

Structural and mechanistic basis of the EMC-dependent biogenesis of distinct transmembrane clients

Lakshmi E Miller-Vedam^{1,2,3,4†}, Bastian Bräuning^{5†}, Katerina D Popova^{3,4,6†}, Nicole T Schirle Oakdale^{4†}, Jessica L Bonnar^{3,4,5}, Jesuraj R Prabu⁵, Elizabeth A Boydston^{4§}, Natalia Sevillano^{7#}, Matthew J Shurtleff^{4¶}, Robert M Stroud², Charles S Craik⁷, Brenda A Schulman^{5*}, Adam Frost^{2*}, Jonathan S Weissman^{3,4,8*}

¹Molecular, Cellular, and Computational Biophysics Graduate Program, University of California, San Francisco, San Francisco, United States; ²Department of Biochemistry and Biophysics, University of California, San Francisco, San Francisco, United States; ³Department of Biology, Whitehead Institute, MIT, Cambridge, United States; ⁴Department of Cellular and Molecular Pharmacology, University of California, San Francisco, San Francisco, United States; ⁵Department of Molecular Machines and Signaling, Max Planck Institute of Biochemistry, Martinsried, Germany; ⁶Biomedical Sciences Graduate Program, University of California, San Francisco, San Francisco, United States; ⁷Department of Pharmaceutical Chemistry, University of California, San Francisco, San Francisco, United States; ⁸Howard Hughes Medical Institute, Chevy Chase, United States

***For correspondence:**

schulman@biochem.mpg.de (BAS);
adam.frost@ucsf.edu (AF);
weissman@wi.mit.edu (JSW)

†These authors contributed equally to this work

Present address: †Gilead Sciences, Foster City, United States; §Whitehead Institute, MIT, Cambridge, United States; #FairJourney Biologics, Porto, Portugal; ¶Lycia Therapeutics, South San Francisco, San Francisco, United States

Competing interests: The authors declare that no competing interests exist.

Funding: See page 39

Received: 30 August 2020

Accepted: 17 November 2020

Published: 25 November 2020

Reviewing editor: Volker Dötsch, Goethe University, Germany

© Copyright Miller-Vedam et al. This article is distributed under the terms of the [Creative Commons Attribution License](#), which permits unrestricted use and redistribution provided that the original author and source are credited.

Abstract Membrane protein biogenesis in the endoplasmic reticulum (ER) is complex and failure-prone. The ER membrane protein complex (EMC), comprising eight conserved subunits, has emerged as a central player in this process. Yet, we have limited understanding of how EMC enables insertion and integrity of diverse clients, from tail-anchored to polytopic transmembrane proteins. Here, yeast and human EMC cryo-EM structures reveal conserved intricate assemblies and human-specific features associated with pathologies. Structure-based functional studies distinguish between two separable EMC activities, as an insertase regulating tail-anchored protein levels and a broader role in polytopic membrane protein biogenesis. These depend on mechanistically coupled yet spatially distinct regions including two lipid-accessible membrane cavities which confer client-specific regulation, and a non-insertase EMC function mediated by the EMC luminal domain. Our studies illuminate the structural and mechanistic basis of EMC's multifunctionality and point to its role in differentially regulating the biogenesis of distinct client protein classes.

Introduction

Integral membrane proteins serve diverse and critical cellular roles, including signal transduction, lipid biosynthesis, adhesion, and transport of molecules across the bilayer. In eukaryotic cells, the endoplasmic reticulum (ER) serves as the primary site of integral membrane protein synthesis, targeting (co- or post-translationally), insertion, folding, and quality control (*Elgaard et al., 2016; Costa et al., 2018*). However, the features of membrane-spanning regions (e.g. low hydrophobicity, charged residues, non-optimal lengths, lipid- and ion-binding sites and hairpins or kinked transmembrane helices) that mediate important functions pose particular challenges for transmembrane

eLife digest Cells are surrounded and contained by a plasma membrane consisting of a double layer of fats and proteins. These proteins monitor and facilitate the movement of food, oxygen and messages in and out of the cell, and help neighboring cells communicate. Membrane proteins are manufactured in a cell compartment called the endoplasmic reticulum. Cellular machines called ribosomes visit this compartment's membrane to manufacture proteins that need to be secreted or embedded into the cell's membranes. As these proteins are made, they are pulled into the endoplasmic reticulum so they can be folded correctly and inserted in the membrane. A cellular machine in this compartment's membrane that aids this process is the endoplasmic reticulum membrane protein complex (EMC). Many steps can go wrong during protein assembly, so to control protein quality, the EMC has to accommodate the variety of complex physical features that proteins can have.

To explore the activity of the EMC, Miller-Vedam, Bräuning, Popova et al. studied the normal structure of the EMC in both yeast and human cells grown in the lab. These snapshots of the complex in different species had a lot in common, including how the complex was arranged within and around the membrane.

Next, Miller-Vedam, Bräuning, Popova et al. generated 50 mutant versions of the EMC in human cells to determine how changing different parts of the complex affected the production of three proteins that rely on the EMC to fold correctly. These proteins were an enzyme called squalene synthase, a signaling protein called the beta adrenergic receptor and sigma intracellular receptor 2, a protein involved in the regulation of cholesterol levels.

Mutations in the section of the EMC outside of the endoplasmic reticulum, within the main cellular compartment, negatively impacted the stability of squalene synthase. This section of the EMC provides a platform where proteins can associate before entering the membrane.

The part of EMC that spans the membrane contains both a fat-filled cavity and a cavity with a 'door' that is either open or closed. Mutations in this section disrupted the insertion of both squalene synthase and the beta adrenergic receptor into the membrane, a role performed by the cavity with the door. The specific role of the fat-filled cavity is still not fully understood, but a mutation affecting this cavity disrupts the correct production of all three proteins studied.

The largest section of the complex, which sits inside the endoplasmic reticulum, protected proteins as they folded, ensuring they were not destroyed for being folded incorrectly before they were fully formed. Mutations in this part of the EMC negatively impacted the stability of sigma intracellular receptor 2 without negatively affecting the other proteins.

This molecular dissection of the activity of the EMC provides insights into how membrane proteins are manufactured, stabilized, coordinated, and monitored for quality. These findings could contribute towards the development of new treatments for certain congenital diseases. For example, cystic fibrosis, retinitis pigmentosa, and Charcot-Marie-Tooth disease are all thought to be caused by mutations within membrane proteins that require the EMC during their production.

protein biosynthesis and folding. Consequently, membrane protein biogenesis is prone to failure, and this can lead to cellular stress and disease (*Marinko et al., 2019*). Thus, it is important to understand the cellular factors that facilitate proper membrane protein biogenesis for such challenging clients.

The ER membrane protein complex (EMC) has emerged as a conserved player in the process of membrane protein biogenesis. It was first identified in *Saccharomyces cerevisiae* as an abundant and stable multi-protein membrane complex whose disruption results in stress mirroring that caused by misfolded membrane proteins (*Jonikas et al., 2009*). Loss of the EMC in mammalian cells is associated with failed biogenesis and degradation of a subset of membrane proteins (*Christianson et al., 2012*). Accordingly, the EMC has been implicated in several mechanistically distinct steps of membrane protein biogenesis, stabilization, and quality control (*Bircham et al., 2011; Richard et al., 2013; Satoh et al., 2015; Savidis et al., 2016; Shurtleff et al., 2018; Volkmar et al., 2019; Tian et al., 2019*).

One well-established EMC function is as an insertase for terminal transmembrane helices. EMC's insertase function has been demonstrated for two classes of clients: low hydrophobicity tail-anchored proteins (i.e. those that contain C-terminal membrane anchors) and a subset of polytopic transmembrane proteins in which the first helix is inserted with the N-terminus in the lumen (Guna et al., 2018; Chitwood et al., 2018). However, many studies indicate EMC functions beyond initial insertion of N- or C-terminal helices. The EMC has been implicated in the biogenesis and stability of many membrane protein classes that do not require a terminal transmembrane insertase (Bircham et al., 2011; Louie et al., 2012; Richard et al., 2013; Shurtleff et al., 2018; Coelho et al., 2019; Luo et al., 2002; Volkmar et al., 2019; Talbot et al., 2019; Petkovic et al., 2020). Recent studies have shown that the EMC is required for stability of internal transmembrane helices of human and viral multi-pass membrane proteins (Hiramatsu et al., 2019; Lin et al., 2019; Ngo et al., 2019; Coelho et al., 2019; Xiong et al., 2020). Additionally, the human EMC (hEMC) physically interacts with the NS4A-B region of the Dengue Virus polyprotein following Sec61-dependent translocation and signal peptidase cleavage, suggesting roles in post-translational stabilization of polytopic membrane proteins (Ngo et al., 2019; Lin et al., 2019). Similarly, the *S. cerevisiae* EMC (yEMC) co-immunoprecipitated with full-length polytopic transmembrane clients, including Pma1p (Luo et al., 2002), Mrh1p, and Fks1p (Shurtleff et al., 2018). In addition to varying types of transmembrane protein clients, the EMC also associates with a range of regulatory factors, including many general and substrate-specific chaperones in the cytoplasm and in the ER lumen (Bagchi et al., 2016; Coelho et al., 2019; Kudze et al., 2018; Richard et al., 2013; Shurtleff et al., 2018).

The complex architecture of the EMC provides additional support for multifunctionality in membrane protein biogenesis. The EMC is an eight (yeast) or nine (mammalian) component, 248–284 kDa complex with considerable mass in the ER lumen, membrane, and cytosol. The cytoplasmic domain contains conserved tetratricopeptide repeats (TPR) repeats in EMC2, and the human complex accommodates an additional subunit, EMC8/9, whose function is not yet understood. The ER luminal domain in yeast does not contain an N-terminal EMC1 expansion seen in hEMC. Notably, the ER luminal domain has been linked to a number of disease-associated phenotypes (Junes-Gill et al., 2011; Probert et al., 2015; Harel et al., 2016; Abu-Safieh et al., 2013; Diamantopoulou et al., 2017; Marquez et al., 2020), and presents the possibility of additional functions for the human luminal domain. One EMC subunit (EMC3) shares limited sequence homology with a family of insertases that are evolutionarily related to the bacterial insertase YidC (Samuelson et al., 2000; Kumazaki et al., 2014; Borowska et al., 2015; Anghel et al., 2017), perhaps explaining the insertase function of the complex. During the preparation of our manuscript, studies describing the structures of the yeast Get1/Get2/Get3 structures, human WRB/CAML/TRC40 (McDowell et al., 2020), translocon bound to Nicalin-TMEM147-NOMO (McGilvray et al., 2020), human structures of the EMC (O'Donnell et al., 2020; Pleiner et al., 2020), and the yeast structure of the EMC (Bai et al., 2020) were published. Those studies focused on the insertase activities of these proteins from the individual species; however, the elaboration of the EMC compared to other known membrane protein biogenesis factors and a diverse client range points to additional functionality that has so far eluded mechanistic explanation. Notably, a systematic structure-based functional analysis across species, conformations, the three distinct EMC domains, and including non-insertase client proteins and mutagenesis of the extensive luminal domain had not been done.

Here, we determined high-resolution cryo-EM structures of yeast EMC bound to a Fab and two conformations of the human EMC structure. Furthermore, we characterized the phenotypes of three distinct classes of EMC clients associated with a series of structure-based EMC mutants. Both yEMC and hEMC structures reveal a path for transmembrane helix insertion from the cytoplasm into the membrane via a conserved cavity. Our structures and mutants also revealed a second lipid-filled cavity with regions of importance for all three client types probed. Analysis of human disease mutations in hEMC1 and our structure-informed mutations enabled us to decouple the EMC insertase function from non-insertase functions and reveal a potential role of the EMC in differentially controlling the biogenesis of distinct classes of client proteins. These structure-function studies collectively establish that the EMC adopts a modular architecture enabling its diverse functions in membrane protein biogenesis.

Results

Overview of strategy to comprehensively reveal EMC structure and function

To comprehensively dissect both conserved and species-specific functions of the EMC, we developed approaches to produce EMC for structure determination and broad mutational analysis (Figure 1A–D). We developed systems to produce robust quantities of pure intact yEMC and hEMC to determine structures for the two organisms in which different facets of EMC function have been described in detail (Jonikas et al., 2009; Christianson et al., 2012; Guna et al., 2018; Shurtleff et al., 2018). Parallel efforts converged on an approach involving FLAG affinity-tagging of the EMC5 C-terminus, which was performed for endogenous yEMC and recombinant hEMC in human embryonic kidney (HEK) cells (Figure 1—figure supplements 1–2, Supplementary file 1).

In parallel, to enable testing of hypotheses based on structures, we created a suite of human (K562) knockout cell lines deleted for individual hEMC subunits - hEMC1 (lumen), hEMC2 (cytoplasm), hEMC3, and hEMC5 (transmembrane) - and a series of reporters of EMC-dependent transmembrane protein biogenesis (Figure 1—figure supplements 3–4). Reintroduction of the wild-type hEMC subunits in the respective knockout cells fully rescued the knockout phenotype (Figure 1—figure supplements 5–6). This allowed for introduction of structure-based mutations in hEMC subunits into the respective knockout cells to determine features supporting biogenesis of fluorescently tagged versions of three different types of EMC clients: the transmembrane domain of a C-terminal tail-anchored transmembrane protein (squalene synthase, SQS³⁷⁸⁻⁴¹⁰) (Guna et al., 2018), a polytopic transmembrane protein that depends on the EMC N-terminal insertase activity (Beta 1 adrenergic receptor, B1AR) (Chitwood et al., 2018), and a polytopic transmembrane protein (Sigma intracellular receptor 2, TMEM97) whose biogenesis requires the Sec61 translocon but does not require a terminal helix insertase (Figure 1—figure supplements 3–6). Three individual EMC clients were fused to mCherry fluorescent protein and GFP separated by a P2A ribosomal skipping sequence. Translation of the described mRNA generates two products due to peptide bond skipping at the P2A sequence. For each molecule of the client-mCherry fusion, there is one GFP molecule. Reduction in mCherry levels relative to GFP reflects post-translational degradation of the client fused to mCherry. Each of the client reporters were introduced into five separate cell lines: wild-type K562 cells, hEMC1 knockout K562 cells, hEMC2 knockout K562 cells, hEMC3 knockout K562 cells, and hEMC5 knockout K562 cells. Monitoring the effect of an hEMC mutation on fluorescent reporter levels provided a quantitative measure of its impact on EMC-dependent biogenesis of each class of client protein. A number of mutations of varying severity, varying conservation between yeast and human (Figure 1—figure supplements 7–8), were designed and tested spanning the hEMC structure. Subsequently, these 49 mutations were mapped onto the structure grouped by reporter phenotype (Video 1, Supplement File 2). To allow for direct comparison of our structure-guided mutant phenotypes with those published recently by others (Pleiner et al., 2020; Bai et al., 2020; O'Donnell et al., 2020), we summarized all mutant data (Supplementary file 3). A subset of the mutant cell lines was validated by genotyping (Figure 1—figure supplement 9). Western blots against the endogenous hEMC subunits allowed us to control for mutational effects on the production and stability of the hEMC complex itself. We concurrently blotted for three clients, SQS, TMEM97, and BCAP31, to assay changes in endogenous protein levels for each of the mutations (Figure 1—figure supplements 5–6, Supplementary file 4). This strategy thus distinguishes effects resulting from a global disruption of the EMC complex from those caused by specific disruption of EMC function. These functional assays of the hEMC show a broad dependence of all these clients on the EMC, consistent with previous work (Shurtleff et al., 2018; Guna et al., 2018; Chitwood et al., 2018; Volkmar et al., 2019; Tian et al., 2019). In order to understand the mechanism of action, we will now go in more detail through several of the mutants with the strongest functional phenotypes in differing regions of the three-dimensional structure.

The EMC is an intricate molecular machine spanning the ER membrane and exhibits a conserved core architecture

We determined structures of yEMC and hEMC — all showing overall compositional similarity, with regional conformational differences between the yeast and human complexes (Figure 2A–D). We

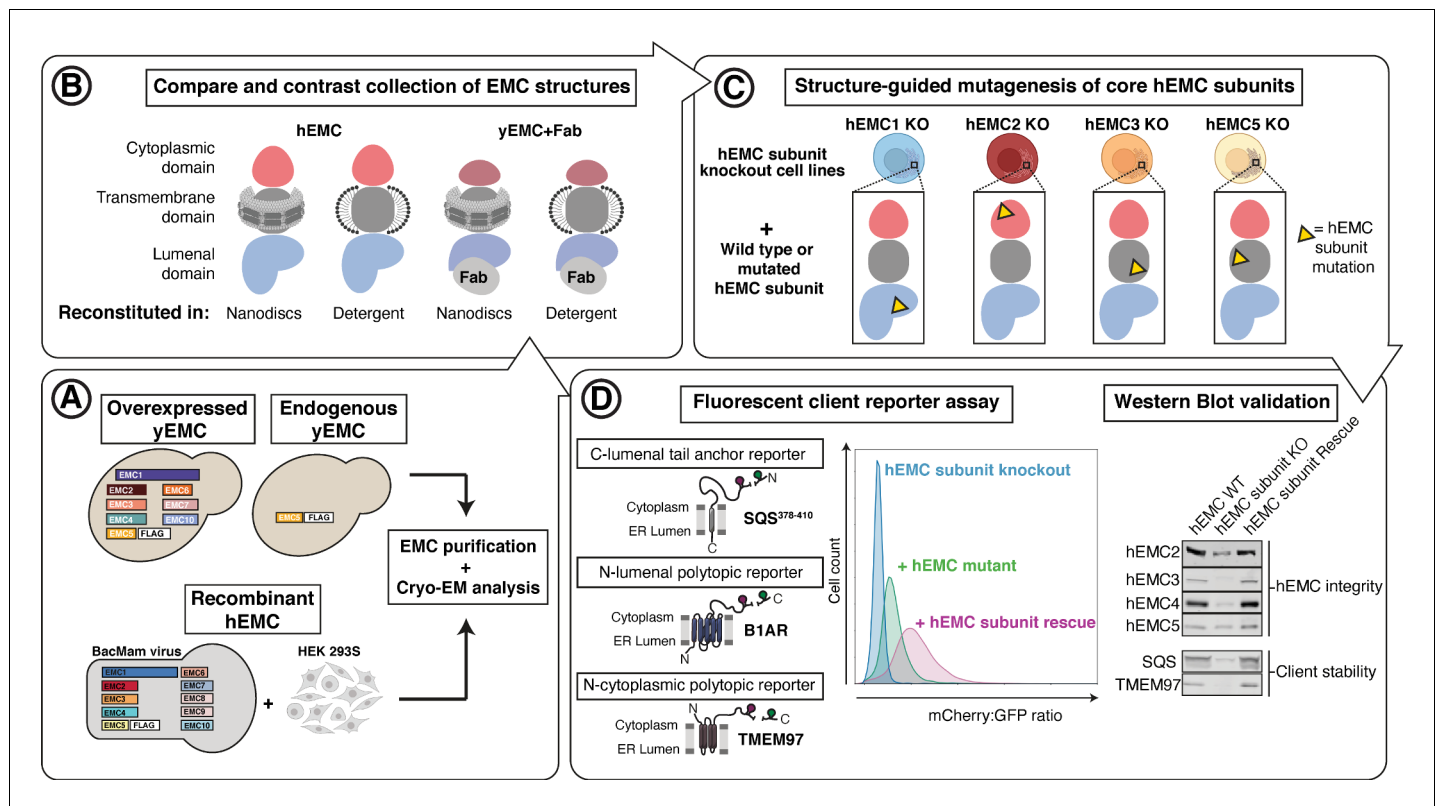


Figure 1. Experimental strategy for the dissection of EMC function. Schematic representation of the combined structural and mutational approach to dissect EMC function. (A) yEMC was purified either by overexpression of all subunits together and affinity pulldown with 3xFlag-tagged yEMC5 or by pulldown of endogenous yEMC proteins using an affinity pulldown with 3xFlag-tagged yEMC5. For hEMC, all subunits were overexpressed together with Flag-tagged EMC5 via a single recombinant BacMam virus. Both yEMC and hEMC were purified by column chromatography and subjected to cryo-EM analysis. (B) The obtained collection of cryo-EM structures of yEMC and hEMC in lipid nanodiscs or detergent micelles were compared to identify similarities and differences. (C) Structure-guided mutagenesis was performed across four core hEMC subunits: hEMC1, hEMC2, hEMC3, and hEMC5 in mammalian K562 cells. (D) Each hEMC subunit knockout (KO) cell line was individually transduced with three different fluorescent client reporters: SQS³⁷⁸⁻⁴¹⁰, full-length B1AR, and full-length TMEM97. Mutant hEMC subunits were then introduced into the corresponding subunit KO cell lines carrying each of the three fluorescent hEMC client reporters. hEMC client stability in each mutant hEMC subunit cell line was assessed by quantifying the mCherry-to-GFP ratio. Western blotting was performed for each mutant-transduced cell line to assess EMC integrity (by immunoblotting for hEMC subunits) as well as client stability (by immunoblotting for hEMC clients) compared against both wild-type (WT) and KO cell lines.

The online version of this article includes the following figure supplement(s) for figure 1:

Figure supplement 1. Purification of yEMC.

Figure supplement 2. Purification of recombinant hEMC.

Figure supplement 3. Fluorescent reporter cell line generation.

Figure supplement 4. Overview of functional assays.

Figure supplement 5. Western blots for EMC1 and EMC2.

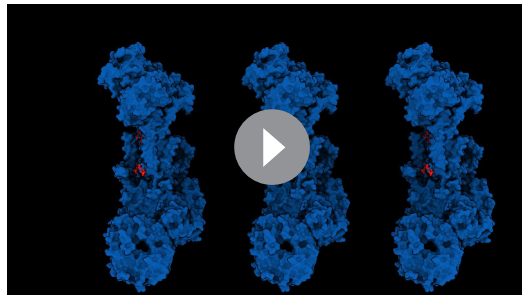
Figure supplement 6. Western blots for EMC3 and EMC5.

Figure supplement 7. Amino acid conservation of EMC1.

Figure supplement 8. Amino acid conservation of EMC2, EMC3, EMC5.

Figure supplement 9. Genotyping of 10 mutants.

obtained reconstructions of yEMC bound to an antigen binding fragment (Fab) and hEMC reconstituted both in detergent micelles and lipid nanodiscs, with the latter strategy yielding the most isotropic and highest resolution data. For yEMC+FabDH4 and hEMC, the global map resolutions reached 3.2 Å and 3.4 Å, respectively (Table 1, Figure 2—figure supplements 1–4). The cryo-EM maps allowed for de novo model building of both human and yeast complexes (Figure 2—figure supplements 5 and 6). As described in the following sections, our multiple EMC structures enable a broad survey of its conserved architecture, with variations between the structures pointing to



Video 1. hEMC mutagenesis displayed on hEMC structures. Three identical copies of hEMC in nanodisc (colored blue) are displayed here. Subsequent labeling and coloring of mutated residues by flow cytometric measure of reporter abundance, grouped into three categories: increased reporter levels (mCherry > GFP signal, colored white), wild-type levels (mCherry signal is close to GFP signal, colored light blue), and decreased reporter levels (mCherry < GFP signal, colored gold). Left hEMC structure displays phenotypes for the C-luminal tail anchor reporter (GFP-P2A-mCherry-SQS³⁷⁸⁻⁴¹⁰-opsin). Middle hEMC structure displays phenotypes for the N-luminal polytopic reporter (B1AR-mCherry-P2A-GFP). Right hEMC structure displays phenotypes for the N-cytoplasmic polytopic reporter (TMEM97-mCherry-P2A-GFP). Mutations with little to no phenotype are displayed as similar to wild-type levels.

<https://elifesciences.org/articles/62611#video1>

McDowell et al., 2020; McGilvray et al., 2020), the arrangement of domains of the EMC is unusual with the transmembrane domain connecting prominent cytoplasmic and luminal domains (**Figure 2E**). On a global level, the structure suggests complexities beyond those of some other ER machineries fulfilling select functions in transmembrane protein biogenesis.

The cytoplasmic domain provides a platform for protein-protein interactions

The exterior interface of the cytoplasmic domain is formed by EMC2, EMC3, EMC4, and parts of hEMC8/9 (in human), while parts of EMC5, EMC2, and EMC8/9 are shielded from the cytoplasm (**Figure 3A–B**). The helical fold of EMC2 constitutes the central organizer of this platform, established by five or six TPR motifs in human versus yeast, respectively (**Figure 3C**). TPR domains are commonly found mediating protein-protein interactions and are present in numerous well-characterized chaperone-protein and other interaction networks (*Blatch and Lässle, 1999; Scheufler et al., 2000; Schlegel et al., 2007; Assimon et al., 2015; Krysztofinska et al., 2017; Graham et al., 2019*). Yeast EMC2 features a more curved helical arrangement with N- and C-terminal domains in closer proximity to each other than seen in hEMC2. Notably, the canonical peptide-binding TPR groove is occupied by the partially helical C-terminus of EMC5, which forms a large interaction surface with EMC2. To test the functional roles of this interaction, we mutated three residues within the hEMC2 TPR motif (hEMC2^{K125E + R126D + K127E}) or a single hEMC5 residue buried in the TPR-binding groove (hEMC5^{F90A}). The mutations on both sides of the interface decreased hEMC integrity by western blot, with a modest decrease of hEMC subunits for hEMC5^{F90A} and a strong reduction in the levels of several hEMC subunits for hEMC2^{K125E + R126D + K127E} (**Figure 3C, Figure 3—figure supplements 1–2, Figure 1—figure supplements 5–6**). This suggests that this interface might be critical for EMC complex assembly rather than EMC function.

conformational and compositional differences (**Figure 2—figure supplements 7–8**). We note that our maps and models are consistent with recent cryo-EM data from yeast EMC (*Bai et al., 2020*), human EMC (*O'Donnell et al., 2020; Pleiner et al., 2020*), and a crystal structure of human EMC2-EMC9 (*O'Donnell et al., 2020; Figure 2—figure supplement 9*).

The EMC is comprised of cytoplasmic, transmembrane, and luminal domains arranged similarly for yeast and human, despite significant evolutionary separation (**Figure 2A–B**). For both species, subunits encompassing EMC2 to EMC7 form an interconnected core complex, while there is additional density capping both the cytoplasmic and luminal domains of hEMC, occupied by an hEMC8/9 and an hEMC1 N-terminal expansion, respectively (**Figure 2C–D**). hEMC8 and hEMC9 are paralogs of each other, which have not been identified in yeast (*Wideman, 2015*). We modeled and depict only hEMC8 for clarity, but due to the 44% sequence identity with hEMC9 and both being present in the recombinant system we refer to this as hEMC8/9. The large hEMC1 insertion in hEMC constitutes the majority of a membrane distal beta-propeller domain protruding into the lumen, a feature missing from *S. cerevisiae*. Compared to other ER-resident proteins implicated in membrane protein biogenesis (*Suloway et al., 2009; Pfeffer et al., 2017; Ramirez et al., 2019;*

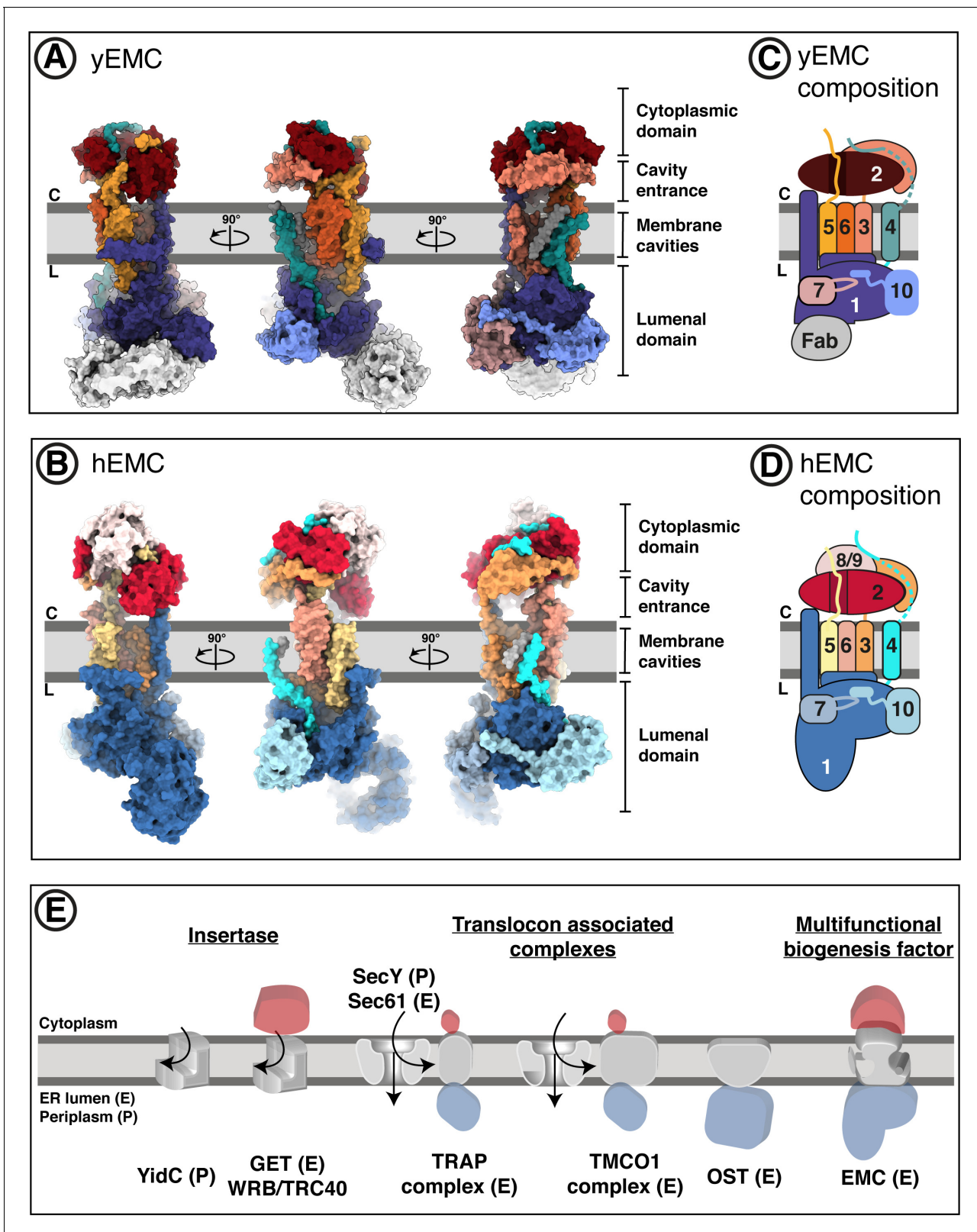


Figure 2. Overall structures of yeast and human EMC. (A) Cryo-EM structure of yEMC in nanodiscs. Three orthogonal views of the yEMC cryo-EM structure shown as surface rendering. Gray bars delineate the approximate ER membrane boundaries with the cytoplasmic (C) and luminal (L) sides indicated. The FAB molecule bound to the yEMC1 luminal domain is colored in gray. (B) Cryo-EM structure of hEMC in nanodiscs. Labeling as in (A). (C) Subunit composition and color scheme of yEMC used throughout the manuscript. Dotted line indicates a portion of yEMC4 unresolved in the cryo-EM structure. *Figure 2 continued on next page*

Figure 2 continued

EM map and left unmodeled. (D) Subunit composition and color scheme of hEMC used throughout the manuscript. (E) Schematic depiction and comparison of the EMC architecture to known transmembrane protein biogenesis factors in the ER and the bacterial plasma membrane. Cytoplasmic, transmembrane and luminal domains are depicted as cartoons colored red, gray and blue, respectively. E, eukaryotic; P, prokaryotic. The online version of this article includes the following figure supplement(s) for figure 2:

- Figure supplement 1.** Cryo-EM reconstruction of yEMC.
- Figure supplement 2.** Cryo-EM reconstruction of hEMC.
- Figure supplement 3.** Cryo-EM data processing workflow for yEMC.
- Figure supplement 4.** Cryo-EM data processing workflow for hEMC.
- Figure supplement 5.** yEMC cryo-EM map validation.
- Figure supplement 6.** hEMC cryo-EM map validation.
- Figure supplement 7.** Subunit-subunit correspondence between yEMC and hEMC.
- Figure supplement 8.** Comparison between individual yEMC and hEMC subunits.
- Figure supplement 9.** Pairwise superposition of EMC structures in the PDB.

The multi-protein cytoplasmic cap has distinct elements between hEMC and yEMC. Capping the cytoplasmic domain in hEMC is hEMC8/9; the functional roles of this cap-like structure are not yet clear. An hEMC8-9 heterodimer is not observed and our cryo-EM permits tracing with both the hEMC8 or hEMC9 amino acid sequence (**Figure 3—figure supplement 3**). Mass spectrometric analysis of our hEMC preparations reveals slightly higher abundance of hEMC8 to hEMC9 (**Figure 1—figure supplement 2E–F, Supplementary file 1**), so we modeled the cytoplasmic cap structure with the hEMC8 sequence. A groove on hEMC8/9 cradles an N-terminal peptide of hEMC4, which proceeds into the EMC4 segment that traverses over hEMC2 and the three-helix bundle of hEMC3 (**Figure 3D**). Although yEMC lacks EMC8/9, yEMC4 follows a similar binding trajectory along cytoplasmic yEMC2 and yEMC3 surfaces. A stretch of 20 hEMC4 amino acids (residues 23–42) after the hEMC8/9 binding site is only poorly resolved in our cryo-EM maps and predicted to be disordered (40% glycine content). This loop contains primarily polar amino acids, and traverses the top of the hEMC2 TPR domain. To see whether this dynamic hEMC2-hEMC4 interface played a role in client stabilization, we mutated two charged patches on hEMC2 to alanines (hEMC2^{E146A+E149A+Q150A}, hEMC2^{E168A+D170A+K173A}), lying in close vicinity to hEMC4²³⁻⁴² (**Figure 3E–F**). These mutants lead to a modest accumulation of the tail-anchored client (SQS³⁷⁸⁻⁴¹⁰) but did not affect polytopic client abundance or decrease of hEMC subunits (**Figure 3E–F; Figure 1—figure supplement 5**). Several mutants across the cytoplasmic domain showed similar phenotypes, supporting a key role in tail anchor protein biogenesis (**Figure 3—figure supplements 1–2**).

Two distinct cavities are present in the transmembrane domain

The transmembrane core of EMC is predicted to include contributions from each subunit except for EMC2 and, in humans, hEMC8/9 (**Figure 2C–D**). The EMC presents two distinct and structurally conserved cavities on opposite sides of the transmembrane core that differ in size, shape, subunit compositions and apparent function (**Figure 4A–B**). One cavity, which we refer to as the lipid-filled cavity, appears contiguous with the ER lipid environment (**Figure 4A**). The second cavity, which we refer to as the gated cavity, appears to open toward the cytoplasm in our structures and is more occluded by a transmembrane helix gate from the lipid environment (**Figure 4B**). Notable structural hallmarks present in both species include a superimposable core of nine transmembrane helices, a set of flexible gate helices, and an amphipathic EMC1 brace helix (**Figure 4C**).

The gated cavity serves as a conduit for terminal helix insertion

Evaluating potential client paths from the cytoplasm into the transmembrane domain revealed a cavernous opening at the membrane-cytoplasmic interface of the gated cavity, wide enough to allow passage of a client helix, and tapering toward the lumen (**Figure 4D**). Consistent with its potential role as a cytoplasmic conduit into the EMC, the EMC3 portion of the cytoplasmic domain, which delineates this opening, sits approximately 45 Å from the luminal side of the gated cavity. This dimension exceeds the thickness of the ER membrane (**Mitra et al., 2004; Heberle et al., 2020; Cornell et al., 2020; Figure 4D**). This cavity is lined primarily by EMC3, EMC4, and EMC6 (**Figure 5A**). Simulating the dimension of the first transmembrane helix of a known terminal

Table 1. Cryo-EM data acquisition, reconstruction, and model refinement statistics.

	yEMC in detergent dataset 1	yEMC in detergent dataset 2	yEMC in nanodiscs	hEMC in detergent	hEMC in nanodiscs
EMDB accession code	EMD-23033		EMD-23003	EMD-11733	EMD-11732
PDB accession code	PDB-7KTX		PDB-7KRA	PDB-7ADP	PDB-7ADO
Data collection and processing					
Microscope	FEI Technai Polara	FEI Titan Krios	FEI Titan Krios	FEI Titan Krios	FEI Titan Krios
Camera	Gatan K2 Summit	Gatan K2 Summit	Gatan K3	Gatan K3	Gatan K3
Magnification	31,000x	22,500x	105,000x	81,000x	105,000x
Voltage (kV)	300	300	300	300	300
Electron exposure (e ⁻ /Å ²)	56.8	58.3	67	62	72
Defocus range (μm)	-1.0 to -3.0	-1.0 to -3.0	-0.8 to -2.5	0.7-2.8	0.7-2.8
Pixel size (Å)	1.22	1.31	0.853	1.094	0.8512
Software	Relion 2.0, Relion 3.0, THUNDER	Relion 2.0, Relion 3.0, THUNDER	Relion 3.0, cryoSPARC v2	Relion 3.0, cryoSPARC v2	Relion 3.0, cryoSPARC v2
Symmetry imposed	C1	C1	C1	C1	C1
Initial particle images (no.)	419,907	670,078	6,100,000	3,350,000	5,900,000
Final particle images (no.)	83,599	170,186	230,528	144,222	177,560
Overall map resolution (Å)	8	7			
FSC threshold 0.143	4.3 (combined)		3.2	3.60	3.39
Local map resolution range (Å)	3.6-6.4		2.6-6.4	2.8-6.0	3.0-7.2
Refinement					
Software	Phenix 1.18 real-space-refine		Phenix 1.18 real-space-refine	Phenix 1.18 real-space-refine	Phenix 1.18 real-space-refine
Model resolution (Å)					
FSC threshold 0.5	4.5		3.5	3.9	3.6
Map sharpening B factor (Å ²)	-125		-75	-115	-126
Model composition					
Non-hydrogen atoms	17,315		17,293	15,040	16,652
Protein residues	2171		2164	1880	2086
Ligands	NAG: 6		NAG: 5; PCW: 1	NAG: 2	NAG: 4; PCW: 5
B factors (Å²)					
Protein (mean)	167		107	111	126
Ligand (mean)	146		92	107	127
R.m.s. deviations					
Bond lengths (Å)	0.006		0.005	0.005	0.005
Bond angles (°)	0.988		0.804	0.718	0.782
Validation					
MolProbity score	1.44		1.29	1.46	1.28
Clashscore	8.1		3.5	9	6
Ramachandran plot					
Favored (%)	98		97	97	97

Table 1 continued on next page

Table 1 continued

	yEMC in detergent dataset 1	yEMC in detergent dataset 2	yEMC in nanodiscs	hEMC in detergent	hEMC in nanodiscs
Allowed (%)	2		3	3	3
Disallowed (%)	0		0	0	0

insertase-client (B1AR - *Chitwood et al., 2018*) suggests that there is sufficient space for a client helix even in the client-free state of the EMC (*Figure 5B*). The gated cavity is hydrophilic on the cytoplasmic side and becomes increasingly hydrophobic toward the luminal side (*Figure 5C*).

The entrance into the gated cavity interior (*Figure 5A*) is formed primarily by the EMC3 cytoplasmic domain. To test its function, charge swap mutations were introduced along the rim of this opening (hEMC3^{E63K + D213K + E223K}, hEMC3^{R59E + R62E + K216E}) (*Figure 5D*). These mutants resulted in loss of the tail-anchored client (SQS³⁷⁸⁻⁴¹⁰) and partial loss of the N-terminal insertase-dependent polytopic client (B1AR), reflecting a failure to support insertase activity. These mutants had no appreciable effect on the abundance of the polytopic transmembrane client (TMEM97) reporter (*Figure 5E, Figure 5—figure supplements 1–2*). A similar phenotype was observed with alanine substitutions for a pair of lysines at the periphery of this cytoplasmic rim (hEMC3^{K42A + K43A}) (*Figure 5—figure supplement 2*).

Having identified a functionally important entry route for terminal helix insertase clients, we next considered potential surfaces inside the cavity that might accommodate a client helix. A polar patch close to the membrane interior of this cavity was conspicuous, even though the specific amino acid residues are not strictly conserved (*Figure 1—figure supplement 8*). Mutating a pair of adjacent asparagine residues to equivalently sized but negatively charged aspartates (hEMC3^{N114D+N117D}) resulted in a dramatic decrease in SQS³⁷⁸⁻⁴¹⁰ reporter levels and no significant decrease in the other two client reporter levels (*Figure 5F*). Western blot analysis for this mutant showed wild-type rescue levels of hEMC subunits and a decrease in endogenous SQS levels (*Figure 1—figure supplement 6*). Meanwhile, mutating a neighboring positively charged residue to an alanine (hEMC3^{R180A}), a residue that is conserved in some of the YidC-superfamily insertase proteins (*Anghel et al., 2017*), resulted in partial loss of only the tail-anchored insertase client (SQS³⁷⁸⁻⁴¹⁰) (*Figure 5—figure supplements 1 and 3*).

Lastly, we surveyed residues closer to the hydrophobic luminal side of the gated cavity. Lipid density was resolved at positions along the cavity in hEMC and yEMC cryo-EM maps (*Figure 4B*) and the properties of this hydrophobic seal to the lumen are conserved (*Figure 5—figure supplement 4A–B*). The importance of this hydrophobic seal is suggested by the strong effect of a structurally mild mutation of a conserved methionine to a leucine (hEMC3^{M151L}), which caused significant decrease in both SQS³⁷⁸⁻⁴¹⁰ and B1AR abundance (*Figure 5G*). Mutation of a neighboring aromatic residue (hEMC3^{F148L}), contacting both a lipid and a hEMC4 C-terminal transmembrane helix, caused a decrease in all three client types without altering the levels of hEMC subunits (*Figure 5—figure supplements 1–2, Figure 1—figure supplement 6*). Together these results indicate that proper EMC insertase function depends on the exact composition of the cavity and not simply on its hydrophobic nature.

Structural heterogeneity suggests a role for the gate in regulating access to the insertase transmembrane cavity

While the core transmembrane helices of the gated cavity are superimposable in all four of our EMC structures, the adjacent gate helices appear in different relative orientations. The structural variability likely reflects dynamics of the gate (*Figure 4C*). Comparing detergent and nanodisc maps for both species identified two major gate conformations (*Video 2, Figure 5—figure supplement 5A*). One of the conformations, referred to as the closed-gate conformation, results in a more occluded membrane cavity. The other conformation, referred to as the open-gate conformation, would provide space for client accommodation.

The C-terminal transmembrane helix of EMC4 and ensuing luminal segment are well resolved in all four structures; however, other regions of EMC4, including the segment connecting the

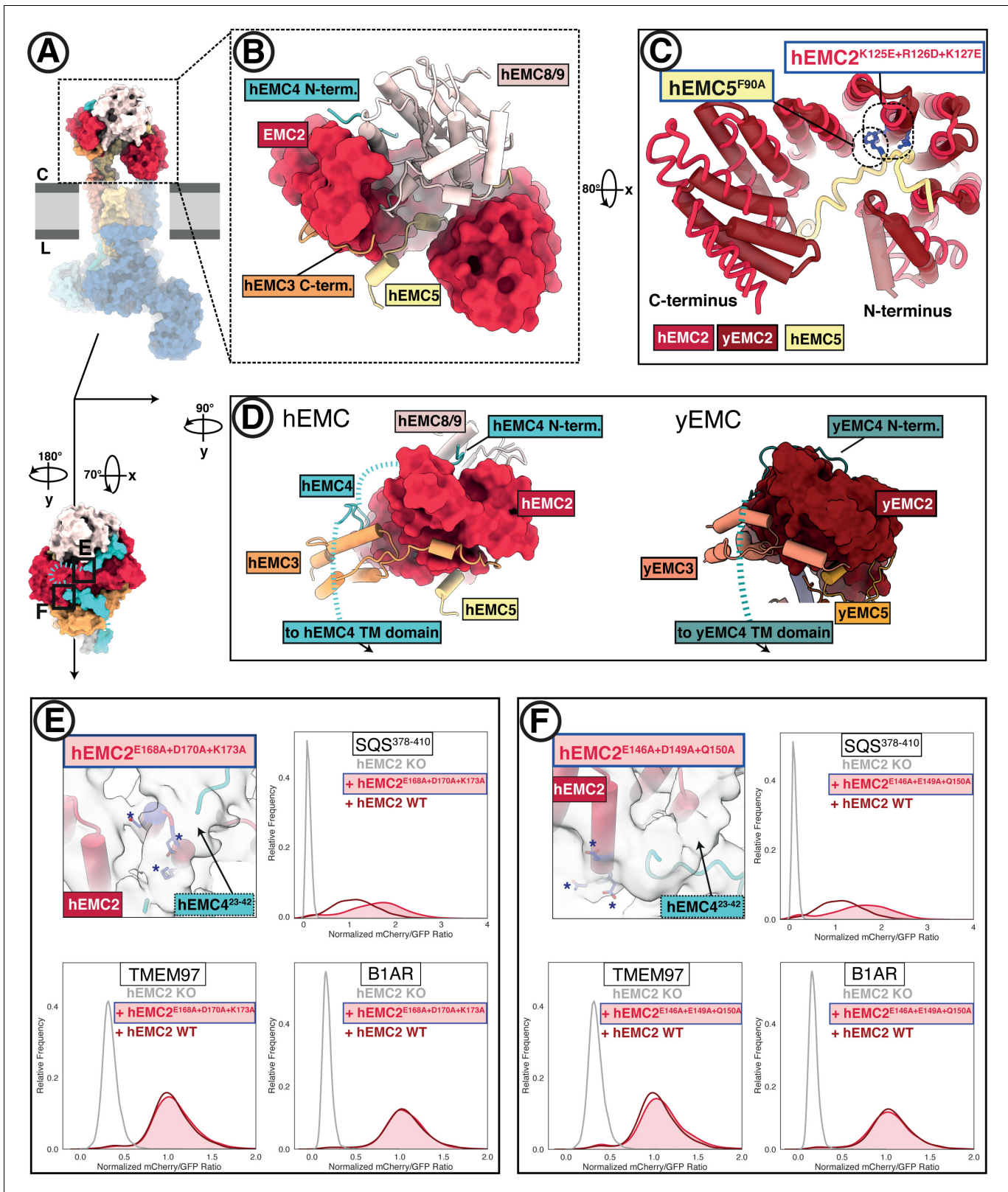


Figure 3. The EMC cytoplasmic domain contains conserved functional interfaces and may engage C-tail-anchored clients directly. (A) Position of the hEMC cytoplasmic domain relative to the membrane and the rest of the complex. Shown is the surface rendered hEMC structure reconstituted in nanodiscs. (B) EMC2 nucleates a protein-protein interaction hub in the cytoplasm. Zoomed-in view of the cytoplasmic domain from (A). EMC2 is shown as surface rendering while interacting EMC subunits are shown as cartoon cylinders. (C) EMC2 forms a TPR domain which binds EMC5. Overlaid are *Figure 3 continued on next page*

Figure 3 continued

hEMC2 (red) and yEMC2 (dark red), illustrating the more tightly wound yEMC2 TPR solenoid. Two mutants, one in EMC5 and three in EMC2, are colored in blue, and show destabilizing phenotypes for EMC integrity. (D) A cytoplasmic cap structure involving EMC4 is conserved in yEMC and hEMC. Shown is a side-by-side comparison between the cytoplasmic domains of hEMC (left) and yEMC (right), highlighting the similar path EMC4 takes from the cytoplasmic domain toward the transmembrane domain. While an interaction surface between EMC8/9 and the EMC4 N-terminus is absent in yeast, yEMC4 binds at the top of the EMC2 TPR domain and assumes a similar position across the EMC3 cytoplasmic domain at the cytoplasm-membrane interface. (E) Fluorescent client reporter stability assay for TMEM97 (N-cytoplasmic polytopic client), B1AR (N-luminal polytopic client) and SQS³⁷⁸⁻⁴¹⁰ (C-luminal tail-anchored client) in EMC2 KO cells expressing mutant hEMC2^{E168A+D170A+K173A} (shaded) or WT hEMC2 rescue (unshaded). Shown is the model of hEMC in nanodiscs superposed with the unsharpened cryo-EM map, where the weaker density for EMC4 (23–42) becomes apparent. Mutated residues are colored blue and marked with asterisks for clarity. (F) Fluorescent client reporter stability assay, as in E, for the hEMC2^{E146A+E149A+Q150A} mutant.

The online version of this article includes the following figure supplement(s) for figure 3:

Figure supplement 1. Flow cytometry for mutations in the EMC cytoplasmic domain.

Figure supplement 2. Additional flow cytometry for mutations in the EMC cytoplasmic domain.

Figure supplement 3. Both EMC8 and EMC9 can be fitted into the hEMC cryo-EM maps.

cytoplasmic domain to the transmembrane gate helices, were poorly resolved, perhaps owing to mobility. The yEMC detergent map, yEMC nanodisc map, and hEMC detergent map all show the unassigned helices in the closed conformation, preventing client residence in the gated cavity. By contrast, the hEMC nanodisc map reveals an open-gate conformation with the unassigned helices shifted away from the transmembrane core to provide space for a client (**Figure 5B**). Consistent with our observations, the closed transmembrane gate conformation can also be seen in recently published cryo-EM maps of hEMC (**O'Donnell et al., 2020**) and yEMC (**Bai et al., 2020**), which studied LMNG and digitonin-solubilized complexes, respectively (**Figure 5—figure supplement 5B**). We note that the conformational heterogeneity and concomitant lower resolution of the gate likely accounts for the challenges in making unambiguous subunit assignments (**Figure 5—figure supplement 5C–E**), reflected by the three different interpretations reported in recent structures (**Pleiner et al., 2020; O'Donnell et al., 2020; Bai et al., 2020**).

Considering the apparent flexibility of the gate, we sought to mutate the hEMC4 interfaces resolved in the cytoplasm versus the membrane. As described above, mutating residues that together form a composite-binding surface for the cytoplasmic domain of hEMC4 (hEMC2^{E146A+E149A+Q150A}, hEMC2^{E168A + D170A + K173A}, **Figure 3E–F**), we observed a modest accumulation of the tail-anchored insertase client (SQS³⁷⁸⁻⁴¹⁰). Likewise, mutating residues in the center of the gated cavity, close to one of the unassigned helices in the closed-gate conformation (hEMC3^{V118A + I122A}) (**Video 2, Figure 5—figure supplement 1**) led to an increase of SQS³⁷⁸⁻⁴¹⁰. This SQS³⁷⁸⁻⁴¹⁰ accumulation effect stands in contrast to mutating a residue that contacts the luminal anchor of hEMC4 (hEMC3^{F148L}), which caused a reduction of SQS³⁷⁸⁻⁴¹⁰ levels (**Figure 5—figure supplement 1**).

The lipid-filled cavity is critical for both insertase-dependent and insertase-independent EMC functions

In addition to the gated cavity, the EMC harbors another membrane-accessible cavity. The surface of the lipid-filled cavity includes contributions from EMC1, EMC3, EMC5, and EMC6 (**Figure 6A**). In our structures, the EMC2 N-terminus occludes cytoplasmic accessibility to this cavity (**Figure 4D, Figure 6A–B**). However, this cavity may be accessible from the membrane or the ER lumen. The respective distance from the cytoplasmic EMC2 N-terminus to the luminal side of the lipid-filled cavity is approximately 35 Å across, which is close to the average ER membrane thickness (**Mitra et al., 2004**).

The lipid-filled cavity features a uniformly hydrophobic surface (**Figure 6C**) and superimposes across our ensemble of EMC structures. As noted, we resolved several lipids in our cryo-EM maps lining the cavity wall and modeled four POPC (1-palmitoyl-2-oleoyl-sn-glycero-3-phosphatidylcholine) molecules in the hEMC nanodisc map (**Figure 6C**). The residues in close proximity to these lipids are moderately conserved (**Figure 5—figure supplement 4C–D**). To characterize the functional role of the lipid-filled cavity, we mutated cavity-lining and lipid-proximal residues (**Figure 6D, Figure 6—figure supplements 1–2**). Most of these mutations resulted in an increased abundance of the tail-anchored reporter (SQS³⁷⁸⁻⁴¹⁰) and wild-type rescue levels for the other two reporters (B1AR,

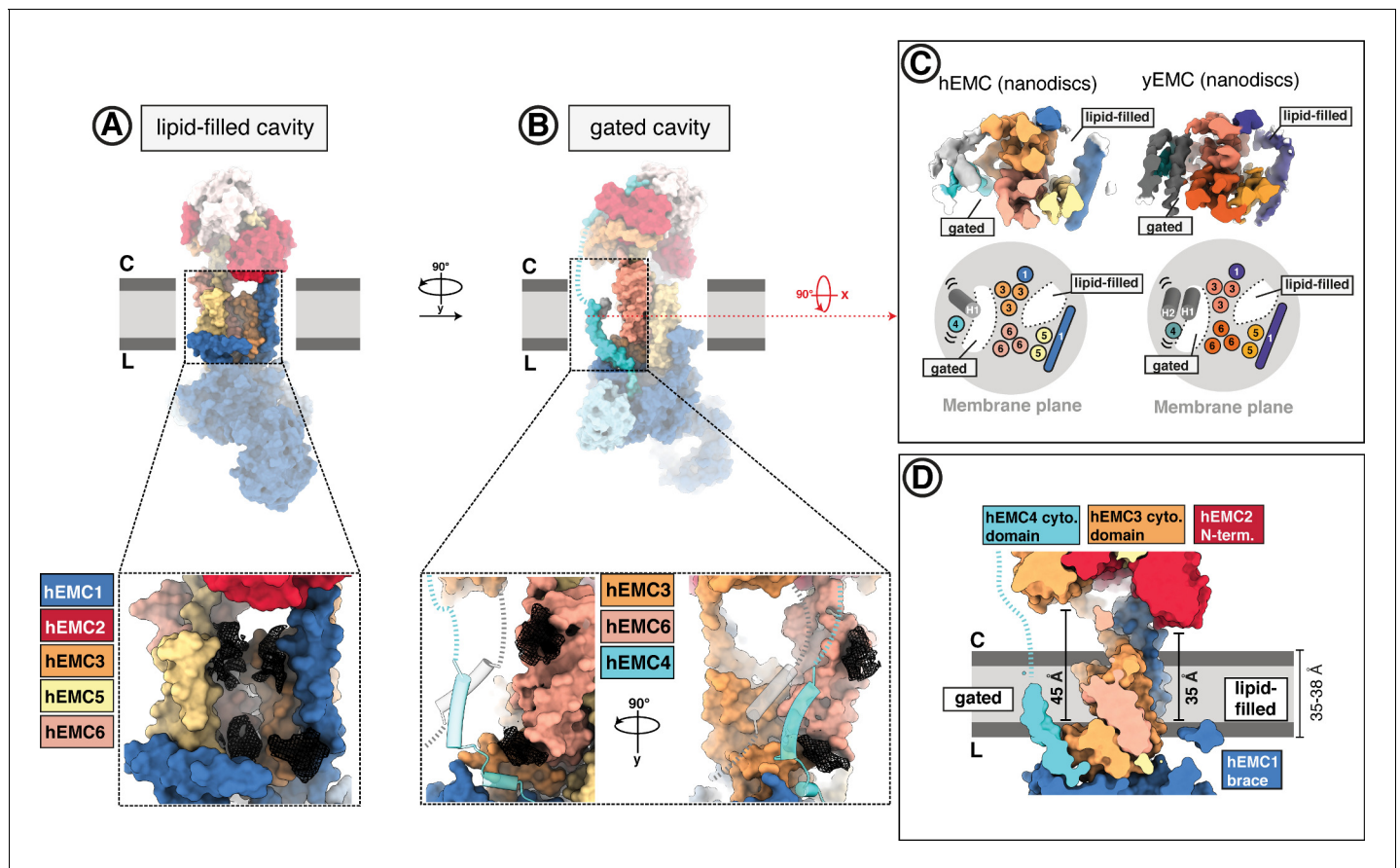


Figure 4. The EMC houses two transmembrane cavities with conserved core structures and distinct accessibilities. (A) Location and composition of the lipid-filled cavity. A zoom-in view on the cavity is shown below, which is composed of EMC1, EMC3, EMC5, and EMC6. Resolved lipid densities from the cryo-EM map of hEMC in POPC nanodiscs are shown as black mesh zoned within 3 Å of modeled POPC molecules. (B) Location and composition of the gated cavity. Two orthogonal zoom-in views of the cavity are shown below, which is composed of EMC3 and EMC6. A transmembrane gate opposite the cavity wall is depicted as transparent cartoon cylinders and has contributions from the C-terminal EMC4 transmembrane helix along with up to two additional, unassigned helices. Resolved lipid densities are shown as in (A). (C) The dual-cavity architecture of the EMC transmembrane domain is conserved between yEMC and hEMC. Unsharpened cryo-EM maps of hEMC and yEMC in nanodiscs (top) are shown along with corresponding schematic representations of the spatial organization of all transmembrane helices (bottom). The gate helices of the gated cavity represent the region of highest conformational heterogeneity across our collection of EMC structures. (D) The two EMC transmembrane cavities feature distinct accessibilities. Shown is a central slice through the surface rendered hEMC nanodisc structure with the two membrane cavities on opposite sides. Measuring from the luminal to the cytoplasmic side, gated and lipid-filled cavities measure 45 Å and 35 Å across, respectively. This suggests that the gated cavity has accessibility from the cytoplasm while the lipid-filled cavity does not.

TMEM97). However, one lipid-proximal mutant showed decreased levels of all three client reporter types with varying severity (hEMC3^{R13E}) without altering overall EMC levels (Figure 6E). Western blotting for the endogenous SQS and TMEM97 revealed a decrease in endogenous SQS and TMEM97 levels for this mutant (Figure 1—figure supplement 6). An analogous mutation in *Drosophila* EMC3 was recently reported to cause reduced levels of Rh1 in this mutant background (Xiong et al., 2020). The amphipathic EMC1 brace helix, which packs against the transmembrane helices of EMC5, is a structural hallmark of the lipid-filled cavity (Figure 6D). Here, mutating interfacial residues from hEMC5 (hEMC5^{H19L+S23A+Q26L}) caused a marked decrease in the N-luminal polytopic reporter (B1AR) and no effect on either the tail-anchored client (SQS³⁷⁸⁻⁴¹⁰) or the polytopic client reporter (TMEM97) (Figure 6F). Unexpectedly, mutating interfacial residues from hEMC1 (hEMC1^{F473Y+R487K}) showed a diametrically opposed phenotype in which B1AR was unaffected, increased SQS³⁷⁸⁻⁴¹⁰ levels, and TMEM97 levels markedly decreased (Figure 6G). Another mutation in this brace (hEMC1^{M483A+R487H+Q491N}) resulted in a decrease in TMEM97 and no significant effect on the other two client reporters. An adjacent hEMC5^{D44K} mutations in the interfacial brace had yet

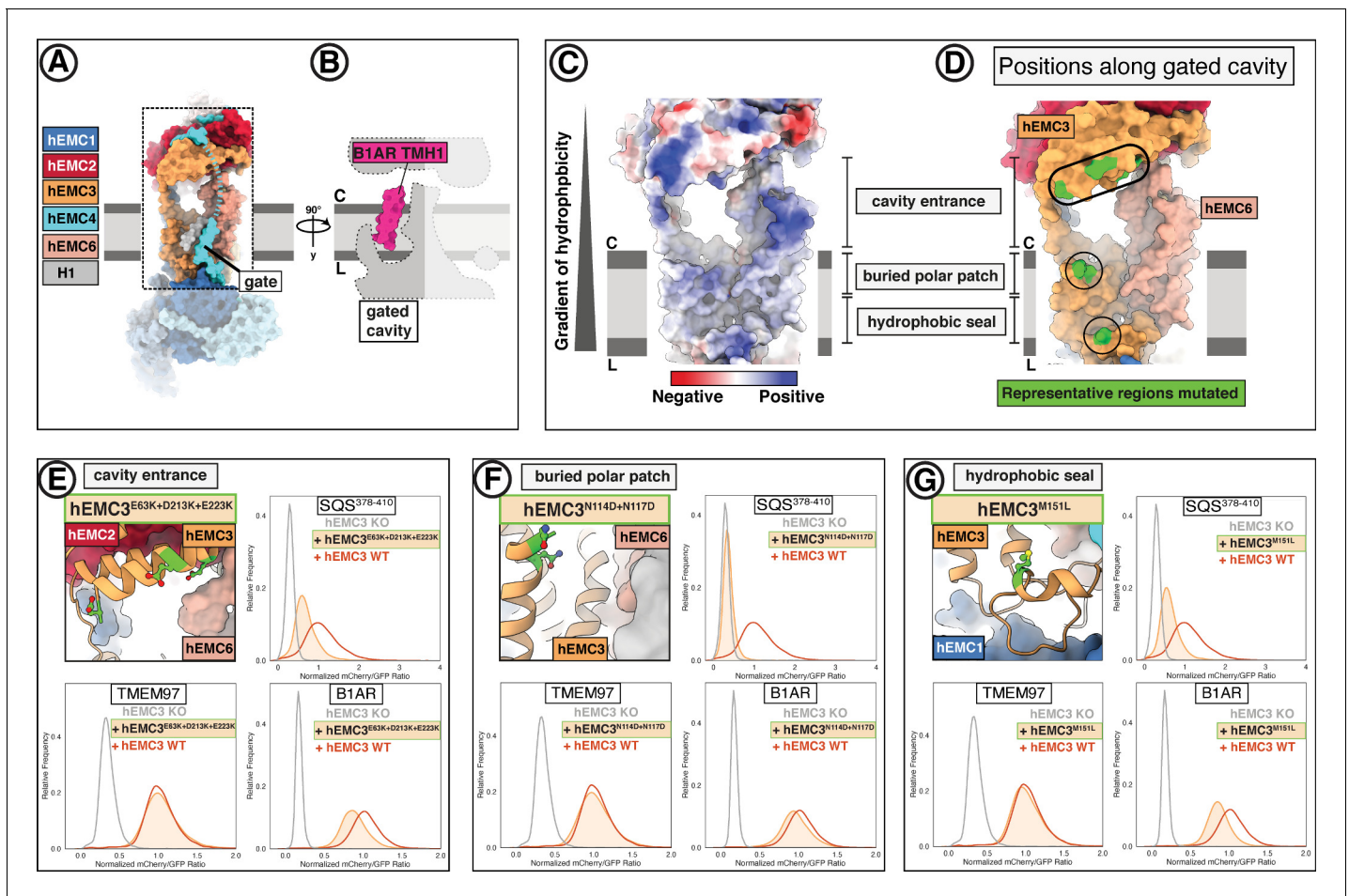


Figure 5. EMC houses an insertase module centered on EMC3 in the gated membrane cavity. (A) A transmembrane gate anchored in the cytosol and the lumen is a structural hallmark of the EMC gated cavity. Shown is a surface rendering of the hEMC model in lipid nanodiscs with an unresolved EMC4 connection between the cytoplasm and the membrane depicted as a dashed line. An unassigned helix of the gate is shown in gray (H1). (B) The gated cavity in the hEMC nanodisc structure has sufficient space to accommodate a client transmembrane helix. The space-filling model of the first transmembrane helix of B1AR (B1AR TMH1) is shown placed inside an outline of the EMC gated cavity. (C) A hydrophobic gradient characterizes the surface of the EMC gated cavity from the cytoplasmic to the luminal side. Gate helices have been omitted for clarity. The surface of the hEMC nanodisc structure is colored by electrostatic surface potential ranging from -15 (red) to $+15$ (blue) kcal/(mol·e). (D) Distinct EMC3 regions along the gated cavity hydrophobic gradient targeted for mutagenesis. Mutated residues are colored in lime. (E) Fluorescent client reporter stability assay for the EMC3 cavity entrance mutant, hEMC3^{E63K+D213K+E223K}. (F) As in (E) for the EMC3 buried polar patch mutant, hEMC3^{N114D+N117D}. (G) As in (E) for the EMC3 hydrophobic seal mutant, hEMC3^{M151L}.

The online version of this article includes the following figure supplement(s) for figure 5:

Figure supplement 1. Flow cytometry of gated cavity mutants.

Figure supplement 2. Additional flow cytometry of gated cavity mutants.

Figure supplement 3. Comparison of EMC3 to YidC-family members.

Figure supplement 4. Resolved lipid densities in hEMC and yEMC nanodisc maps.

Figure supplement 5. Comparison of gate conformations.

different resulting client flow cytometry profiles, with an increase in SQS³⁷⁸⁻⁴¹⁰ and no effect on either of the polytopic client reporters (Figure 6—figure supplement 2B–C). The pleiotropic client phenotypes across the panel of interfacial brace mutants suggest that this feature is critical for multiple EMC functions.



Video 2. EMC transmembrane cavity gate conformations. Overview of hEMC colored and labeled by subunit. Volume fades away to hEMC nanodisc model. hEMC nanodisc model remains constant as segmented maps of the unassigned gate helices are shown of hEMC detergent, yEMC detergent, and yEMC nanodisc maps. hEMC is colored cyan, yEMC is colored dark cyan, and gate helices are colored in shades of gray and purple as indicated by the label on the left. Two residues are shown in stick representation colored gold.

<https://elifesciences.org/articles/62611#video2>

anchored via the embedding of EMC4's C-terminus within the membrane-proximal EMC1 propeller. The lipid-filled cavity is connected to the ER luminal domain via the amphipathic EMC1 brace helix, which is tethered to the membrane-proximal EMC1 beta-propeller. The connections between the luminal domain and the transmembrane cavities could allow for conformational coupling during client handling. Indeed, superimposing the two conformations presented above, the open- and closed-gate states, revealed not only differences in the transmembrane domain but also a rotation of the luminal domain relative to the membrane cavities (**Video 3**). The luminal positioning is consistent for all three of our closed-gate conformation reconstructions (hEMC detergent, yEMC nanodisc, yEMC detergent). By contrast, the one map with an open gated cavity displayed a luminal rotation and concomitant shifts in position of the hEMC1 brace helix (**Figure 7—figure supplement 1**). Indeed, our set of interfacial hEMC1 brace mutants described above (**Figure 6F–G**, **Figure 6—figure supplement 2B–C**), showed differing client phenotypes when mutated from either the hEMC1 or the hEMC5 side. This suggests a complex conformational interplay between luminal and transmembrane domains during the engagement of diverse client types.

We investigated several known disease mutations in both conserved and human-specific regions of hEMC1 (**Figure 7C–D**, **Figure 7—figure supplements 2–3**; **Harel et al., 2016**; **Abu-Safieh et al., 2013**; **Amberger et al., 2019**). One of these disease-associated residues sits near the anchor point for the luminal hEMC4 transmembrane gate helix (hEMC1^{R881C}), while the majority are found farther from the membrane (hEMC1^{G868R}, hEMC1^{A144T}, hEMC1^{T82M}) (**Figure 7C–D**, **Figure 7—figure supplement 2B**). Incorporating each of these disease mutations into our EMC functional assay resulted in lower levels of the N-cytoplasmic polytopic client (TMEM97) and an increase in the level of the tail-anchored client (SQS^{378–410}), discussed in more detail below.

Two different hEMC1 mutants associated with cerebellar atrophy, visual impairment, and psychomotor retardation (hEMC1^{T82M}, hEMC1^{G868R}) map to the hinge region between the hEMC1 beta propellers where hEMC7 binds (**Figure 7D**). Both the mutants at this protein-protein interface resulted in depletion of the N-cytoplasmic polytopic client (TMEM97). EMC7 and EMC10 form beta-sandwich domains on either side of the membrane-proximal beta-propeller of EMC1 and contact each other across the EMC1 surface. Consistent with our structures, coupling of these subunits is supported by the prior finding that in the absence of EMC7, EMC10 is also lost from the complex

The EMC luminal domain is crucial for the biogenesis of multi-pass transmembrane proteins

Composed primarily of EMC1, EMC7, and EMC10, the extensive EMC luminal domain (**Figure 7A**) is important for polytopic client biogenesis and interactions with luminal chaperones (**Luo et al., 2002**; **Shurtleff et al., 2018**; **Hiramatsu et al., 2019**; **Coelho et al., 2019**). EMC7 and EMC10 are scaffolded on two beta-propellers of EMC1, one distal and the other proximal to the membrane. The luminal cap differs between hEMC and yEMC, with a four-bladed distal beta-propeller in yeast and eight-bladed distal propeller the human complex (**Figure 7B**). All three luminal EMC subunits have structural folds known to participate in protein-protein interactions (**Reinisch and De Camilli, 2016**). Mutations in this luminal domain have been linked to loss of the EMC complex (**Bircham et al., 2011**), a trafficking delay for membrane protein Pma1 (**Luo et al., 2002**), and male infertility (**Zhou et al., 2018**).

Several regions of the luminal domain form stabilizing interactions with the membrane cavities. The gate helices of the gated cavity are

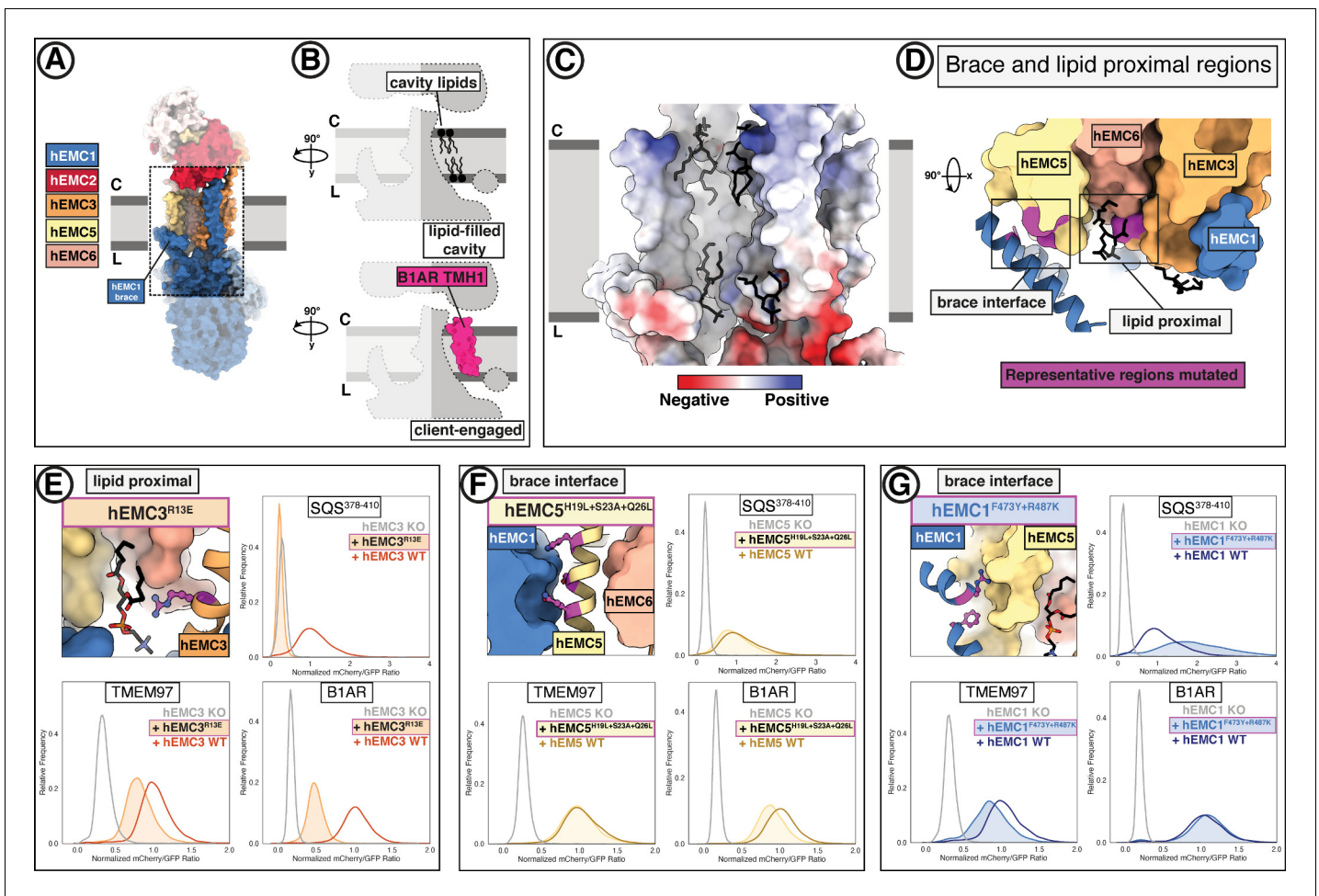


Figure 6. A lipid-filled cavity in the EMC transmembrane domain stabilizes disparate client proteins. (A) An EMC1 amphipathic brace helix delineates the boundary of the lipid-filled transmembrane cavity and packs against EMC5. Shown is a surface rendering of the hEMC model in nanodiscs. EMC4, EMC5, EMC6, and EMC1 subunits all contribute to the cavity lining. (B) The lipid-filled cavity in the hEMC nanodisc is occupied by several lipid molecules. Cartoon outlines of the gated cavity illustrate that the cavity could in principle allow for occupancy of a client helix (B1AR TMH1), possibly by lipid displacement or movement of the EMC1 brace helix. (C) The lipid-filled cavity has a uniform hydrophobic lining. Shown is an electrostatic surface rendering of the hEMC nanodisc structure colored as in **Figure 5C**. The cytoplasm-membrane interface contains positively charged residues and the luminal interface contains negatively charged residues. Modeled phospholipid molecules are displayed in black. (D) Lipid-proximal and brace interface residues targeted for mutagenesis. Selected regions targeted for mutagenesis are colored in magenta and include brace interface mutations both in EMC1 and EMC5, as well as a lipid-proximal residue in EMC3. (E) Fluorescent client reporter stability assay for the hEMC3^{R13E} mutant, which is in close proximity to a modeled POPC molecule. (F) As in (E) for the hEMC5^{H19L+S23A+Q26L} mutant, which sits at the interface to the EMC1 amphipathic brace helix. (G) As in (E) for the hEMC1^{F473Y+R487K} mutant, which sits at the interface to the EMC5 transmembrane helices.

The online version of this article includes the following figure supplement(s) for figure 6:

Figure supplement 1. Flow cytometry of lipid-filled cavity mutants.

Figure supplement 2. Additional flow cytometry of lipid-filled cavity mutants.

while the other EMC components appear unaffected (*Shurtleff et al., 2018*). EMC7 and EMC10 have been proposed to be auxiliary components with weaker phenotypes compared to core EMC subunits (*Jonikas et al., 2009; Shurtleff et al., 2018; Dickinson et al., 2016*). Upon deleting yEMC7, multi-pass transmembrane clients are retained in the ER but tail-anchored clients, including SQS-homolog Erg9, decrease in abundance (*Shurtleff et al., 2018*).

Several features of our data suggest dynamic association of hEMC7. Density for the hEMC7 beta-sandwich at the hinge between the two hEMC1 beta propellers was relatively weak in the consensus hEMC nanodisc map (**Figure 2—figure supplement 4**). Additional rounds of 3D classification revealed two distinct classes, one with clear density for hEMC7, and one with weak density in this

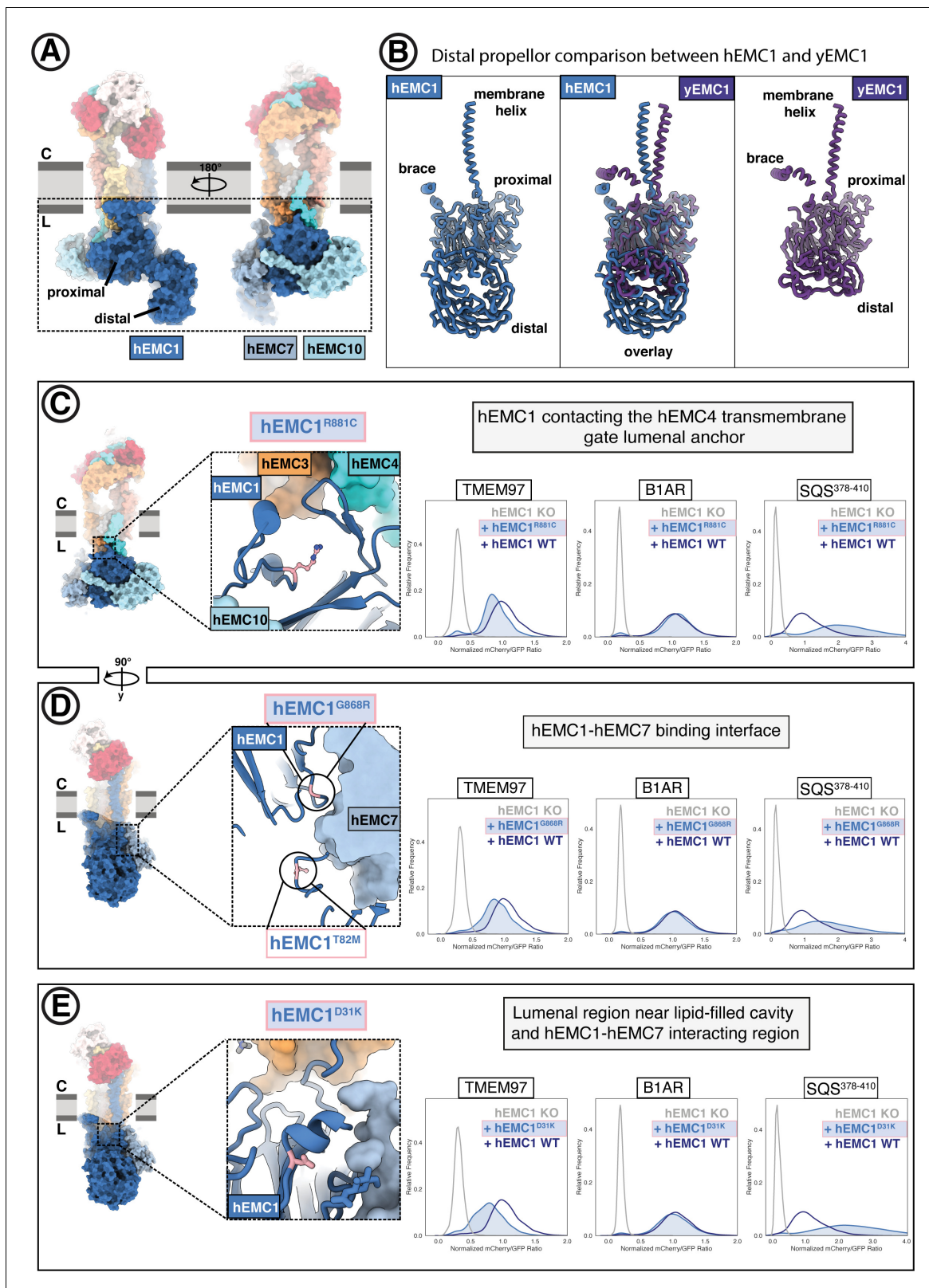


Figure 7. The large EMC luminal domain is the site for several annotated disease mutations. (A) Two views of the hEMC nanodisc structure. Two beta propellers are present in EMC1, one proximal to the membrane and one distal. (B) EMC1 is the largest EMC subunit and differs in size between yeast and human. Shown are human EMC1 (nanodisc), an overlay of human and yeast EMC1 (both nanodisc), and yeast EMC1 (nanodisc). (C) The *Figure 7 continued on next page*

Figure 7 continued

hEMC1^{R881C} mutant sits near the EMC4 luminal gate anchor. Left: Location of the mutation (colored pink). Right: Fluorescent client R881C reporter stability assay for hEMC1. (D) As in (C) for the hEMC1^{G868R} mutant. (E) As in (C) for the hEMC1^{D31K} mutant.

The online version of this article includes the following figure supplement(s) for figure 7:

Figure supplement 1. Conformational heterogeneity of the hEMC luminal domain between detergent and nanodisc maps.

Figure supplement 2. Flow cytometry of luminal domain mutants.

Figure supplement 3. Additional flow cytometry of luminal domain mutants.

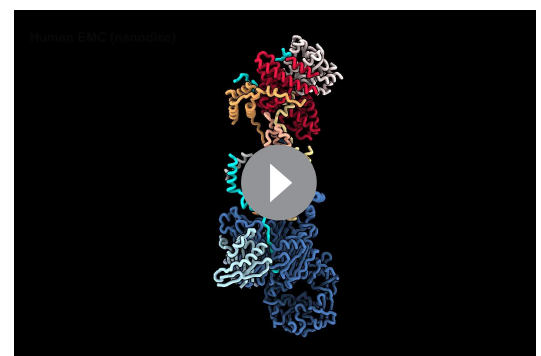
region. Mass spectrometric analysis of purified hEMC, however, revealed that the abundance of hEMC7 was similar to that of the other hEMC components (**Figure 1—figure supplement 2; Supplementary file 1**). Both reconstructions, with and without density for the hEMC7 luminal domain, displayed well-resolved density for hEMC10. Together, we conclude that hEMC7 is associated with hEMC1 in two different conformational states of hEMC7 with potentially distinct functions.

The OMIM database (**Amberger et al., 2019**) lists a mutation of unknown significance linked to retinitis pigmentosa (hEMC1^{A144T}) residing in the EMC1 distal propeller (**Figure 7—figure supplement 2**). Additionally, we also generated mutations in two surface exposed patches of the membrane-distal EMC1 beta-propeller projecting into the lumen (hEMC1^{D31K}, hEMC1^{R69D}, hEMC1^{G71S}, hEMC1^{H93D + E138D + N282K}, **Figure 7E, Figure 7—figure supplements 2–3**). Overall, these mutations displayed the same client effect: a decrease in the N-cytoplasmic polytopic client reporter (TMEM97), no change in the N-luminal polytopic client reporter (B1AR), and accumulation of the tail-anchored client reporter (SQS^{378–410}). Upon identifying antibodies against yEMC, we observed that the top two antibodies bind to a similar extended loop in the distal yEMC1 beta-propeller, perhaps suggesting that this site is accessible for co-factor binding in the ER. Intriguingly, this region of the luminal domain corresponds to the region where hEMC1 has an expanded distal beta-propeller. Taken together, the data provide evidence that the luminal domain is functionally coupled to the broader EMC role in transmembrane client stabilization. Moreover, these data support that the EMC is acting as a holdase chaperone to shield polytopic clients from degradation while they are folding to their functional form.

Discussion

Our collection of yeast and human EMC structures revealed the intricate and dynamic architecture of this multifunctional transmembrane molecular machine. The structures served as the starting point for our systematic dissection of EMC's multifaceted functions by exploring the impact of structure-based mutations on the ability of the EMC to support the biogenesis of representative members of three classes of membrane proteins: SQS, a tail-anchored protein, which exploits EMC's C-terminal insertase activity; B1AR, which relies on EMC's N-terminal insertase activity; and TMEM97, a polytopic membrane protein, which depends on the EMC for its biogenesis but does not rely on either of EMC's terminal insertase activities. Our data revealed that a conserved dual membrane cavity architecture supports the biogenesis of this diverse panel of transmembrane clients.

Overall, our studies present a nuanced picture of EMC's multifunctionality, revealing structural regions that differentially impact production of the three distinct client types. Unexpectedly, we also find that alterations to either the cytoplasmic or luminal domain of EMC lead to enhanced abundance of the TA



Video 3. hEMC luminal domain differences between nanodisc and detergent models. Overview of hEMC nanodisc model colored and labeled by subunit. Structural landmarks are labeled. hEMC detergent model (colored gray) fades in and both models rotate. As the models rotate several structural features are highlighted.

<https://elifesciences.org/articles/62611#video3>

substrate. Moreover, our work provides a foundational framework for understanding how discrete yet allosterically coupled regions of the complex enable the multiple functions of the EMC to support membrane protein biogenesis. Taken together, these studies suggest a model in which the EMC differentially regulates the biogenesis of distinct membrane proteins, thereby contributing to cellular coordination of membrane protein abundance in accordance with physiological needs. We propose a model of the EMC functioning both as a terminal insertase as well as a holdase chaperone that is potentially modulated by post-translational modifications, lipid interactions, and protein-protein interactions (**Figure 8**). Here, we summarize our findings into a proposed model of EMC function for these three clients.

Terminal insertase clients require an embedded insertase module within the EMC

EMC3's fold at the interface between the cytoplasm and membrane forms the core of the gated cavity and is reminiscent of proteins from the YidC family of insertases (*Borowska et al., 2015; Dalbey and Kuhn, 2015; Anghel et al., 2017*). Indeed, mutations in either the cytoplasmic or transmembrane domains of EMC3 establish that these features are critical for terminal helix insertase activity. In light of our observation of multiple gate conformations, we speculate that these conformations modulate insertion and release into the ER membrane.

Notably, mutating the surface of the cytoplasmic cap, which extends beyond the EMC3 cytoplasmic helices toward EMC8/9, resulted in an unexpected increase in C-tail anchor client (SQS³⁷⁸⁻⁴¹⁰) abundance. Of the three clients analyzed, SQS was the only one to show enhanced levels. It is unclear if this enhancement is SQS-specific or representative more broadly of all post-translationally targeted EMC tail-anchored clients. Future studies will be required to address if this is due to regulated insertion of SQS by the EMC, parallel pathways for inserting SQS into the membrane (i.e. mediated by TRC40/GET), and/or slower cytoplasmic clearance of chaperone-bound SQS.

Post-translational insertase clients have previously been shown to be targeted to the ER by cytoplasmic chaperones (*Guna et al., 2018*). Structural analysis and coupled mutagenesis, from our and recent studies (*O'Donnell et al., 2020; Pleiner et al., 2020; Bai et al., 2020*), suggest that clients then engage the cytoplasmic domain of the EMC, the transmembrane gate opens, the terminal helix is inserted into the EMC-gated cavity, and then another conformational change would allow for release into the lipid bilayer (**Figure 8A–B**). Further studies are needed to establish the precise C-terminal client range, as most tail anchor clients have been shown to be inserted by the GET (in yeast) or WRB (in human) complexes (*Denic et al., 2013; Mateja and Keenan, 2018*).

Both EMC cavities have resolved lipids and are critical for client biogenesis

Both the N-terminal (B1AR) and C-terminal insertase (SQS) clients depend on the EMC-gated cavity. Indeed, both the SQS tail-anchored helix and the first transmembrane helix of B1AR are moderately hydrophobic, with polar residues near the cytoplasmic end of the transmembrane helix, and both showed a strong dependence on the gated cavity. Nevertheless, our panel of mutants revealed some notable differences in the handling of these two client types. B1AR showed more dependence than SQS on the lipid-filled cavity in contrast to mutants elsewhere in the complex. Consistent with this, a number of mutations, primarily in the gated cavity, show residues of importance to both SQS and B1AR. However, there are also a number of mutations that appear to only affect SQS. One possible reason could be due to differences in the mechanism of initial engagement: SQS is targeted to the ER by cytoplasmic chaperones, while B1AR is targeted by SRP. Another key difference is that B1AR is polytopic and needs to overcome the additional challenge of tertiary transmembrane packing to reach its folded state. This work provides support for a model where the EMC inserts both types of terminal transmembrane helices into the gated cavity with differences in initial targeting and perhaps release into the lipid environment (**Figure 8C–D**). Future work will address the interplay between B1AR synthesis and its co-translational engagement with the translocon to ascertain whether there is a direct handoff between the translocon and the EMC or the EMC acts post-translationally to insert the N-terminal helix of B1AR.

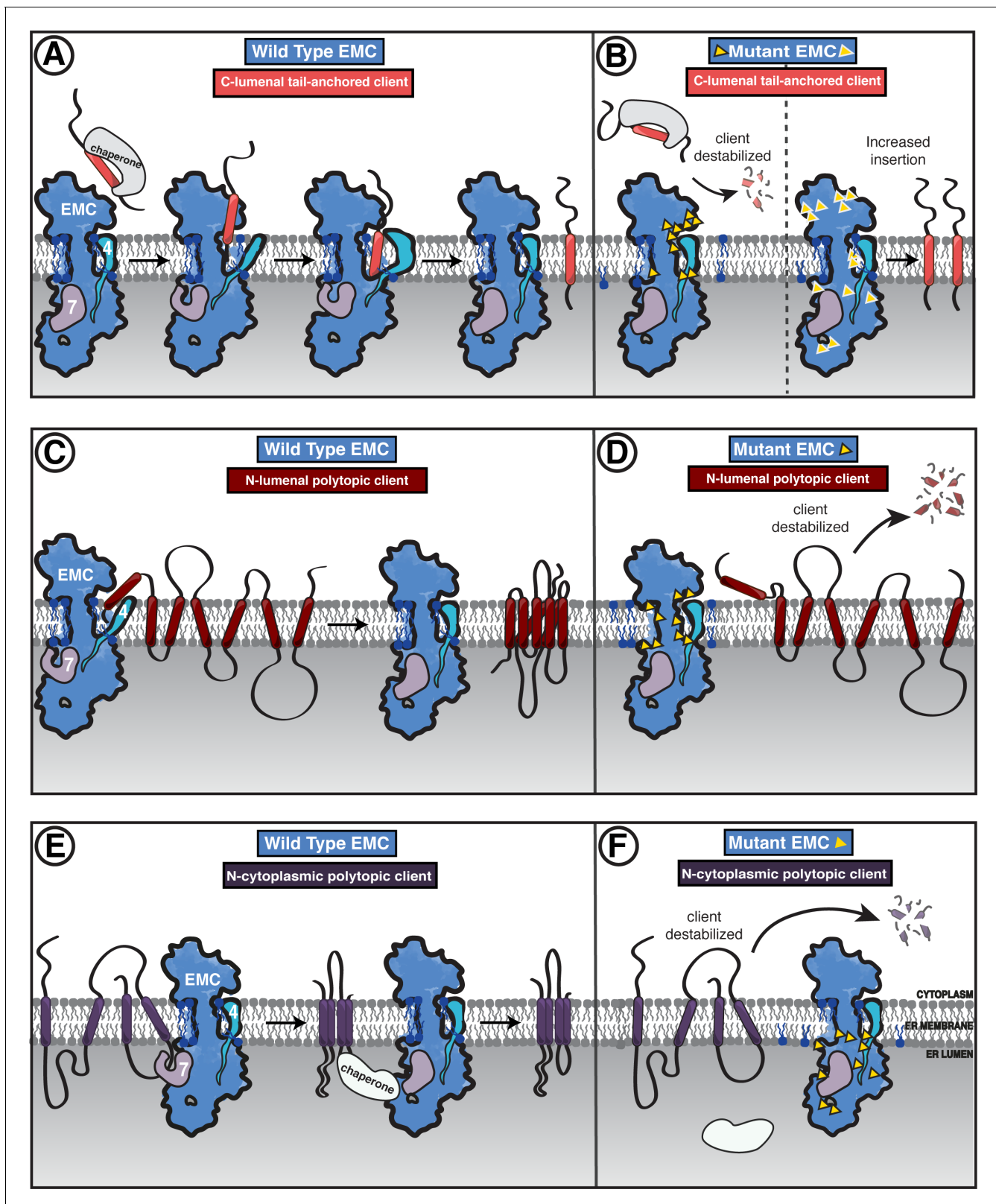


Figure 8. Model of coordinated EMC functions. (A) Model of EMC insertase function for a C-luminal tail-anchored client. Cytosolic factors bring post-translationally localized clients to the ER. Then the client engages the EMC cytoplasmic domain. The polar roof modulates entry into the gated cavity. A hydrophobic slide facilitates the client helix fully entering the cavity. A lateral movement of the gate releases the client helix into the membrane and the EMC gate closes. (B) Our mutagenesis data provide the following insights into EMC regions of functional importance for each of the three client types
 Figure 8 continued on next page

Figure 8 continued

we tested. Mutants are depicted by yellow triangles. Tail-anchored client (coral) abundance was depleted upon mutagenesis of the cytoplasmic domain entrance to the gated cavity, polar and charged residues at the cytoplasm-membrane boundary, residues along the length of the gated cavity, in the hydrophobic seal to the lumen, and lipid interacting residues in both cavities (left). We also observed a subset of mutants that resulted in higher levels of the C-luminal tail-anchored client (right) that are positioned in the cytoplasmic domain cap, throughout the ER luminal domain, and one mutation at the center of the gated cavity. (C) The EMC facilitates biogenesis of N-luminal polytopic client protein B1AR (dark red). (D) Regions important for B1AR stability primarily map to the transmembrane region of the EMC structure, with depletion observed for lipid proximal residues on both sides of the cavity, the polar entrance roof of the gated cavity, and the EMC1 brace helix. (E) The EMC facilitates biogenesis of N-cytoplasmic polytopic client protein TMEM97 (dark purple). (F) Regions important for TMEM97 stability were primarily located in the luminal domain spanning both propellers, in EMC1. In addition to these luminal regions, there was a depletion of TMEM97 at the lipid-interacting positions at the luminal interface of both membrane cavities of the EMC. Figure - Figure Supplement legends.

The EMC luminal domain orchestrates holdase chaperone function important for polytopic clients

Unlike the two terminal insertase clients we investigated, TMEM97 biogenesis was negatively impacted by mutation of the luminal EMC1. The depletion of TMEM97 observed in these mutant backgrounds is consistent with the luminal domain contributing to a holdase chaperone function, passively shielding its client while it is being synthesized and/or folded (Zhang *et al.*, 2017). Interestingly, the diametrically opposed phenotype of mutants in the EMC luminal domain on SQS raises the possibility that occupancy by one type of client can support an EMC conformation that is unfavorable for receiving the other. Alternative conformations could establish competition between client types for EMC occupancy. One explanation for this observation is that there is a conformational change between the insertase-active versus the holdase-active states. Interestingly, we identified at least two EMC conformations in our collection of structures, and EMC may adopt different conformations in various client and cofactor-engaged states.

In yeast, the polytopic clients co-purifying with the EMC are also glycosylated. One possible model is that the putative carbohydrate-binding domains in EMC7 or EMC10 directly contribute to engagement with client proteins. We speculate post-translational modifications on clients and the EMC could modulate function including client binding, chaperone binding, or regulating signaling in response to cellular cues.

Multi-pass transmembrane proteins require membrane factors to assist after insertion into the membrane to pack transmembrane helices in the correct order and topology. We propose that the EMC may act as a chaperone holdase to facilitate one of the following: helix and lipid packing, shielding from degradation while synthesis is in progress, or assisting in the assembly of multi-protein transmembrane complex formation. This is consistent with observations that in the absence of the EMC numerous integral membrane proteins are degraded (Shurtleff *et al.*, 2018; Volkmar *et al.*, 2019; Tian *et al.*, 2019). Direct interactions with multi-pass transmembrane proteins have been shown previously (Shurtleff *et al.*, 2018; Coelho *et al.*, 2019). Furthermore, EMC dependence of internal transmembrane domain segments has also been established (Ngo *et al.*, 2019; Hiramatsu *et al.*, 2019). In the absence of yEMC7, a primarily luminal subunit, a polytopic membrane protein was retained for longer in the ER, suggesting the possibility that yEMC7 may be involved in client release from the EMC. We propose a model where the EMC engages polytopic clients either during or directly after translation and remains bound until the client is released either to the membrane environment directly or handed off to client-specific and general ER chaperones (Figure 8E–F). It remains to be seen whether these polytopic clients directly engage with the lipid-filled cavity or the gated cavity or the lumen domain, what the determinants for engaging with a client or release into the membrane are, and how the EMC fits into the broader ER luminal chaperone network.

Potential role of the EMC as a master regulator of membrane protein biogenesis as the basis for its pleiotropic phenotypes

Why does the cell use a multifunctional EMC molecular machinery rather than specialized machinery for each of the functions encompassed by the EMC? Considering that the cell already has general machinery (Sec61 translocon) and tail-anchor insertase machinery (GET/TRC complex), we speculate that the EMC coordinates biogenesis of diverse membrane proteins. Several observations suggest

broader roles of the EMC as an integrator of information sensing the protein and lipid environment and coordinating its multiple activities, including the regulating the biogenesis of membrane proteins. For example, the initial identification of the EMC included numerous genetic interactions with both protein and lipid synthesis factors in yeast (*Jonikas et al., 2009*) and these disparate interdependencies have been subsequently observed in numerous species including human EMC (*Lahiri et al., 2014; Tang et al., 2017; Guna et al., 2018; Volkmar et al., 2019; Volkmar and Christianson, 2020*). Also, several client proteins are enzymes or cofactors involved in multiple stages of lipid synthesis or trafficking, and this may provide a unifying explanation for the range of genetic interactions and co-essentiality observations reported to date (*Guna et al., 2018; Shurtleff et al., 2018; Volkmar et al., 2019; Tian et al., 2019; Wainberg et al., 2019; Corradi et al., 2019; Volkmar and Christianson, 2020*). Perhaps by facilitating the insertion of sterol synthesis protein SQS, the EMC allows for modulation of local membrane thickness and lipid composition to accommodate differences within the broad range of membrane proteins being synthesized. In this regard, one structural feature of particular interest is the EMC1 amphipathic brace, which resides adjacent to the lipid-filled cavity. This conserved feature sits within the interfacial membrane boundary, raising the possibility that it can modulate the lipid or protein composition of this cavity. Notably, several other membrane proteins involved in ER homeostasis, including Opi1 and Ire1, also contain amphipathic helices that have been proposed to sense the properties of the lipid bilayer (*Volmer et al., 2013; Jacquemyn et al., 2017; Halbleib et al., 2017; Hofbauer et al., 2018; Cho et al., 2019*). Future work will explore how the EMC overall, and the EMC1 brace helix in particular, govern client release into the membrane, interface with the local structure of the lipid bilayer, and play roles in specific client-lipid interactions.

In addition to the three client classes we investigate here, it is clear that EMC has a broader range of clients including multi-protein assemblies (*Richard et al., 2013; Talbot et al., 2019*), lipid-modulating proteins (*Volkmar et al., 2019*), lipid-binding proteins (*Salas-Estrada et al., 2018; Sejdiu and Tieleman, 2020*), and those with helices that do not span the bilayer (*Lin et al., 2019; Ngo et al., 2019*). The compartmentalization and interdependence that we observe for effects of mutations on client handling provide a foundation for understanding this multifunctionality. We propose that the complexity of the EMC machine, combining insertase and holdase chaperone functions within one molecular machine, has arisen to mitigate the error prone biogenesis of a diverse range of membrane spanning proteins in the dynamic environment of the ER.

Materials and methods

Key resources table

Reagent type (species) or resource	Designation	Source or reference	Identifiers	Additional information
Gene (<i>Homo sapiens</i>)	hEMC1	NIH Mammalian Gene Collection	NCBI: BC034589	
Gene (<i>Homo sapiens</i>)	hEMC2	NIH Mammalian Gene Collection	NCBI: BC021667	
Gene (<i>Homo sapiens</i>)	hEMC3	NIH Mammalian Gene Collection	NCBI: BC022807	
Gene (<i>Homo sapiens</i>)	hEMC4	Genestrand (Eurofins, Germany)	Uniprot: Q5J8M3-1	
Gene (<i>Homo sapiens</i>)	hEMC5	NIH Mammalian Gene Collection	NCBI: BC033588	
Gene (<i>Homo sapiens</i>)	hEMC6	NIH Mammalian Gene Collection	NCBI: BC001409	
Gene (<i>Homo sapiens</i>)	hEMC7	NIH Mammalian Gene Collection	NCBI: BC104936	
Gene (<i>Homo sapiens</i>)	hEMC8	NIH Mammalian Gene Collection	NCBI: BC020250	
Gene (<i>Homo sapiens</i>)	hEMC9	NIH Mammalian Gene Collection	NCBI: BC002491	

Continued on next page

Continued

Reagent type (species) or resource	Designation	Source or reference	Identifiers	Additional information
Gene (<i>Homo sapiens</i>)	hEMC10	Genestrand (Eurofins, Germany)	Uniprot: Q5UCC4-1	
Gene (<i>Saccharomyces cerevisiae</i>)	yEMC1	Uniprot	Uniprot: P25574	
Gene (<i>Saccharomyces cerevisiae</i>)	yEMC2	Uniprot	Uniprot: P47133	
Gene (<i>Saccharomyces cerevisiae</i>)	yEMC3	Uniprot	Uniprot: P36039	
Gene (<i>Saccharomyces cerevisiae</i>)	yEMC4	Uniprot	Uniprot: P53073	
Gene (<i>Saccharomyces cerevisiae</i>)	yEMC5	Uniprot	Uniprot: P40540	
Gene (<i>Saccharomyces cerevisiae</i>)	yEMC6	Uniprot	Uniprot: Q12431	
Gene (<i>Saccharomyces cerevisiae</i>)	yEMC7	Uniprot	Uniprot: P39543	
Gene (<i>Saccharomyces cerevisiae</i>)	yEMC10	Uniprot	Uniprot: Q12025	
Recombinant DNA reagent	pX458	Addgene	pX458	
Recombinant DNA reagent	pKDP041	This study; available from the Weissman Lab	Cas9-sfGFP-EMC5 sgRNA3	single guide KO system targeting EMC5 gene
Recombinant DNA reagent	pKDP077	This study; available from the Weissman Lab	Cas9-sfGFP-EMC1_sRNA3_sRNA4	dual guide KO system targeting EMC1 gene
Recombinant DNA reagent	pKDP080	This study; available from the Weissman Lab	Cas9-sfGFP-EMC2_sRNA4_sRNA5	dual guide KO system targeting EMC2 gene
Recombinant DNA reagent	pKDP083	This study; available from the Weissman Lab	Cas9-sfGFP-EMC3_sRNA1_sRNA2	dual guide KO system targeting EMC3 gene
Recombinant DNA reagent	pKDP119	This study; available from the Weissman Lab	SFFV-insert site-IRES-Puro-P2A-BFP	parental vector
Recombinant DNA reagent	pKDP121	This study; available from the Weissman Lab	pTwist+Lenti+SFFV+EMC1+IRES+Puro+P2A+BFP+WPRE	EMC1 covering plasmid
Recombinant DNA reagent	pKDP122	This study; available from the Weissman Lab	pTwist+Lenti+SFFV+EMC3+IRES+Puro+P2A+BFP+WPRE	EMC3 covering plasmid
Recombinant DNA reagent	pKDP124	This study; available from the Weissman Lab	pTwist+Lenti+SFFV+EMC5+IRES+Puro+P2A+BFP+WPRE	EMC5 covering plasmid
Recombinant DNA reagent	pKDP125	This study; available from the Weissman Lab	pTwist+Lenti+SFFV+EMC2+IRES+Puro+P2A+BFP+WPRE	EMC2 covering plasmid
Recombinant DNA reagent	pKDP110	This study; available from the Weissman Lab	bAR1_mCherry_P2A_GFP	See Supplementary file 5 for sequence
Recombinant DNA reagent	pKDP111	This study; available from the Weissman Lab	TMEM97_mCherry_P2A_GFP	See Supplementary file 5 for sequence
Recombinant DNA reagent	pKDP136	This study; available from the Weissman Lab	GFP_P2A_mCherry_SQS_TMD_opsintag	See Supplementary file 5 for sequence
Recombinant DNA reagent	pKDP119_hsEMC1_mut_D31K	Twist; available from the Weissman Lab	hsEMC1_mut_D31K	See Supplementary file 5 for sequence
Recombinant DNA reagent	pKDP119_hsEMC1_mut_R69D	Twist; available from the Weissman Lab	hsEMC1_mut_R69D	See Supplementary file 5 for sequence
Recombinant DNA reagent	pKDP119_hsEMC1_mut_G71S	Twist; available from the Weissman Lab	hsEMC1_mut_G71S	See Supplementary file 5 for sequence

Continued on next page

Continued

Reagent type (species) or resource	Designation	Source or reference	Identifiers	Additional information
Recombinant DNA reagent	pKDP119_hsEMC1_mut_R76D_K80D	Twist; available from the Weissman Lab	hsEMC1_mut_R76D_K80D	See Supplementary file 5 for sequence
Recombinant DNA reagent	pKDP119_hsEMC1_mut_T82M	Twist; available from the Weissman Lab	hsEMC1_mut_T82M	See Supplementary file 5 for sequence
Recombinant DNA reagent	pKDP119_hsEMC1_mut_T82A	Twist; available from the Weissman Lab	hsEMC1_mut_T82A	See Supplementary file 5 for sequence
Recombinant DNA reagent	pKDP119_hsEMC1_mut_A144T	Twist; available from the Weissman Lab	hsEMC1_mut_A144T	See Supplementary file 5 for sequence
Recombinant DNA reagent	pKDP119_hsEMC1_mut_H93D_E138D_N282K	Twist; available from the Weissman Lab	hsEMC1_mut_H93D_E138D_N282K	See Supplementary file 5 for sequence
Recombinant DNA reagent	pKDP119_hsEMC1_mut_R275E_R404E	Twist; available from the Weissman Lab	hsEMC1_mut_R275E_R404E	See Supplementary file 5 for sequence
Recombinant DNA reagent	pKDP119_hsEMC1_mut_G471R	Twist; available from the Weissman Lab	hsEMC1_mut_G471R	See Supplementary file 5 for sequence
Recombinant DNA reagent	pKDP119_hsEMC1_mut_F473Y_R487K	Twist; available from the Weissman Lab	hsEMC1_mut_F473Y_R487K	See Supplementary file 5 for sequence
Recombinant DNA reagent	pKDP119_hsEMC1_mut_M483A_R487H_Q491N	Twist; available from the Weissman Lab	hsEMC1_mut_M483A_R487H_Q491N	See Supplementary file 5 for sequence
Recombinant DNA reagent	pKDP119_hsEMC1_mut_G868R	Twist; available from the Weissman Lab	hsEMC1_mut_G868R	See Supplementary file 5 for sequence
Recombinant DNA reagent	pKDP119_hsEMC1_mut_R881C	Twist; available from the Weissman Lab	hsEMC1_mut_R881C	See Supplementary file 5 for sequence
Recombinant DNA reagent	pKDP119_hsEMC1_mut_K951A_K957A	Twist; available from the Weissman Lab	hsEMC1_mut_K951A_K957A	See Supplementary file 5 for sequence
Recombinant DNA reagent	pKDP119_hsEMC2_mut_K18A_K21A	Twist; available from the Weissman Lab	hsEMC2_mut_K18A_K21A	See Supplementary file 5 for sequence
Recombinant DNA reagent	pKDP119_hsEMC2_mut_R80A_R81A_K90A_R112A	Twist; available from the Weissman Lab	hsEMC2_mut_R80A_R81A_K90A_R112A	See Supplementary file 5 for sequence
Recombinant DNA reagent	pKDP119_hsEMC2_mut_K125E_R126D_K127E	Twist; available from the Weissman Lab	hsEMC2_mut_K125E_R126D_K127E	See Supplementary file 5 for sequence
Recombinant DNA reagent	pKDP119_hsEMC2_mut_N137A_N167A	Twist; available from the Weissman Lab	hsEMC2_mut_N137A_N167A	See Supplementary file 5 for sequence
Recombinant DNA reagent	pKDP119_hsEMC2_mut_E146A_E149A_Q150A	Twist; available from the Weissman Lab	hsEMC2_mut_E146A_E149A_Q150A	See Supplementary file 5 for sequence
Recombinant DNA reagent	pKDP119_hsEMC2_mut_E168A_D170A_K173A	Twist; available from the Weissman Lab	hsEMC2_mut_E168A_D170A_K173A	See Supplementary file 5 for sequence
Recombinant DNA reagent	pKDP119_hsEMC2_mut_E206A_E209A_D252A	Twist; available from the Weissman Lab	hsEMC2_mut_E206A_E209A_D252A	See Supplementary file 5 for sequence
Recombinant DNA reagent	pKDP119_hsEMC2_mut_K248E_D252K_K255E	Twist; available from the Weissman Lab	hsEMC2_mut_K248E_D252K_K255E	See Supplementary file 5 for sequence
Recombinant DNA reagent	pKDP119_hsEMC2_mut_R266A_Q269A_R273A	Twist; available from the Weissman Lab	hsEMC2_mut_R266A_Q269A_R273A	See Supplementary file 5 for sequence
Recombinant DNA reagent	pKDP119_hsEMC2_mut_Q269A_E286A_E290A	Twist; available from the Weissman Lab	hsEMC2_mut_Q269A_E286A_E290A	See Supplementary file 5 for sequence
Recombinant DNA reagent	pKDP119_hsEMC3_WT	Twist; available from the Weissman Lab	hsEMC3_WT	See Supplementary file 5 for sequence
Recombinant DNA reagent	pKDP119_hsEMC3_mut_D9A	Twist; available from the Weissman Lab	hsEMC3_mut_D9A	See Supplementary file 5 for sequence
Recombinant DNA reagent	pKDP119_hsEMC3_mut_R13E	Twist; available from the Weissman Lab	hsEMC3_mut_R13E	See Supplementary file 5 for sequence

Continued on next page

Continued

Reagent type (species) or resource	Designation	Source or reference	Identifiers	Additional information
Recombinant DNA reagent	pKDP119_hsEMC3_mut_K42A_K43A	Twist; available from the Weissman Lab	hsEMC3_mut_K42A_K43A	See Supplementary file 5 for sequence
Recombinant DNA reagent	pKDP119_hsEMC3_mut_E63K_D213K_E223K	Twist; available from the Weissman Lab	hsEMC3_mut_E63K_D213K_E223K	See Supplementary file 5 for sequence
Recombinant DNA reagent	pKDP119_hsEMC3_mut_K70Y	Twist; available from the Weissman Lab	hsEMC3_mut_K70Y	See Supplementary file 5 for sequence
Recombinant DNA reagent	pKDP119_hsEMC3_mut_V118A_I122A	Twist; available from the Weissman Lab	hsEMC3_mut_V118A_I122A	See Supplementary file 5 for sequence
Recombinant DNA reagent	pKDP119_hsEMC3_mut_N114D_N117D	Twist; available from the Weissman Lab	hsEMC3_mut_N114D_N117D	See Supplementary file 5 for sequence
Recombinant DNA reagent	pKDP119_hsEMC3_mut_R180A	Twist; available from the Weissman Lab	hsEMC3_mut_R180A	See Supplementary file 5 for sequence
Recombinant DNA reagent	pKDP119_hsEMC3_mut_R59E_R62E_K216E	Twist; available from the Weissman Lab	hsEMC3_mut_R59E_R62E_K216E	See Supplementary file 5 for sequence
Recombinant DNA reagent	pKDP119_hsEMC3_mut_R147E	Twist; available from the Weissman Lab	hsEMC3_mut_R147E	See Supplementary file 5 for sequence
Recombinant DNA reagent	pKDP119_hsEMC3_mut_F148L	Twist; available from the Weissman Lab	hsEMC3_mut_F148L	See Supplementary file 5 for sequence
Recombinant DNA reagent	pKDP119_hsEMC3_mut_M151L	Twist; available from the Weissman Lab	hsEMC3_mut_M151L	See Supplementary file 5 for sequence
Recombinant DNA reagent	pKDP119_hsEMC3_mut_I186V_I182V	Twist; available from the Weissman Lab	hsEMC3_mut_I186V_I182V	See Supplementary file 5 for sequence
Recombinant DNA reagent	pKDP119_hsEMC3_mut_K244A_H247A_E249A	Twist; available from the Weissman Lab	hsEMC3_mut_K244A_H247A_E249A	See Supplementary file 5 for sequence
Recombinant DNA reagent	pKDP119_hsEMC5_WT	Twist; available from the Weissman Lab	hsEMC5_WT	See Supplementary file 5 for sequence
Recombinant DNA reagent	pKDP119_hsEMC5_mut_A18L	Twist; available from the Weissman Lab	hsEMC5_mut_A18L	See Supplementary file 5 for sequence
Recombinant DNA reagent	pKDP119_hsEMC5_mut_D44K	Twist; available from the Weissman Lab	hsEMC5_mut_D44K	See Supplementary file 5 for sequence
Recombinant DNA reagent	pKDP119_hsEMC5_mut_D82A_R85A	Twist; available from the Weissman Lab	hsEMC5_mut_D82A_R85A	See Supplementary file 5 for sequence
Recombinant DNA reagent	pKDP119_hsEMC5_mut_F22L	Twist; available from the Weissman Lab	hsEMC5_mut_F22L	See Supplementary file 5 for sequence
Recombinant DNA reagent	pKDP119_hsEMC5_mut_E75A	Twist; available from the Weissman Lab	hsEMC5_mut_E75A	See Supplementary file 5 for sequence
Recombinant DNA reagent	pKDP119_hsEMC5_mut_H19L_S23A_Q26L	Twist; available from the Weissman Lab	hsEMC5_mut_H19L_S23A_Q26L	See Supplementary file 5 for sequence
Recombinant DNA reagent	pKDP119_hsEMC5_mut_K7A	Twist; available from the Weissman Lab	hsEMC5_mut_K7A	See Supplementary file 5 for sequence
Recombinant DNA reagent	pKDP119_hsEMC5_mut_K7E	Twist; available from the Weissman Lab	hsEMC5_mut_K7E	See Supplementary file 5 for sequence
Recombinant DNA reagent	pKDP119_hsEMC5_mut_R28A_R32A	Twist; available from the Weissman Lab	hsEMC5_mut_R28A_R32A	See Supplementary file 5 for sequence
Recombinant DNA reagent	pKDP119_hsEMC5_mut_I63L	Twist; available from the Weissman Lab	hsEMC5_mut_I63L	See Supplementary file 5 for sequence
Recombinant DNA reagent	pKDP119_hsEMC5_mut_F90A	Twist; available from the Weissman Lab	hsEMC5_mut_F90A	See Supplementary file 5 for sequence
Antibody	Mouse GAPDH Primary Antibody	Abcam	ab8245	See Supplementary file 5 for sequence
Antibody	Rabbit TMEM97 primary	ThermoFisher Scientific	PA-23003	

Continued on next page

Continued

Reagent type (species) or resource	Designation	Source or reference	Identifiers	Additional information
Antibody	Rabbit FDFT1 Primary Antibody	Abcam	ab195046	
Antibody	Rat BAP31 Primary Antibody	ThermoFisher Scientific	MA3-002	
Antibody	Rabbit (KIAA0090) EMC1 primary antibody	Abcam	ab242112	
Antibody	Rabbit TTC35 (EMC2) primary antibody	Proteintech	25443-1-AP	
Antibody	Rabbit TM111 (EMC3) primary antibody	ThermoFisher Scientific	#711771	
Antibody	Rabbit EMC4 primary antibody	Abcam	ab184544	
Antibody	Rabbit MGMT1 (EMC5) primary antibody	Bethyl Laboratories	A305-833A-M	
Antibody	Rabbit (C19orf63) EMC10 primary antibody	Abcam	ab180148	
Antibody	IRDye 800CW Goat anti-Mouse IgG Secondary Antibody	LI-COR Biosciences	925-32210	
Antibody	IRDye 800CW Goat anti-Rabbit IgG Secondary Antibody	LI-COR Biosciences	926-32211	
Peptide, recombinant protein	Fab DE4	This study; available from the Weissman Lab	LMV83	LFAIPLVVPFYSHSALDWMQSPSLPV TPGEPASISCRSSQTLMNRRNGNNFLDW YVQKPGQSPQLLIYLGSNRAPGVPDRFS GSGSGTDFTLKISRLEVEDVGVYYCMQA LQTPRTFGQGTKEIKRTVAAPSVFIFPP SDEQLKSGTASVCLLNFFYPREAKVQW KVDNALQSGNSQESVTEQDSKDSYSL STLTLSKADYEKHKVYACEVTHQGLSSP VTKSFNRGEC- MAQVQLQQWGAGLLKPSETLSLTCAVYG GFSFGYYWSWIRQPPGKGLEWIGEINHS GSTNYPNPKSRVTISVDTSKQFSLKLS SVTAADTAVYYCARFSYGGIYWGQGT LTVSSASTKGPSVFPLAPSSKSTSGGTAA LGCLVKDYFPEPVTVSWNSGALTSVHT FPAVLQSSGLYSLSSVTPVSSSLGTQTYI CNVNHKPSNTKVDKVEPKSCAAAH HHHGAEEQKLISEEDLNAA-
Peptide, recombinant protein	Fab DH4	This study; available from the Weissman Lab	LMV82	LFAIPLVVPFYSHSALDWMQSPSLPV TPGEPASISCRSSQTLMNRRNGNNFLDW YLQKPGQSPQLLIYLGSNRAPGVPDRFS GSGSGTDFTLRISRVEPEDVGVYYCMQA LQTPSFGGGTKVEIRRTVAAPSVFIFPPS DEQLKSGTASVCLLNFFYPREAKVQW KVDNALQSGNSQESVTEQDSKDSYSL SSTLTLSKADYEKHKVYACEVTHQGLSS PVTGSFNRGEC- MAQVQLQQWGAGLLKPSETLSLTCAVY GGFSFGYYWSWIRQPPGKGLEWIGEIN HSGSTNYPNPKSRVTISVDTSKNQFSL KLSVTAADTAVYYCARGLAGRGGYGG SYLRWGQGTLVTVSSASTKGPSVFPLAP SSKSTSGGTAALGCLVKDYFPEPVTVSW NSGALTSVHTFPAVLQSSGLYSLSSV TPVSSSLGTQTYICNVNHKPSNTKVDK KVEPKSCAAAH HHHHHGAEE QKLISEEDLNAA-
Commercial assay or kit	Superose 6, 10/300 GL	GE Healthcare	17517201	

Continued on next page

Continued

Reagent type (species) or resource	Designation	Source or reference	Identifiers	Additional information
Commercial assay or kit	R1.2/1.3 200 and 300 mesh Cu holey carbon grids	Quantifoil	1210627	
Commercial assay or kit	BL21 Gold Star competent cells	Invitrogen	C602003	
Commercial assay or kit	Anti-Flag agarose beads	Millipore	A2220	
Commercial assay or kit	EconoPac Chromatography Columns	Biorad	7321010	
Commercial assay or kit	100 KD MW	EMD Millipore	UFC810024	
Commercial assay or kit	Superose 6, 10/300 GL	Cytiva	29-0915-96	
Commercial assay or kit	cOmplete EDTA-free Protease Inhibitor Cocktail	Roche	catalog No. 05056489001	
Commercial assay or kit	Bio-Beads	Biorad	1523920	
Commercial assay or kit	R1.2/1.3 200 and 300 mesh Cu holey carbon grids	Quantifoil	1210627	
Commercial assay or kit	Ultrathin Carbon Film on Lacey Carbon Support Film, 400 mesh, Copper	Ted Pella	#01824	
Chemical compound, drug	FuGENE HD transfection reagent	Promega	E2312	
Chemical compound, drug	1-Palmitoyl-2-oleoyl-sn-glycero-3-PC (POPC)	Cayman Chemical	15102	
Chemical compound, drug	Glyco-diosgenin (GDN)	Anatrace	GDN101	
Chemical compound, drug	yeast extract total	Avanti Polar Lipids	190000 P-100mg	
Chemical compound, drug	Cholesteryl Hemisuccinate Tris Salt	Anatrace	CH210 5 GM	
Chemical compound, drug	b-DDM	Anatrace	D310	
Chemical compound, drug	IPTG	GoldBio	I2481C5	
Chemical compound, drug	EX-CELL 420 Serum-Free Medium	Sigma-Aldrich	14420 C	
Chemical compound, drug	FreeStyle 293 Expression Medium	Thermo fischer	12338018	
Cell line (<i>Homo sapiens</i>)	HEK293S GnTI-	ATCC	CRL-3022	Mycoplasma negative
Cell line (<i>Spodoptera frugiperda</i>)	Sf9	Thermo Fischer	11496015	
Cell line (<i>Homo sapiens</i>)	K562 crispr	Gilbert et al., 2014	K562 crispr	

Continued on next page

Continued

Reagent type (species) or resource	Designation	Source or reference	Identifiers	Additional information
Strain, strain background <i>Saccharomyces cerevisiae</i>	Overexpressed EMC with yEMC5-linker-TEV-linker-3xFlag	This study; available from the Weissman Lab	LMV84	BY4743 — MATa/alpha, his3Δ0/his3Δ0, leu2Δ0/leu2Δ0, LYS2/lys2Δ0, met15Δ0/MET15, ura3Δ0/ura3Δ0, emc1::NatMX::TEF2pr-EMC1/EMC1, emc3::KanMX::TEF2pr-EMC3/EMC3, emc4::his3(CG)::TEF2pr-EMC4/EMC4, sop4::HphMx::TEF2pr-SOP4/SOP4, EMC2/emc2::NatMX::TEF2pr-EMC2, emc5::EMC5-TEV-3xFLAG::ura3(KL)/emc5::his3(CG)::TEF2pr-EMC5-TEV-3xFLAG::KanMX, EMC6/emc6::HphMX::TEF2pr-EMC6, YDR056c/ydr056c::leu2(CG)::TEF2pr-ydr056c
Strain, strain background <i>Saccharomyces cerevisiae</i>	Endogenous yEMC5-linker-TEV-linker-3xFlag	This study; available from the Weissman Lab	LMV85	W303 — EMC5-3xF:ura - Linker-TEV-linker-3xFlag (GGSGSGENLYFQSGSGS DYKDDDDKDYKDDDDKDYKDDDDK)
Software, algorithm	CryoSPARC version 2.12.4.	Punjani et al., 2017	RRID:SCR_016501	
Software, algorithm	UCSF ChimeraX Version 1.0	Goddard et al., 2018	RRID:SCR_015872	
Software, algorithm	PHENIX Version 1.17	Adams et al., 2011;	RRID:SCR_014224	
Software, algorithm	Coot Version 0.8	Emsley et al., 2010	RRID:SCR_014222	
Software, algorithm	RELION 3.1	Kimanius et al., 2016; Zivanov et al., 2018	http://www2.mrc.lmb.cam.ac.uk/relion	
Software, algorithm	SerialEM	Mastrorarde, 2005	RRID:SCR_017293	

Reagents used for experiments described and reagents made as part of this study are listed in a Key Resources Table listed as an appendix to this article file.

Cell line maintenance

K562 dCas9 KRAB cells were grown in RPMI 1640 (GIBCO) with 25 mM HEPES, 2 mM l-glutamine, 2 g/L NaHCO₃ and supplemented with 10% (v/v) fetal bovine serum (FBS), 100 units/mL penicillin, 100 μg/mL streptomycin, 2 mM l-glutamine. HEK293T cells were grown in Dulbecco's modified eagle medium (DMEM, GIBCO) with 25 mM d-glucose, 3.7 g/L NaHCO₃, 4 mM l-glutamine and supplemented with 10% (v/v) FBS, 100 units/mL penicillin, 100 μg/mL streptomycin. All cell lines were grown at 37°C. All cell lines were periodically tested for Mycoplasma contamination using the MycoAlert Plus Mycoplasma detection kit (Lonza).

DNA transfections and virus production

Lentivirus was generated by transfecting HEK39T cells with standard fourth-generation packaging vectors using TransIT-LT1 Transfection Reagent (Mirus Bio). Media was changed 10 hr post-transfection. Viral supernatant was harvested 60 hr after transfection, filtered through 0.45 μm PVDF filters and frozen prior to transduction.

Knockout hEMC cell lines

A single and dual knockout guide system was developed in the pX458 backbone (Addgene plasmid # 48138) with guides targeting hEMC1, hEMC2, hEMC3, or hEMC5 (Key Resources table). Targeting guides were selected using the Broad's guide selection tool (<https://portals.broadinstitute.org/gpp/public/analysis-tools/sgrna-design>). For the single hEMC5 knockout system, an hEMC5 targeting guide was cloned into pX458 by digesting with BbsI and ligating to annealed oligos for the hEMC5 sgRNA. For the dual knockout system, a four-step cloning process generated the final knockout

plasmid: (1) Each of the two guides targeting the same locus were individually cloned into pX458. (2) Then pX458_sgRNA1 was digested with XbaI. (3) SgRNA2 cassette from pX458_sgRNA2 was PCR amplified with oligos containing overhangs spanning the XbaI cloning site and purified. (4) Finally, the final dual guide vector was generated by Gibson cloning (NEBuilder).

To generate the hEMC knockout cell lines, K562 dCas9 KRAB cells were nucleofected with the respective hEMC knockout plasmids using Lonza SF Cell Line 96-well Nucleofector Kit (V4SC-2096). Two days post-nucleofection, GFP-positive cells were single cell sorted into 96-well plates using BD FACS ARIALL. After colonies from single cells grew out, genomic DNA was isolated using QuickExtract (Lucigen), the sgRNA-targeted sites were PCR amplified and then NGS-sequenced via Genewiz's EZ-Amplicon service. Sequencing data was analyzed and aligned to the respective reference alleles in the human genome. Clones whose alleles harbored only indel mutations for hEMC1, hEMC2, hEMC3, and hEMC5 (full knockouts) respectively were further validated on the protein level.

Dual fluorescent EMC client reporter cell lines

Dual client reporters for TMEM97, ADRB1 (protein name: B1AR), and FDFT1 (protein name: SQS) were introduced lentivirally into each of the EMC1, EMC2, EMC3, and EMC5 knockout cell lines. TMEM97 and ADRB1 full-length sequences were used with a C-terminal tag -mCherry-P2A-GFP. The sequence for FDFT1 transmembrane domain (SQS³⁷⁸⁻⁴¹⁰) was tagged N-terminally with GFP-P2A-mCherry- and an opsin tag on the C-terminus as used in a prior study ([Guna et al., 2018](#)). Three days post-transduction, GFP/mCherry-positive cells were sorted on BDARIALL. Sequences for these constructs are available in the [Supplementary file 5](#).



Scheme 1. Client reporters.

Mutant EMC cell lines

The EMC mutant genes were synthesized and cloned by Twist into pKDP119-SFFV-[insert site]-IRES-Puro-P2A-BFP. For hEMC subunit mutation details refer to the Key Resources Table, for sequences refer to [Supplementary file 5](#). Mutant hEMC cell lines were generated by lentiviral introduction of the respective hEMC mutant subunit into the respective knockout cell lines (hEMC1, hEMC2, hEMC3, or hEMC5) containing the dual fluorescent reporters for each EMC client (pKDP110_ADRB1_mCherry_P2A_GFP, pKDP111_TM97_mCherry_P2A_GFP, or GFP_P2A_mCherry_FDFT1_TMD_opsintag). The expression of each fluorescent reporter was read out 6 days after puromycin selection in each of the hEMC mutant cell lines.



Scheme 2. hEMC subunit mutation construct design.

Flow analysis

For each hEMC mutant cell line, 20,000 live cells were recorded on Attune NxT flow cytometer. FlowCal flow analysis package was used for analysis in Python. First, live cells were gated based on FSC/SSC. Then GFP (BL1-A) and mCherry (YL2-A) were plotted for each mutant and control cell line. mCherry:GFP intensity ratios were calculated for individual cells in each cell line. Fluorescence ratios for each substrate in an hEMC mutant cell line were normalized to the mCherry:GFP ratio of the same substrate in the hEMC wild-type rescue cell line. Distributions of fluorescence ratios were plotted as histograms in Python using seaborn.

Fluorescent reporter statistical analysis

We performed bootstrap estimates of the mean of normalized mCherry/GFP ratio from the FACS data. For bootstrapping, we performed 1000 iterations with 50 cells/iteration to fit normal distributions. We performed two separate one-sided T-tests at a p-value cutoff of 0.01 between each mutant and the respective subunit WT to test for significant decreases or increases in ratios based on bootstrapped estimates of the mean. These statistics are contained in the files 'filtered_final_pvalues.01cutoff.lo.csv' and 'filtered_final_pvalues.01cutoff.hi.csv' respectively. Statistics were generated for the EMC-independent membrane protein controls ('stats.membrane.controls.lo', 'stats.membrane.controls.hi') and for the mCherry-p2a-GFP control ('.mcherry.p2a.gfp.control.lo', 'stats.mcherry.p2a.gfp.control.hi'). Values can be found in **Supplementary file 2**.

Western blotting

Cell pellets were lysed using lysis buffer (20 mM Tris pH 7.5, 150 mM NaCl, 5 MgCl₂, 1% Triton x-100, 1 mM DTT, 24 U/ml Turbo DNase (Ambion). Clarified lysate was quantified and samples were boiled with 4x LDS sample (Thermo Fisher, NP0007) buffer for 5 min at 95°C. Samples were separated on 4–12% or 12% Bolt Bis-Tris Plus Gels (Invitrogen, NP0322PK2). Proteins were transferred onto nitrocellulose membranes using Bio-Rad Trans-Blot Turbo transfer system. Membranes were blocked in Odyssey Blocking Buffer (LI-COR, 927–50000) for an hour at room temperature. Blocked membranes were incubated with primary antibody diluted in TBST and incubated overnight at 4°C on a shaker. Primary antibodies were detected by incubating membranes with 1:10,000 dilution of IRDye-conjugated (LI-COR) secondary anti-mouse and anti-rabbit antibodies for 1 hr at room temperature. Blots were visualized using LI-COR imaging system. The primary antibodies used in this study are listed in the Key Resources table.

Yeast strains

Strain BY4741 and BY4742 were used as the wild-type parental strains for the creation of the yEMC overexpression strain. Yeast homologous recombination (**Rothstein, 1991**) was used to generate yeast strains. For the overexpression strain, the endogenous promoter for each yEMC subunit (yEMC1, yEMC2, yEMC3, yEMC4, yEMC5, yEMC6, yEMC7, yEMC10) were replaced with a TEF2 promoter. In addition, EMC5 was tagged at the C-terminus with linker-TEV-linker-3xFlag. Auxotrophic markers and drug selection markers in both BY4741 and BY4742 were employed to add this promoter modification to all these eight subunits and the two strains were crossed to create the resulting BY4743 strain used for immunoprecipitation. Endogenous EMC yeast strain was made using W303a wild-type parental background (leu2-3,-112; his3-11,-15; trp1-1; ura3-1; ade2-1; can1-100; MATa). Homologous recombination was used to integrate a linker-TEV-linker-3xFlag at the C-terminus of yEMC coding sequence. Genomic PCR was conducted to verify integration.

Design and purification of fragments antigen binding (Fab) DH4 and DE4

Fabs were identified as described in these studies (**Kim et al., 2011; Wu et al., 2012**). Overexpressed yEMC solubilized in DDM as described above was biotinylated and streptavidin magnetic beads were used to capture yEMC, which was then subjected to a Fab phage library. Unbound Fabs were washed away and then binding Fabs were eluted and analyzed by ELISA. Two Fabs were identified binding yEMC, Fab DH4 and DE4.

Purification of DH4 and DE4 Fabs

Plasmid with either Fab DH4 or DE4 were transformed into BL21 Gold Star cells and plated onto agarose plates with 2x YT + 2% glucose + Ampicillin. Cultures were inoculated from resulting colonies for overnight growth at 30°C into 2xYT + 2% glucose + Amp. In the morning dilute overnight culture to OD₆₀₀ of 0.05 in 1L, in a 2.8 L flask of 2xYT + 0.1% glucose + Amp. Grow the culture at 180 rpm at 37°C shaker until OD₆₀₀ of 0.6, then, switch to shaking at 19°C for 1 hr. Next, induce with 0.4 mM IPTG. Shake at 180 rpm at 19°C for 18–20 hr. Spin 1L cultures down at 3500 rpm in large Beckman Centrifuge at 4°C for 20 min in (8.1 rotor). Discard media and gently resuspend cell pellet in ice-cold 20 ml in Buffer 1 (0.2 M Tris pH 8.0, 0.5 mM EDTA, 0.5 M Sucrose) on ice. Transfer the resuspended cells from step 2 into two smaller JLA 25.5 centrifuge tubes. Add 20 mL of ice cold

ddH₂O with 2x protease inhibitor cocktail (Roche Complete Ultra, Millipore Sigma 5056489001) from step 3 to the resuspended pellets. Incubate at on ice for 1 hr occasionally swirling samples gently. Spin periplasmic fractions at 13,000 x g for 15 min, 4°C, rotor 25.50. Wash 500 µL Ni resin (Qiagen, Ni-NTA, 30210) per periplasmic fraction four times in Buffer 2 (50 mM Tris pH 8.0, 250 mM NaCl). Add MgCl₂ and imidazole to a final concentration of 10 mM to each periplasmic fraction. Add beads to periplasmic fractions and nutate at 4°C for 2 hr. Spin down beads at 2000 x g, 10 min, 4°C. Transfer beads either to a 50-mL gravity column. Wash the beads with 20 column volumes of Buffer 3 (50 mM Tris pH 8.0, 500 mM NaCl, 20 mM Imidazole). Elute protein with three column volumes of Buffer 4 (50 mM Tris pH 8.0, 500 mM NaCl, 300 mM Imidazole). Analyze eluate by SDS-PAGE 4–12% Invitrogen (Invitrogen, NP0321PK2). Fabs as two bands run around 30 kDa in reducing conditions, or 50 kDa in non-reducing conditions. Dialyze eluate O/N in Dialysis cassette 10 kD molecular weight cutoff at 4°C against 150 mM KOAc, 20 mM HEPES pH 6.8.

Purification of overexpressed yeast EMC5-3xflag

The OE-Emc5-3xflag yeast strain were grown in YEPD media in a 40 L fermenter, harvested and flash frozen in liquid nitrogen. Cell pellets were thawed and diluted in lysis buffer (50 mM HEPES pH 6.8, 150 mM KOAc, 2 mM MgOAc, 1 mM CaCl₂, 0.2M Sorbital, 2x Protease Inhibitor). Bead beating (10 times → 1 min on, 2 min off) was used to lyse cells. For 25 g of cells, 0.1 mm cold beads were added and lysis buffer up to the top of the 50 mL canister. After lysis, beads were filtered and solution centrifuged at 10,000 xg for 10 min. Supernatants were ultracentrifuged at 42,000 RPM (Ti 45 rotor) for 2 hr. Supernatant was discarded. Membrane pellet was combined with the lipid layer, and resuspended in lysis buffer and then a precooled dounce homogenizer was used to dounce 20 times. Membranes were aliquoted and flash frozen in liquid nitrogen. On ice, 150 mL of solubilization buffer (50 mM HEPES pH 6.8, 150 mM KOAc, 2 mM MgOAc, 1 mM CaCl₂, 15% glycerol, 1% b-DDM, 2x Protease Inhibitor) was added incrementally to 7.5 g of thawing membranes, nutated at 4°C for 1 hr in JA 25.5 rotor tubes, and centrifuged at 20,000 rpm for 45 min. Meanwhile 2.5 mL of αFLAG agarose beads (Millipore A2220) were rinsed in 50 mL of low-salt buffer (50 mM HEPES pH 6.8, 150 mM KOAc). Supernatant was added to αFLAG beads and nutated at 4°C for 2 hr. Resulting solution was applied over a glass column. After flowing through unbound solution, αFLAG beads were washed with 100 mL low-salt buffer, 100 mL high-salt buffer (50 mM HEPES pH 6.8, 300 mM KOAc, 0.05% b-DDM), and 100 mL low-salt buffer. αFLAG beads were resuspended in 10 mL of low-salt buffer and 300 µL of TEV (1.15 mg/mL) was added and nutated overnight at 4°C. Removed supernatant from beads by low-speed spin and applied over 500 µL of NiNTA beads equilibrated with low-salt buffer to remove excess TEV. Flow through glass column and collect supernatant. Using a 100 kD concentrator (Millipore, UFC910008) solution was concentrated to 2 mg/mL. Concentrated EMC protein was applied to the Akta Explorer Superose 6 Increase column (Cytiva, 29091596) for size exclusion chromatography in the size exclusion buffer (20 mM HEPES pH 6.8, 150 mM KOAc, 0.05% b-DDM). Fractions were evaluated by SDS-PAGE Coomassie stain and negative stain electron microscopy then EMC peak fractions were pooled and incubated with 2x molar excess of Fab, either Fab DH4 or Fab DE4, for 30 min on ice. Solution was applied to Akta Explorer Superose 6 Increase for size exclusion of Fab bound EMC. Resulting EMC-Fab fractions were evaluated by SDS-PAGE Coomassie stain and EMC-Fab peak fractions were pooled.

Purification and nanodisc reconstitution of endogenous yeast EMC5-3xflag

Yeast was grown in rich media (YPAD) in a 65L fermenter until OD 2.6. Cell pellets were harvested and flash frozen in liquid nitrogen. Pellets were ground using three cycles in a French press. As above, the resulting solution was ultracentrifuged to separate membranes, dounced to homogenize, and flash frozen in liquid nitrogen. Thawed membranes were solubilized in 1% b-DDM (Anatrace, D310) nutating at 4°C for 1 hr then centrifuged to separate solubilized membranes from the pellet. Supernatant was applied to equilibrated αFLAG beads, nutated at 4°C for 1 hr, and applied over a disposable plastic column at 4°C. αFLAG beads were washed with low-salt buffer and high salt buffer. Then washed with low-salt buffer with b-DDM+CHS (Anatrace, CH210) (10:1) in place of b-DDM. αFLAG beads were then transferred to a 15-mL Eppendorf tube for TEC cleavage and nanodisc reconstitution.

Bio-Beads SM-2 (Bio-Rad) were prepared ~400 μL biobeads, rinsing with EtOH, and then water four times. Yeast Extract Total (Avanti Polar Lipids, 190000 C-100mg) was prepared by transferring chloroform resuspended solution to a glass vial, drying the lipids into a film with nitrogen gas, drying in a vacuum desiccator overnight, and then solubilizing the lipids first in water and then in size exclusion buffer with DDM+CHS by bath sonication, aliquots stored at -20°C until use. A total of 200 μL of TEV protease (5 mg/mL) and 150 μL of 1 mg/mL Yeast Total Extract solubilized in b-DDM+CHS, at room temperature for 30 min. Then added MSP1D1, purified as described previously (Ritchie et al., 2009), to a ratio of 200:10:1 (Yeast total extract:MSP1D1:EMC), at 4°C for 10 min. Then activated Bio-Beads SM-2 (Bio-Rad), ~300 μL , were added and nutated overnight. On-bead reconstitution employed adapted from Laverty et al., 2019. In the morning, ~100 μL more Bio-Beads SM-2 (Bio-Rad) were added and 2x molar excess of FabDH4, nutated for another hour. Beads and solution applied to an EconoPac column (Bio-Rad). Flow through was collected and solution was applied to a 100 kD (Amicon) concentrator. Resulting concentrated EMC was applied to the Akta Explorer Superose 6 Increase column for size exclusion chromatography. Peak fractions were pooled for SDS-PAGE Coomassie stain, negative stain, and cryo-EM evaluation. Key reagents used are provided in the Key Resource Table.

Cryo-EM sample preparation and data collection for yEMC

Overexpressed EMC + Fab DE4 in b-DDM

Following size exclusion sample was prepared for cryo-electron microscopy. A total of 3 μL of sample (0.1 mg/mL EMC + Fab DE4 in 20 mM HEPES pH 6.8, 150 mM KOAc, 0.05% b-DDM) was applied to the grid, incubated for 10 s, then blotted with no offset for 6.5 s and plunge frozen in liquid ethane using a Vitrobot Mark III at 5°C , Whatman #1 filter paper, and 100% humidity. Protein was frozen on glow discharged Ultrathin Carbon Film on a Lacey Carbon Support Film (Ted Pella, 01824) and stored under liquid nitrogen until imaging. This dataset was collected on the 300 kV Technai Polara at UCSF with a 30 μm C2 aperture, 100 μm Objective aperture, and K2 Summit detector operated in super-resolution mode. 1536 micrographs were collected using SerialEM (Mastronarde, 2005) at a magnification of 31,000X (0.6078 \AA /super resolution pixel) as dose-fractionated stacks of 40 frames x 0.2 s exposures (1.42 $\text{e}^{-}/\text{\AA}^2$) for a total dose of ~56.85 $\text{e}^{-}/\text{\AA}^2$ (Table 1).

Overexpressed EMC + Fab DH4 in b-DDM

Following size exclusion sample was prepared for cryo electron microscopy. A total of 3 μL of sample (0.1 mg/mL EMC + Fab DH4 in 20 mM HEPES pH 6.8, 150 mM KOAc, 0.05% b-DDM) was applied to the grid, incubated for 10 s, then blotted with no offset for 7 s and plunge frozen in liquid ethane using a Vitrobot Mark III at 4°C , Whatman #1 filter paper, and 100% humidity. Protein was frozen on glow discharged Ultrathin Carbon Film on a Lacey Carbon Support Film (Ted Pella 01824). This dataset was collected at the HHMI Janelia Research Campus on Titan Krios 2, a 300 kV microscope equipped with a 50 μm C2 aperture, 70 μm objective aperture, and K2 Summit detector operated in super-resolution mode. A total of 3357 micrographs were collected using automated SerialEM (Mastronarde, 2005) collection with defocus range set between -1 and -3 μm at a magnification of 22,500X (0.655 \AA /super resolution pixel) as dose-fractionated stacks of 50 frames x 0.2 s exposures (1.165 $\text{e}^{-}/\text{\AA}^2$) for a total dose of ~58.3 $\text{e}^{-}/\text{\AA}^2$ (see Table 1).

Endogenous EMC + Fab DH4 in MSP1D1-yeast total extract nanodisc

Following size exclusion sample was prepared for cryo electron microscopy. Four μL of sample (~0.8 mg/mL EMC + Fab DH4 in nanodisc in 20 mM HEPES pH 6.8, 150 mM KOAc, 0.05% b-DDM) was applied to the grid from the left side, then blotted with no offset for 2.5 s, then another 4 μL of sample was applied to the right side of the grid (without glow discharge) and blotted for 3.5 s, and plunge frozen in liquid ethane using a Vitrobot Mark IV at 4°C , Whatman #1 filter paper, and 100% humidity. Protein was frozen on R 1.2/1.3 grids with 300 Au mesh (Quantifoil, Germany). This dataset was collected at UCSF on the Titan Krios 2, a 300 kV microscope equipped with a 70 μm C2 aperture, 100 μm objective aperture, and K3 detector operated in CDS mode. 5949 micrographs were collected using automated SerialEM (Mastronarde, 2005) collection with defocus range set between -0.8 and -2 μm at a magnification of 105X (0.4265 \AA /super resolution pixel) as dose-

fractionated stacks of 100 frames x 0.06 s exposures ($0.67 \text{ e}^-/\text{\AA}^2$) for a total dose of $\sim 67 \text{ e}^-/\text{\AA}^2$ (see [Table 1](#)).

Image analysis and 3D reconstruction for yEMC

Overexpressed EMC + Fab in b-DDM

Image processing schematic ([Figure 2—figure supplement 1](#)) and [Table 1](#) have additional details. All dose-fractionated image stacks were corrected for motion artefacts, 2x binned in the Fourier domain, and dose-weighted using MotionCor ([Li et al., 2013](#)) for the DDM datasets, resulting in one dose-weighted and one unweighted integrated image per stack with pixel sizes of 1.22 Å (DDM - Polara) or 1.31 Å (DDM - Janelia Krios). The parameters of the Contrast Transfer Function (CTF) were estimated using GCTF-v1.06 ([Zhang, 2016](#)) and the motion-corrected but unweighted images. For each dataset, ~ 1000 particles per dataset were manually selected and averaged in 2D using RELION 2.0 ([Kimanius et al., 2016](#)). The resulting class sums were then used as templates for automated particle picking using Gautomatch-v0.55 ([Zhang, 2016](#)), followed by extraction in RELION 2.0. Five rounds of 2D classification were performed to eliminate ice contamination, particles near carbon edges, and 2D class without visible secondary structure features. Subsequent particles were subjected to 3D auto-refine in Relion 2.0. The Polara dataset was processed providing a reference model created in Spider ([Shaikh et al., 2008](#)) roughly mimicking the dimensions seen in 2D projections, then a second round was run using the resulting volume before two rounds of 3D classification without alignments. The resulting subset of particles were subjected to 3D auto-refine and then 3D classification with local alignments. The best 83,599 particles were then subjected to 3D refinement resulting in a 3D volume with $\sim 8 \text{ \AA}$ reported resolution, which was rescaled and low-pass filtered for use as the reference for the DDM Krios dataset. 3D classification without alignments, 3D refinement, 3D classification with local alignments, and 3D auto refinement were performed resulting in a $\sim 7 \text{ \AA}$ structure composed of 170,186 particles. Both resulting reconstructions overlay with one another, despite having Fab DH4 in one sample and DE4 in the other. Furthermore, they both displayed a severe orientation bias, and 3D reconstructions appeared streaky.

Particles from both datasets were re-extracted and scaled to a common pixel size of 1.35 Å and box size of 266. The combined dataset was subjected to two rounds of 3D refinement to form a consensus structure at $\sim 6.8 \text{ \AA}$ all conducted in Relion 2.0. These particles were then subjected to 3D refinement in THUNDER ([Hu et al., 2018](#)) using soft-edged mask. THUNDER produced a resulting 3D reconstruction that visually appeared less distorted along the axis of overrepresented views and resulted in a $\sim 4.8 \text{ \AA}$ consensus structure. Postprocessing was done in Relion 3.0 resulting in a $\sim 4.3 \text{ \AA}$ sharpened map and output was used to generate the FSC plot ([Figure 2—figure supplement 1](#)). Molecular graphics and analyses were performed with the UCSF Chimera package ([Pettersen et al., 2004](#)) and Coot 0.8.7 and Coot 0.9 ([Emsley and Cowtan, 2004](#); [Emsley et al., 2010](#)). Local resolution was computed by inputting mask and half maps into Cryosparc two local resolution ([Stagg et al., 2014](#); [Punjani et al., 2017](#); [Punjani et al., 2019](#)) and visualizing the resulting map and scaling in UCSF Chimera.

Endogenous EMC + Fab DH4 in MSP1D1-yeast total extract nanodisc

All dose-fractionated image stacks were corrected for motion artefacts, 2x binned in the Fourier domain, and dose-weighted using MotionCor2 ([Zheng et al., 2017](#)) using Focus ([Biyani et al., 2017](#)) resulting in a 2x binned pixel size of 0.835 Å (nanodisc - UCSF Krios). The parameters of the Contrast Transfer Function (CTF) were estimated using GCTF-v1.06 ([Zhang, 2016](#)) and the motion-corrected but unweighted images. Data were then split into five groups of 1000 micrographs for processing until they were combined in 3D. Roughly ~ 1000 particles per subset were manually selected and averaged in 2D using RELION 3.0 ([Zivanov et al., 2018](#)) for the nanodisc dataset. The resulting class sums were then used as templates for automated particle picking using Autopick in Relion 3.0, followed by extraction and one round of 2D classification per subset to remove ice contamination. The resulting subsets of particles were subject to 3D refinement. Combining the RELION star files these particles were imported into Cryosparc 2.0 ([Punjani et al., 2017](#); [Punjani et al., 2019](#)) along with a reference model. These data were subjected to non-uniform homogeneous refinement, a round of four class 3D heterogeneous refinement, another round of non-uniform refinement for the best class (roughly 1.2 million particles), non-uniform homogeneous refinement, a round of

two class 3D heterogeneous refinement, and another non-uniform homogeneous refinement for the best class (roughly 500,000 particles). These were then exported to RELION 3.0 using PyEM (Asarnow *et al.*, 2019). 3D Classification was performed with local alignments, then CTF refinement of the best class (230,528 particles) resulting in a ~ 3.2 Å final reconstruction. This was post-processed in both RELION 3.0 and using phenix.autosharpen, both resulting maps were used for model building.

Model building and refinement of yEMC in nanodiscs

Structural biology applications used in this project were compiled and configured by SBGrid (Morin *et al.*, 2013). The yeast EMC structure was built de novo using Coot (version 0.8.7 and 0.9) and UCSF ChimeraX (Goddard *et al.*, 2018). Visible secondary structure was built by hand for the entire structure using overlays of the yEMC detergent consensus map as well as the yEMC nanodisc unsharpened and sharpened map. Starting with the best resolved transmembrane helices, sequence was placed for each of the predicted transmembrane helices, using TMHMM (Krogh *et al.*, 2001), in the yEMC proteins. Visual inspection for landmark residues (tryptophan, tyrosine, leucine, and proline) in the sequences that correlated with the position of well densities as well as fit correlation in UCSF Chimera was computed to assign identities for yEMC1, yEMC3, yEMC5, and yEMC6. Connectivity between the EMC1 assigned helix to the luminal domain was used to start assigning sequence for the luminal portion of EMC1. Secondary structure prediction was computed for all yEMC proteins using Phyre2 (Kelley *et al.*, 2015) and Quick2D, a tool within the Max-Planck Institute for Developmental Biology Bioinformatics Toolkit that visualizes several different secondary structure predictors (Jones, 1999; Cuff and Barton, 2000; Ouali and King, 2000; Rost, 2001; Lupas *et al.*, 1991; Jones *et al.*, 1994; Ward *et al.*, 2004; Peng *et al.*, 2006; Obradovic *et al.*, 2005). Secondary structure prediction was used to check and guide sequence assignment of beta strands and helices. Next several homology models were computed and overlain for yEMC2, with a predicted TPR structural domain, using Robetta (Raman *et al.*, 2009; Song *et al.*, 2013), I-TASSER (Zhang, 2008; Roy *et al.*, 2010; Yang *et al.*, 2015), Phyre2 (Kelley *et al.*, 2015), and RaptorX (Källberg *et al.*, 2012). These were used in addition to secondary structure prediction to guide sequence assignment, loop building, and helical packing. Fab DH4 starting structure was computed using Phyre2 1-to-1 threading against a crystal structure of a monoclonal Fab (PDB 1M71, Vyas *et al.*, 2002). EMC3, EMC5, and EMC6 were built off of the transmembrane helices using sphere refinement, real space refinement, regularization, and visual monitoring of the Ramachandran plot in Coot. EMC7 and EMC10 both form beta sandwich folds on the exterior of the EMC1 luminal domain, beta strand sequence was placed for both in both densities, position of aromatic residues and loop length differed between the two allowing assignment of each. After building EMC1-3, EMC5-7, and EMC10, there remained several transmembrane helices and a beta strand fitted into the lumen but not connected to EMC1, EMC7, or EMC10. The resolution of the luminal domain is better than 3 Å in most parts allowing for sequence placement of the EMC4 C-terminus and C-terminal transmembrane helix. The connectivity of the transmembrane helix to the cytoplasmic domain was not resolved. However, there was an additional poorly resolved short helix and loop density in the cytoplasmic domain which was assigned to EMC4.

Two poorly resolved transmembrane helices remained, however, due to the fact they did not have clear connectivity to any built strand, poly alanine alpha helices were built in but not assigned to a yEMC protein (Figure 5—figure supplement 5). EMC4 had density in the cytoplasmic domain as well as the luminal domain, suggesting that it has either one or three transmembrane passes. EMC7 and EMC10 were predicted to have transmembrane helices, however, the connection between the luminal densities and those predicted transmembrane helices was not clear. Additional density that was not built into was visualized in UCSF ChimeraX (Goddard *et al.*, 2018) and allowed for subsequent assignment of several glycosylated residues and one POPC molecule. Each subunit was built in a separate pdb file and subjected to iterative rounds of phenix.real_space_refine (Adams *et al.*, 2011; Liebschner *et al.*, 2019) into segmented maps preceded and followed by adjustment in Coot. Manual assignment of secondary structure restraints was used and improved during Phenix refinement. Once all of the well-resolved secondary structure was assigned to yEMC subunits, PDBs were combined and subjected to iterative rounds of phenix.real_space_refine (Adams *et al.*, 2011; Afonine *et al.*, 2018; Liebschner *et al.*, 2019) in the unsharpened and then sharpened maps. Loops were built back where the connectivity was clear and then refined again in

Phenix and Coot. PDBs were prepared for refinement steps using phenix.reduce to add hydrogens throughout refinement steps, ReadySet to generate cif restraints, and Phenix PDB preparation tool for creating mmCIF files for deposition. Representative regions of the model as well as the map-to-model FSC can be found in **Figure 2—figure supplement 5**. Model for the yEMC nanodisc sample was used to generate reference model restraints for phenix real space refinement of yEMC DDM model.

Cloning and expression constructs for hEMC

A modified version of the biGBac (Weissmann *et al.*, 2016) multi-gene cloning method was combined with the BacMam (Goehring *et al.*, 2014) mammalian expression system to allow for recombinant production of human EMC (hEMC). hEMC subunits were individually inserted into pEG, with EMC5 bearing a C-terminal Flag-tag. To amplify gene-expression cassettes (GEC) from pEG, original forward primers from biGBac were used in combination with modified reverse primers bearing complementarity downstream of the SV40 terminator sequence. GECs were inserted into pBIG1a-e vectors as follows: pBIG1a (EMC1 - Uniprot code Q8N766-1), pBIG1b (EMC4 - Q5J8M3-1; EMC5-Flag - Q8N4V1-1, which encodes DYKDDDDK immediately after R131; EMC6 - Q9BV81), pBIG1c (EMC2 - Q15006; EMC3 - Q9P0I2-1; EMC7 - Q9NPA0), pBIG1d (EMC8 - O43402-1; EMC9 - Q9Y3B6), pBIG1e (EMC10 - Q5UCC4-1). These were subsequently combined into pBIG2abcde to yield a single expression vector containing all 10 hEMC subunits. Bacmid was generated in DH10 EMBacY *E. coli* and subsequently transfected into Sf9 insect cells using FuGENE (Promega) reagent. Virus was amplified in Sf9 cells up to P3 and virus supernatant sterilized by filtration.

hEMC expression, purification, and nanodisc reconstitution

Recombinant hEMC was expressed by baculovirus transduction of human embryonic kidney (HEK) 293S GnTI- cells grown in suspension. Cells were maintained at 37°C in Freestyle 293 Expression Medium (Thermo) and expanded with home-made suspension medium (Chaudhary *et al.*, 2012) in 2 L shaker flasks. For expression of hEMC, 10% (v/v) P3 virus was added to 800 mL of HEK culture at a cell density $>3 \times 10^6$. 16 hr post-transduction, 10 mM butyrate was added and the temperature reduced to 30°C. Cells were harvested 48 hr later and stored frozen at -80°C.

For purification, 15–20 g of cell pellet was thawed and resuspended in 60–80 mL Lysis Buffer containing 50 mM ammonium citrate pH 6.0, 150 mM sodium chloride, 0.001 mg/mL Benzonase, EDTA-free protease inhibitor cocktail (1 tablet per 50 mL of buffer), and lysed by Dounce homogenization on ice (50 strokes). Glyco-diosgenin (GDN, Anatrace) was added to the lysate at 2% (w/v) and cellular membranes solubilized for 3 hr at 4°C under constant stirring. Insolubilized material was removed by centrifugation at 100,000 x g, supernatant incubated with 2 mL M2 Flag-affinity resin in-batch for 2 hr at 4°C. The resin was poured into a column and unbound proteins washed away with 25 column volumes (CV) of Wash Buffer containing 20 mM ammonium citrate pH 6.0, 150 mM sodium chloride, 0.01% (w/v) GDN. Bound hEMC was eluted in 10 CV Wash Buffer containing 0.3 mg/mL Flag peptide and concentrated to <500 µL using centrifugal concentration filters with 100 kDa cut-off (Amicon). Sample was polished using size-exclusion chromatography (SEC) on a Superose 6 Increase 10/300 GL column (GE Healthcare) with Running Buffer containing 10 mM ammonium citrate pH 6.0, 100 mM sodium chloride, 0.25 mM TCEP, 0.01% (w/v) GDN. Peak fractions containing hEMC were pooled, concentrated to ~3 mg/mL and used immediately for cryo-EM grid preparation. hEMC in nanodiscs composed of MSP1D1 scaffold protein and 1-palmitoyl-2-oleoyl-sn-glycero-3-phosphatidylcholine (POPC) was reconstituted following Flag-affinity chromatography. The MSP1D1 expression vector was a gift from Franz Hagn (TUM, Germany) and the scaffold protein purified from *E. coli* following a published protocol (Hagn *et al.*, 2018). Prior to reconstitution, hEMC purified by Flag-affinity chromatography was mixed with MSP1D1 and POPC (solubilized as 25 mM stock in 5% n-dodecyl β-D-maltoside) in a 1:4:50 ratio and this mixture incubated on ice for 2 hr. Nanodisc reconstitution was achieved by incubation with 0.5–1 mL Bio-Beads SM-2 (Bio-Rad) for 16 hr at 4°C under constant rotation. The liquid phase was aspirated, concentrated to <500 µL and injected onto a Superose 6 s column with buffer containing 10 mM ammonium citrate pH 6.0, 100 mM sodium chloride, 0.25 mM TCEP, to separate nanodisc-embedded hEMC from empty nanodiscs. Peak fractions were pooled and concentrated to ~2 mg/mL for immediate cryo-EM grid preparation.

Cryo-EM sample preparation and imaging for hEMC

Four μL of freshly purified hEMC (in detergent or nanodisc) was applied to glow discharged copper Quantifoil holey carbon grids (R1.2/1.3 300 mesh) at 100% humidity and 4°C in a Vitrobot Mark IV (Thermo) and incubated for 30 s. Excess liquid was blotted away with filter paper (blot force 4–6, blot time 4 s) and the grid plunge-frozen into liquid ethane. Samples were imaged on a FEI Titan Krios microscope operating at 300 kV, equipped with a post-column GIF and a K3 direct detector operating in counting mode. Images were recorded at a nominal magnification of 105,000x (0.8512 Å/pixel at the specimen level) for hEMC in nanodiscs or 81,000x (1.094 Å/pixel at the specimen level) for hEMC in detergent, with target defocus ranging between 0.7 and 2.8 μm and total exposure of $\sim 70 \text{ e}/\text{\AA}^2$ using SerialEM (*Mastronarde, 2005*). On-the-fly motion correction, CTF estimation and templated particle auto-picking were performed using a pipeline implemented in Focus (*Biyani et al., 2017*).

Cryo-EM data processing for hEMC in detergent

Preprocessing in Focus included dose-weighted motion correction using Motioncor2 (*Zheng et al., 2017*), CTF estimation using Gctf (*Zhang, 2016*) and templated autopicking using Gautomatch (*Zhang, 2016*). The autopicking template originated from a reconstruction of hEMC in GDN micelles, with data acquired on a K2 (Gatan) direct electron detector (operated in counting mode) under liquid nitrogen conditions using a Glacios microscope (Thermo) operated at 200 kV. 3713 micrographs with a maximal resolution estimate better than 5 Å were imported into Relion 3.0 (*Zivanov et al., 2018*), from which ~ 3.35 million particles were extracted applying fourfold binning. These were subjected to three rounds of 2D classification and two rounds of 3D classification (using the reconstruction obtained from the 200kV dataset as reference), followed by 3D autorefinement. This reconstruction was used as initial model for three rounds of 3D classification of the original ~ 3.35 million particles (first round: K = 10, T = 10; second round: K = 10, T = 10; third round: K = 3, T = 16), yielding a set of 144,222 particles. This set was re-extracted at full pixel size, followed by masked 3D autorefinement, producing a reconstruction at 3.77 Å overall resolution. Application of non-uniform refinement in cryoSPARC (*Punjani et al., 2017; Punjani et al., 2019*) further improved the map quality and overall resolution to 3.60 Å.

Cryo-EM data processing for hEMC in nanodiscs

Micrographs were preprocessed using Focus in a similar manner as for hEMC in detergent. 9164 micrographs with a maximal resolution estimate better than 5 Å were imported into Relion 3.0, from which ~ 5.9 million particles were extracted applying fourfold binning. These were subjected to three rounds of 3D classification (using hEMC in GDN as reference for the first round), after which 386739 particles were kept and re-extracted to full pixel size. Particles were aligned using global angular search 3D classification (K = 1, T = 4) before one further round of 3D classification with a soft mask and skipping alignment (K = 6, T = 8), to isolate a set of 177560 homogeneous hEMC particles. Masked 3D autorefinement of this particle set yielded a map at 3.6 Å overall resolution. Implementation of cryoSPARC non-uniform refinement led to a consensus map at 3.4 Å global resolution. To aid de novo model building of cytoplasmic and luminal domains, these parts were subjected to masked focused classification (K = 5, T = 8), 3D autorefinement and post-processing in Relion, yielding improved maps at 3.4 Å and 3.2 Å, respectively. To obtain highest quality maps of the transmembrane domains, the 177560 particles from consensus refinement were processed using Sidesplitter (*Ramlaul et al., 2020*), producing a 3.3 Å global map after Relion post-processing, where transmembrane helix pitch and side chains were well resolved and allowed for unambiguous sequence assignment. The final particle set was further subjected to 3D variability analysis (*Punjani and Fleet, 2020*) in cryoSPARC, revealing the presence or absence of the EMC7 luminal domain between the EMC1 beta-propellers. Heterogeneous refinement, using a map from 3D variability analysis containing stronger EMC7 density as reference, allowed for further sub-classification of the consensus particle set. Non-uniform refinement of the class containing stronger EMC7 density produced a map at 3.5 Å global resolution, which was subsequently used to build an EMC7 model.

Model building and refinement of hEMC in nanodiscs and detergent

Given the higher quality hEMC nanodisc map compared to the detergent map, the former was used for de novo model building in Coot (*Emsley and Cowtan, 2004; Emsley et al., 2010*). Focused luminal and cytoplasmic, as well as Sidesplitter maps, permitted assignment of amino acid sequence throughout all parts of hEMC. Inspection of structural homology and secondary structure predictions for the hEMC subunits produced via HHpred and Quick2D servers (*Zimmermann et al., 2018*) predicted the luminal domain of EMC1, the largest hEMC subunit, to consist of two beta-propellers. EMC7 and EMC10 are predicted to feature beta-sandwich structures in the lumen. A final missing beta-strand of the EMC1 membrane proximal propeller could be assigned to the luminal C-terminus of EMC4, which forms a parallel sheet with EMC1 residues 668–674. Almost all EMC2 is predicted to form an alpha-solenoid structure harboring several TPR motifs. Analysis of EMC8 and EMC9 amino acid sequences revealed structural homology to CSN5 (deneddylase subunit of the CSN complex) and Rpn11 (deubiquitinase subunit of the 19S proteasomal regulatory particle) peptide hydrolase folds. The globular density sitting on the distal face of the EMC2 solenoid, facing away from the rest of the complex, was modeled with the EMC8 sequence, which shares ~45% amino acid sequence identity with EMC9. Additional helical density sitting sideways on top of the EMC2 solenoid could be modeled as two cytoplasmic helices of EMC3 as well as the extended, partially helical meander of the EMC3 C-terminus. Beta-strand-like density on the EMC8 surface, commonly occupied by deubiquitinase substrate peptides, was assigned to the extreme N-terminus of EMC4, with a further downstream part of this cytoplasmic domain snaking along EMC2 and EMC3 toward the transmembrane part of hEMC.

Clear side-chain resolution and excellent connectivity of the Sidesplitter map, within the nanodisc encircled membrane domain, allowed us to model all predicted transmembrane helices of EMC1, EMC3, EMC5, and EMC6. EMC5 extends its C-terminus outside the membrane, which snakes through the central cavity of the EMC2 solenoid on the cytoplasmic side. Inspection of the map at lower thresholds revealed density for at least two additional transmembrane helices facing EMC3 and EMC6 on one side of the complex: continuous density from one of these helices toward the luminal EMC4 C-terminus indicates that at least one of these gate helices represent EMC4's C-terminal transmembrane helix. However, given poor map resolution and connectivity in this region, we left the other gate helices unassigned.

Model refinement was performed using real-space refinement in Phenix (*Adams et al., 2011*), applying secondary structure and Ramachandran restraints. Initially, luminal and cytoplasmic domains were refined individually against their focused maps, after which the improved models were rigid-body placed and refined against the non-uniform refined consensus map. The transmembrane domain was likewise first refined against the Sidesplitter map, after which all parts of hEMC were combined into a consensus model and refined against the consensus map.

The refined hEMC nanodisc model was subsequently docked into the hEMC detergent map, revealing a relative rotation of the entire luminal domain. The fitted model was manually adjusted in Coot (*Emsley and Cowtan, 2004; Emsley et al., 2010*) and refined using Phenix real-space refinement (*Adams et al., 2011*). Different masking strategies failed to produce stronger density for the EMC7 luminal domain in the hEMC detergent maps, despite EMC7 levels being comparable to the other hEMC subunits in subsequent mass spectrometry analysis. EMC7 thus remains absent from our hEMC detergent model, perhaps due to conformational heterogeneity.

Mass spectrometric analysis of purified hEMC samples in detergent or nanodiscs

GDN solubilized or nanodisc reconstituted hEMC purified by Flag-affinity chromatography and SEC was subjected to mass spectrometric analysis to assess hEMC subunit abundance. For reduction and alkylation of the proteins, proteins were incubated with SDC buffer (1% Sodiumdeoxycholate, 40 mM 2-Chloroacetamide (Sigma-Aldrich), 10 mM tris(2-carboxyethyl) phosphine (TCEP; PierceTM, Thermo Fisher Scientific) in 100 mM Tris, pH 8.0) for 20 min at 37°C. Before digestion, the samples were diluted 1:2 with MS grade water (VWR). Samples were digested overnight at 37°C with 1 µg trypsin (Promega).

The solution of peptides was then acidified with Trifluoroacetic acid (Merck) to a final concentration of 1% and a pH value of <2, followed by purification via SCX StageTips (*Rappsilber et al.,*

2007) washed with 1% TFA in Isopropanol, followed by a second wash with 0.2% TFA, eluted as one fraction with 80% Acetonitrile and 5% Ammonia (Merck). Samples were vacuum dried and re-suspended in 6 μ l of Buffer A (0.1% Formic acid (Roth) in MS grade water (VWR)).

Purified and desalted peptides were loaded onto a 15-cm column (inner diameter: 75 μ m; packed in-house with ReproSil-Pur C18-AQ 1.9- μ m beads, Dr. Maisch GmbH) via the autosampler of the Thermo Easy-nLC 1000 (Thermo Fisher Scientific) at 50°C. Using the nanoelectrospray interface, eluting peptides were directly sprayed onto the benchtop Orbitrap mass spectrometer Q Exactive HF (Thermo Fisher Scientific).

Peptides were loaded in buffer A (0.1% (v/v) Formic acid) at 250 nL/min and percentage of buffer B (80% Acetonitril, 0.1% Formic acid) was ramped to 30% over 45 min followed by a ramp to 60% over 5 min then 95% over the next 5 min and maintained at 95% for another 5 min. The mass spectrometer was operated in a data-dependent mode with survey scans from 300 to 1650 m/z (resolution of 60000 at m/z = 200), and up to 10 of the top precursors were selected and fragmented using higher energy collisional dissociation (HCD with a normalized collision energy of value of 28). The MS2 spectra were recorded at a resolution of 15000 (at m/z = 200). AGC target for MS and MS2 scans were set to 3E6 and 1E5, respectively, within a maximum injection time of 100 and 60 ms for MS and MS2 scans, respectively. Dynamic exclusion was set to 30 ms.

Raw data were processed using the MaxQuant computational platform (**Cox and Mann, 2008**) with standard settings applied. Shortly, the peak list was searched against the reviewed human UniProt database with an allowed precursor mass deviation of 4.5 ppm and an allowed fragment mass deviation of 20 ppm. MaxQuant by default enables individual peptide mass tolerances, which was used in the search. Cysteine carbamidomethylation was set as static modification, and methionine oxidation and N-terminal acetylation as variable modifications. The iBAQ algorithm was used for calculation of approximate abundances for the identified proteins (**Schwanhäusser et al., 2011**) which normalizes the summed peptide intensities by the number of theoretically observable peptides of the protein.

Sequence alignments

T-coffee PSI-Coffee extension (**Notredame et al., 2000**) was used to compute sequence alignments between yEMC, hEMC, and homologous proteins (**Figure 1—figure supplements 6–7, Figure 3—figure supplement 3, Figure 5—figure supplement 3**). Outputs of these alignments were visualized in Jalview (**Waterhouse et al., 2009**) for figure creation and colored by ClustalX convention.

Figure and video creation

All figures were assembled and edited in Adobe Illustrator. **Figure 1** and **Figure 1—figure supplement 4** were created using BioRender. All the visualization, structure figures, and structure videos were made using UCSF ChimeraX 1.0 (**Goddard et al., 2018**) and UCSF Chimera 1.14 (**Pettersen et al., 2004**). Flow cytometry plots were generated in Python and labeled in Adobe Illustrator.

Acknowledgements

We thank J Weibazahn, P Walter, R Irannejad, J Gestwicki, R Scheltema, Ö Karayel, H Nguyen, I Johnson, N Talledge, L Kenner, E Thompson, K Hickey, J Kellermann, S von Gronau, M Feige, K Swain, M Liao, C-W Lee, F Wilfling, and members of the Weissman, Frost, and Schulman laboratories for assistance and helpful discussion; L Metzger, Z Roe-Zurz, M Tessema, DW Chester, and S Aller for assisting with fermentation; M Sun, H Autzen, and E Green for advice on nanodisc reconstitution; F Hagn and I Goba for the gift of the MSP1D1 vector and advice on nanodisc reconstitution; P Thomas and D Asarnow for computational support; M Braunfeld, G Gilbert, E Tse, D Bulkley, M Harrington, A Myasnikov and Z Yu of the UCSF Center for Advanced CryoEM for microscopy support and funded by NIH grants S10OD020054 and 1S10OD021741; J Baker-LePain and the QB3 shared cluster (NIH grant 1S10OD021596-01) for computational support; and the Howard Hughes Medical Institute (HHMI); Z Yu and H Chou of the CryoEM Facility at the HHMI Janelia Research Campus (NIH grant 1S10OD021596-01). D Bollschweiler, T Schäfer and the cryo-EM facility at the Max Planck Institute of Biochemistry; B Steigenberger, the mass spectrometry core facility at the Max Planck Institute of Biochemistry; E Gouaux for the gift of the pEG vector; A Titan X Pascal used for this

research was donated by the NVIDIA Corporation. This study was supported in part by the HDFCCC Laboratory for Cell Analysis Shared Resource Facility through a grant from NIH (P30CA082103). Molecular graphics and analyses performed with UCSF ChimeraX, developed by the Resource for Biocomputing, Visualization, and Informatics at the University of California, San Francisco, with support from National Institutes of Health R01-GM129325 and the Office of Cyber Infrastructure and Computational Biology, National Institute of Allergy and Infectious Diseases. UCSF Chimera is developed by the Resource for Biocomputing, Visualization, and Informatics at the University of California, San Francisco (supported by NIGMS P41-GM103311).

Additional information

Funding




Funder	Grant reference number	Author
Deutsche Forschungsgemeinschaft	Leibniz Prize SCHU 3196/1-1	Brenda A Schulman
Max Planck Society		Brenda A Schulman
National Institutes of Health	P50AI150476	Charles S Craik Natalia Sevillano
National Institutes of Health	1P41CA196276-01	Charles S Craik
Helen Hay Whitney Foundation		Matthew J Shurtleff
Peter und Traudl Engelhorn Stiftung		Bastian Bräuning
Jane Coffin Childs Memorial Fund for Medical Research		Nicole T Schirle Oakdale
National Institutes of Health	1DP2OD017690-01	Adam Frost
National Institutes of Health	GM24485	Robert M Stroud
Howard Hughes Medical Institute		Jonathan S Weissman
Chan Zuckerberg Initiative		Adam Frost
Howard Hughes Medical Institute	55108523	Adam Frost

The funders had no role in study design, data collection and interpretation, or the decision to submit the work for publication.

Author contributions

Lakshmi E Miller-Vedam, Katerina D Popova, Conceptualization, Data curation, Formal analysis, Validation, Investigation, Visualization, Methodology, Writing - original draft, Writing - review and editing; Bastian Bräuning, Conceptualization, Data curation, Formal analysis, Funding acquisition, Validation, Investigation, Visualization, Methodology, Writing - original draft, Writing - review and editing; Nicole T Schirle Oakdale, Conceptualization, Data curation, Formal analysis, Funding acquisition, Validation, Methodology, Writing - review and editing; Jessica L Bonnar, Data curation, Formal analysis, Validation, Visualization, Methodology, Writing - review and editing; Jesuraj R Prabu, Data curation, Validation, Methodology, Writing - review and editing; Elizabeth A Boydston, Natalia Sevillano, Data curation, Formal analysis, Methodology, Writing - review and editing; Matthew J Shurtleff, Funding acquisition, Validation, Writing - review and editing; Robert M Stroud, Conceptualization, Resources, Supervision, Funding acquisition, Methodology, Writing - review and editing; Charles S Craik, Conceptualization, Supervision, Funding acquisition, Methodology, Writing - review and editing; Brenda A Schulman, Adam Frost, Jonathan S Weissman, Conceptualization, Supervision, Funding acquisition, Validation, Writing - review and editing

Author ORCIDs

Lakshmi E Miller-Vedam  <https://orcid.org/0000-0002-2980-7479>
 Bastian Bräuning  <https://orcid.org/0000-0002-7194-2500>
 Katerina D Popova  <https://orcid.org/0000-0002-3927-1284>
 Jessica L Bonnar  <https://orcid.org/0000-0001-5531-4849>
 Elizabeth A Boydston  <http://orcid.org/0000-0001-8365-0436>
 Matthew J Shurtleff  <http://orcid.org/0000-0001-9846-3051>
 Charles S Craik  <https://orcid.org/0000-0001-7704-9185>
 Brenda A Schulman  <https://orcid.org/0000-0002-3083-1126>
 Adam Frost  <https://orcid.org/0000-0003-2231-2577>
 Jonathan S Weissman  <https://orcid.org/0000-0003-2445-670X>

Decision letter and Author response

Decision letter <https://doi.org/10.7554/eLife.62611.sa1>

Author response <https://doi.org/10.7554/eLife.62611.sa2>

Additional files**Supplementary files**

- Supplementary file 1. Mass spectrometry analysis on purified hEMC. SEC purified hEMC in detergent (sheet 1) or nanodiscs (sheet 2) were subjected to tryptic digestion and mass spectrometry. The tables list identified proteins sorted by iBAQ score (descending order). EMC subunits are highlighted in yellow.
- Supplementary file 2. Statistical significance values for flow cytometry data. Table listing p-values for membrane controls (Sheet 1; relates to **Figure 1—figure supplement 3**) and flow cytometry for each of the three client reporters (Sheets 2, 3 and 4; relates to Main **Figures 3** and **5–7** and figures supplements to those figures).
- Supplementary file 3. Comparison of EMC point mutant effects on client proteins. Table listing point mutagenesis performed on hEMC and yEMC and assayed against different client types.
- Supplementary file 4. Uncropped western blots. Blots provided here without cropping, related to **Figure 1—figure supplements 5–6**.
- Supplementary file 5. Plasmid sequences for hEMC mutants and reporters. Table listing sequences of point mutagenesis plasmids used in the hEMC functional assay in this study.
- Transparent reporting form

Data availability

All data generated or analyzed during this study are included in the manuscript or available at an appropriate public data repository. Flow cytometry data and analysis code is available at Github (<https://github.com/katerinadpopova/emcstructurefunction>) (copy archived at <https://archive.softwareheritage.org/swh:1:rev:7ef1dee8de00b98b2cbda4321dc1989435c89eb4/>). Electron microscopy maps are available at the EMDB (unsharpened, sharpened, half maps, FSC file) (accession codes EMDB - 11732, 11733, 23003, 23033), models at the PDB (accession codes PDB - 7ADO, 7ADP, 7KRA, 7KTX), and additional cryo-EM data at EMPIAR. Key Resource Table is included as an appendix to the main article and is referenced throughout the Methods section with relevant reagents used or generated during the course of the study allowing for replication of these or request of specific cell lines and reagents. Supplementary file 1 contains raw mass spectrometry data. Supplementary file 4 contains un-cropped western blots. Supplementary file 5 contains plasmid sequences for mutant constructs generated for this study.

The following datasets were generated:

Author(s)	Year	Dataset title	Dataset URL	Database and Identifier
Miller-Vedam LE,	2020	Cryo-EM structure of	https://www.ebi.ac.uk/	Electron Microscopy

Schirle Oakdale NT, Bräuning B, Boydston EA, Sevillano N, Popova KD, Bonnar JL, Shurtleff MJ, Prabu JR, Stroud RM, Craik CS, Schulman BA, Weissman JS, Frost A		Saccharomyces cerevisiae ER membrane protein complex bound to a Fab in DDM detergent	pdbe/entry/emdb/EMD-23033	Data Bank, EMD-23033
Miller-Vedam LE, Schirle Oakdale NT, Bräuning B, Boydston EA, Sevillano N, Popova KD, Bonnar JL, Shurtleff MJ, Prabu JR, Stroud RM, Craik CS, Schulman BA, Weissman JS, Frost A	2020	Cryo-EM structure of Saccharomyces cerevisiae ER membrane protein complex bound to Fab-DH4 in lipid nanodiscs	https://www.ebi.ac.uk/pdbe/entry/emdb/EMD-23003	Electron Microscopy Data Bank, EMD-23003
Bräuning B, Prabu RS, Miller-Vedam LE, Weissman JS, Frost A, Schulman BA	2020	Cryo-EM structure of human ER membrane protein complex in GDN detergent	https://www.ebi.ac.uk/pdbe/entry/emdb/EMD-11733	Electron Microscopy Data Bank, EMD-11733
Bräuning B, Prabu RS, Miller-Vedam LE, Weissman JS, Frost A, Schulman BA	2020	Cryo-EM structure of human ER membrane protein complex in lipid nanodiscs	https://www.ebi.ac.uk/pdbe/entry/emdb/EMD-11732	Electron Microscopy Data Bank, EMD-11732
Miller-Vedam LE, Schirle Oakdale NT, Bräuning B, Boydston EA, Sevillano N, Popova KD, Bonnar JL, Shurtleff MJ, Prabu RS, Stroud RM, Craik CS, Schulman BA, Weissman JS, Frost A	2020	Cryo-EM structure of Saccharomyces cerevisiae ER membrane protein complex bound to a Fab in DDM detergent	https://www.rcsb.org/structure/7KTX	RCSB Protein Data Bank, 7KTX
Miller-Vedam LE, Schirle Oakdale NT, Bräuning B, Boydston EA, Sevillano N, Popova KD, Bonnar JL, Shurtleff MJ, Prabu RS, Stroud RM, Craik CS, Schulman BA, Weissman JS, Frost A	2020	Cryo-EM structure of Saccharomyces cerevisiae ER membrane protein complex bound to Fab-DH4 in lipid nanodiscs	https://www.rcsb.org/structure/7KRA	RCSB Protein Data Bank, 7KRA
Bräuning B, Prabu RS, Miller-Vedam LE, Weissman JS, Frost A, Schulman BA	2020	Cryo-EM structure of human ER membrane protein complex in lipid nanodiscs	https://www.rcsb.org/structure/7ADO	RCSB Protein Data Bank, 7ADO
Bräuning B, Prabu RS, Miller-Vedam LE, Weissman JS, Frost A, Schulman BA	2020	Cryo-EM structure of human ER membrane protein complex in GDN detergent	https://www.rcsb.org/structure/7ADP	RCSB Protein Data Bank, 7ADP

References

- Abu-Safieh L**, Alrashed M, Anazi S, Alkuraya H, Khan AO, Al-Owain M, Al-Zahrani J, Al-Abdi L, Hashem M, Al-Tarimi S, Sebai MA, Shamia A, Ray-Zack MD, Nassan M, Al-Hassnan ZN, Rahbeeni Z, Waheeb S, Alkharashi A, Abboud E, Al-Hazzaa SA, et al. 2013. Autozygome-guided exome sequencing in retinal dystrophy patients reveals pathogenetic mutations and novel candidate disease genes. *Genome Research* **23**:236–247. DOI: <https://doi.org/10.1101/gr.144105.112>, PMID: 23105016
- Adams PD**, Afonine PV, Bunkóczy G, Chen VB, Echols N, Headd JJ, Hung LW, Jain S, Kapral GJ, Grosse Kunstleve RW, McCoy AJ, Moriarty NW, Oeffner RD, Read RJ, Richardson DC, Richardson JS, Terwilliger TC, Zwart PH. 2011. The Phenix software for automated determination of macromolecular structures. *Methods* **55**: 94–106. DOI: <https://doi.org/10.1016/j.ymeth.2011.07.005>, PMID: 21821126
- Afonine PV**, Poon BK, Read RJ, Sobolev OV, Terwilliger TC, Urzhumtsev A, Adams PD. 2018. Real-space refinement in PHENIX for cryo-EM and crystallography. *Acta Crystallographica. Section D, Structural Biology* **74**:531–544. DOI: <https://doi.org/10.1107/S2059798318006551>, PMID: 29872004
- Amberger JS**, Bocchini CA, Scott AF, Hamosh A. 2019. OMIM.org: leveraging knowledge across phenotype-gene relationships. *Nucleic Acids Research* **47**:D1038–D1043. DOI: <https://doi.org/10.1093/nar/gky1151>, PMID: 30445645
- Anghel SA**, McGilvray PT, Hegde RS, Keenan RJ. 2017. Identification of Oxa1 homologs operating in the eukaryotic endoplasmic reticulum. *Cell Reports* **21**:3708–3716. DOI: <https://doi.org/10.1016/j.celrep.2017.12.006>, PMID: 29281821
- Asarnow D**, Palovcak E, Cheng Y. 2019. UCSF pyem. Zenodo. v0.5. <https://doi.org/10.5281/zenodo.3576630>
- Assimon VA**, Southworth DR, Gestwicki JE. 2015. Specific binding of tetratricopeptide repeat proteins to heat shock protein 70 (Hsp70) and heat shock protein 90 (Hsp90) is regulated by affinity and phosphorylation. *Biochemistry* **54**:7120–7131. DOI: <https://doi.org/10.1021/acs.biochem.5b00801>, PMID: 26565746
- Bagchi P**, Inoue T, Tsai B. 2016. EMC1-dependent stabilization drives membrane penetration of a partially destabilized non-enveloped virus. *eLife* **5**:e21470. DOI: <https://doi.org/10.7554/eLife.21470>, PMID: 28012275
- Bai L**, You Q, Feng X, Kovach A, Li H. 2020. Structure of the ER membrane complex, a transmembrane-domain insertase. *Nature* **584**:475–478. DOI: <https://doi.org/10.1038/s41586-020-2389-3>, PMID: 32494008
- Bircham PW**, Maass DR, Roberts CA, Kiew PY, Low YS, Yegambaram M, Matthews J, Jack CA, Atkinson PH. 2011. Secretory pathway genes assessed by high-throughput microscopy and synthetic genetic array analysis. *Molecular BioSystems* **7**:2589. DOI: <https://doi.org/10.1039/c1mb05175j>, PMID: 21731954
- Biyani N**, Righetto RD, McLeod R, Caujolle-Bert D, Castano-Diez D, Goldie KN, Stahlberg H. 2017. Focus: the interface between data collection and data processing in cryo-EM. *Journal of Structural Biology* **198**:124–133. DOI: <https://doi.org/10.1016/j.jsb.2017.03.007>, PMID: 28344036
- Blatch GL**, Lässle M. 1999. The tetratricopeptide repeat: a structural motif mediating protein-protein interactions. *BioEssays* **21**:932–939. DOI: [https://doi.org/10.1002/\(SICI\)1521-1878\(199911\)21:11<932::AID-BIES5>3.0.CO;2-N](https://doi.org/10.1002/(SICI)1521-1878(199911)21:11<932::AID-BIES5>3.0.CO;2-N), PMID: 10517866
- Borowska MT**, Dominik PK, Anghel SA, Kossiakoff AA, Keenan RJ. 2015. A YidC-like protein in the archaeal plasma membrane. *Structure* **23**:1715–1724. DOI: <https://doi.org/10.1016/j.str.2015.06.025>, PMID: 26256539
- Chaudhary S**, Pak JE, Gruswitz F, Sharma V, Stroud RM. 2012. Overexpressing human membrane proteins in stably transfected and clonal human embryonic kidney 293S cells. *Nature Protocols* **7**:453–466. DOI: <https://doi.org/10.1038/nprot.2011.453>, PMID: 22322218
- Chitwood PJ**, Juszkiwicz S, Guna A, Shao S, Hegde RS. 2018. EMC is required to initiate accurate membrane protein topogenesis. *Cell* **175**:1507–1519. DOI: <https://doi.org/10.1016/j.cell.2018.10.009>, PMID: 30415835
- Cho H**, Stanzione F, Oak A, Kim GH, Yerneni S, Qi L, Sum AK, Chan C. 2019. Intrinsic structural features of the human IRE1 α transmembrane domain sense membrane lipid saturation. *Cell Reports* **27**:307–320. DOI: <https://doi.org/10.1016/j.celrep.2019.03.017>, PMID: 30943411
- Christianson JC**, Olzmann JA, Shaler TA, Sowa ME, Bennett EJ, Richter CM, Tyler RE, Greenblatt EJ, Wade Harper J, Kopito RR. 2012. Defining human ERAD networks through an integrative mapping strategy. *Nature Cell Biology* **14**:93–105. DOI: <https://doi.org/10.1038/ncb2383>
- Coelho JPL**, Stahl M, Bloemeke N, Meighen-Berger K, Alvira CP, Zhang ZR, Sieber SA, Feige MJ. 2019. A network of chaperones prevents and detects failures in membrane protein lipid bilayer integration. *Nature Communications* **10**:672. DOI: <https://doi.org/10.1038/s41467-019-08632-0>, PMID: 30737405
- Cornell CE**, Mileant A, Thakkar N, Lee KK, Keller SL. 2020. Direct imaging of liquid domains in membranes by cryo-electron tomography. *PNAS* **117**:19713–19719. DOI: <https://doi.org/10.1073/pnas.2002245117>, PMID: 32759217
- Corradi V**, Sejdiu BI, Mesa-Gallosio H, Abdizadeh H, Noskov SY, Marrink SJ, Tieleman DP. 2019. Emerging diversity in Lipid-Protein interactions. *Chemical Reviews* **119**:5775–5848. DOI: <https://doi.org/10.1021/acs.chemrev.8b00451>, PMID: 30758191
- Costa EA**, Subramanian K, Nunnari J, Weissman JS. 2018. Defining the physiological role of SRP in protein-targeting efficiency and specificity. *Science* **359**:689–692. DOI: <https://doi.org/10.1126/science.aar3607>, PMID: 29348368
- Cox J**, Mann M. 2008. MaxQuant enables high peptide identification rates, individualized p.p.b.-range mass accuracies and proteome-wide protein quantification. *Nature Biotechnology* **26**:1367–1372. DOI: <https://doi.org/10.1038/nbt.1511>, PMID: 19029910

- Cuff JA**, Barton GJ. 2000. Application of multiple sequence alignment profiles to improve protein secondary structure prediction. *Proteins: Structure, Function, and Genetics* **40**:502–511. DOI: [https://doi.org/10.1002/1097-0134\(20000815\)40:3<502::AID-PROT170>3.0.CO;2-Q](https://doi.org/10.1002/1097-0134(20000815)40:3<502::AID-PROT170>3.0.CO;2-Q), PMID: 10861942
- Dalbey RE**, Kuhn A. 2015. Membrane insertases are present in all three domains of life. *Structure* **23**:1559–1560. DOI: <https://doi.org/10.1016/j.str.2015.08.002>, PMID: 26331454
- Denic V**, Dötsch V, Sinning I. 2013. Endoplasmic reticulum targeting and insertion of tail-anchored membrane proteins by the GET pathway. *Cold Spring Harbor Perspectives in Biology* **5**:a013334. DOI: <https://doi.org/10.1101/cshperspect.a013334>, PMID: 23906715
- Diamantopoulou A**, Sun Z, Mukai J, Xu B, Fenelon K, Karayiorgou M, Gogos JA. 2017. Loss-of-function mutation in *Mirta22/Emc10* rescues specific schizophrenia-related phenotypes in a mouse model of the 22q11.2 deletion. *PNAS* **114**:E6127–E6136. DOI: <https://doi.org/10.1073/pnas.1615719114>, PMID: 28696314
- Dickinson ME**, Flenniken AM, Ji X, Teboul L, Wong MD, White JK, Meehan TF, Wening WJ, Westerberg H, Adissu H, Baker CN, Bower L, Brown JM, Caddle LB, Chiani F, Clary D, Cleak J, Daly MJ, Denegre JM, Doe B, et al. 2016. High-throughput discovery of novel developmental phenotypes. *Nature* **537**:508–514. DOI: <https://doi.org/10.1038/nature19356>, PMID: 27626380
- Ellgaard L**, McCaul N, Chatsisvili A, Braakman I. 2016. Co- and Post-Translational protein folding in the ER: co- and Post-Translational protein folding in the ER. *Traffic* **17**:615–638. DOI: <https://doi.org/10.1111/tra.12392>, PMID: 26947578
- Emsley P**, Lohkamp B, Scott WG, Cowtan K. 2010. Features and development of coot. *Acta Crystallographica. Section D, Biological Crystallography* **66**:486–501. DOI: <https://doi.org/10.1107/S0907444910007493>, PMID: 20383002
- Emsley P**, Cowtan K. 2004. Coot: model-building tools for molecular graphics. *Acta Crystallographica. Section D, Biological Crystallography* **60**:2126–2132. DOI: <https://doi.org/10.1107/S0907444904019158>, PMID: 15572765
- Gilbert LA**, Horlbeck MA, Adamson B, Villalta JE, Chen Y, Whitehead EH, Guimaraes C, Panning B, Ploegh HL, Bassik MC, Qi LS, Kampmann M, Weissman JS. 2014. Genome-Scale CRISPR-Mediated control of gene repression and activation. *Cell* **159**:647–661. DOI: <https://doi.org/10.1016/j.cell.2014.09.029>, PMID: 25307932
- Goddard TD**, Huang CC, Meng EC, Pettersen EF, Couch GS, Morris JH, Ferrin TE. 2018. UCSF ChimeraX: meeting modern challenges in visualization and analysis. *Protein Science* **27**:14–25. DOI: <https://doi.org/10.1002/pro.3235>, PMID: 28710774
- Goehring A**, Lee CH, Wang KH, Michel JC, Claxton DP, Bacongus I, Althoff T, Fischer S, Garcia KC, Gouaux E. 2014. Screening and large-scale expression of membrane proteins in mammalian cells for structural studies. *Nature Protocols* **9**:2574–2585. DOI: <https://doi.org/10.1038/nprot.2014.173>, PMID: 25299155
- Graham JB**, Canniff NP, Hebert DN. 2019. TPR-containing proteins control protein organization and homeostasis for the endoplasmic reticulum. *Critical Reviews in Biochemistry and Molecular Biology* **54**:103–118. DOI: <https://doi.org/10.1080/10409238.2019.1590305>, PMID: 31023093
- Guna A**, Volkmar N, Christianson JC, Hegde RS. 2018. The ER membrane protein complex is a transmembrane domain insertase. *Science* **359**:470–473. DOI: <https://doi.org/10.1126/science.aao3099>, PMID: 29242231
- Hagn F**, Nasr ML, Wagner G. 2018. Assembly of phospholipid nanodiscs of controlled size for structural studies of membrane proteins by NMR. *Nature Protocols* **13**:79–98. DOI: <https://doi.org/10.1038/nprot.2017.094>, PMID: 29215632
- Halbleib K**, Pesek K, Covino R, Hofbauer HF, Wunnicke D, Hänel I, Hummer G, Ernst R. 2017. Activation of the unfolded protein response by lipid bilayer stress. *Molecular Cell* **67**:673–684. DOI: <https://doi.org/10.1016/j.molcel.2017.06.012>, PMID: 28689662
- Harel T**, Yesil G, Bayram Y, Coban-Akdemir Z, Charng WL, Karaca E, Al Asmari A, Eldomery MK, Hunter JV, Jhangiani SN, Rosenfeld JA, Pehlivan D, El-Hattab AW, Saleh MA, LeDuc CA, Muzny D, Boerwinkle E, Gibbs RA, Chung WK, Yang Y, et al. 2016. Monoallelic and biallelic variants in EMC1 identified in individuals with global developmental delay, Hypotonia, scoliosis, and cerebellar atrophy. *The American Journal of Human Genetics* **98**:562–570. DOI: <https://doi.org/10.1016/j.ajhg.2016.01.011>, PMID: 26942288
- Heberle FA**, Doktorova M, Scott HL, Skinkle AD, Waxham MN, Levental I. 2020. Direct label-free imaging of nanodomains in biomimetic and biological membranes by cryogenic electron microscopy. *PNAS* **117**:19943–19952. DOI: <https://doi.org/10.1073/pnas.2002200117>, PMID: 32759206
- Hiramatsu N**, Tago T, Satoh T, Satoh AK. 2019. ER membrane protein complex is required for the insertions of late-synthesized transmembrane helices of Rh1 in *Drosophila* photoreceptors. *Molecular Biology of the Cell* **30**:2890–2900. DOI: <https://doi.org/10.1091/mbc.E19-08-0434>, PMID: 31553680
- Hofbauer HF**, Gecht M, Fischer SC, Seybert A, Frangakis AS, Stelzer EHK, Covino R, Hummer G, Ernst R. 2018. The molecular recognition of phosphatidic acid by an amphipathic helix in Opi1. *Journal of Cell Biology* **217**:3109–3126. DOI: <https://doi.org/10.1083/jcb.201802027>, PMID: 29941475
- Hu M**, Yu H, Gu K, Wang Z, Ruan H, Wang K, Ren S, Li B, Gan L, Xu S, Yang G, Shen Y, Li X. 2018. A particle-filter framework for robust cryo-EM 3D reconstruction. *Nature Methods* **15**:1083–1089. DOI: <https://doi.org/10.1038/s41592-018-0223-8>, PMID: 30504871
- Jacquemyn J**, Cascalho A, Goodchild RE. 2017. The ins and outs of endoplasmic reticulum-controlled lipid biosynthesis. *EMBO Reports* **18**:1905–1921. DOI: <https://doi.org/10.15252/embr.201643426>, PMID: 29074503
- Jones DT**, Taylor WR, Thornton JM. 1994. A model recognition approach to the prediction of all-helical membrane protein structure and topology. *Biochemistry* **33**:3038–3049. DOI: <https://doi.org/10.1021/bi00176a037>, PMID: 8130217
- Jones DT**. 1999. Protein secondary structure prediction based on position-specific scoring matrices. *Journal of Molecular Biology* **292**:195–202. DOI: <https://doi.org/10.1006/jmbi.1999.3091>, PMID: 10493868

- Jonikas MC**, Collins SR, Denic V, Oh E, Quan EM, Schmid V, Weibezahn J, Schwappach B, Walter P, Weissman JS, Schuldiner M. 2009. Comprehensive characterization of genes required for protein folding in the endoplasmic reticulum. *Science* **323**:1693–1697. DOI: <https://doi.org/10.1126/science.1167983>, PMID: 19325107
- Junes-Gill KS**, Gallaher TK, Gluzman-Poltorak Z, Miller JD, Wheeler CJ, Fan X, Basile LA. 2011. hHSS1: a novel secreted factor and suppressor of glioma growth located at chromosome 19q13.33. *Journal of Neuro-Oncology* **102**:197–211. DOI: <https://doi.org/10.1007/s11060-010-0314-6>, PMID: 20680400
- Källberg M**, Wang H, Wang S, Peng J, Wang Z, Lu H, Xu J. 2012. Template-based protein structure modeling using the RaptorX web server. *Nature Protocols* **7**:1511–1522. DOI: <https://doi.org/10.1038/nprot.2012.085>, PMID: 22814390
- Kelley LA**, Mezulis S, Yates CM, Wass MN, Sternberg MJ. 2015. The Phyre2 web portal for protein modeling, prediction and analysis. *Nature Protocols* **10**:845–858. DOI: <https://doi.org/10.1038/nprot.2015.053>, PMID: 25950237
- Kim J**, Stroud RM, Craik CS. 2011. Rapid identification of recombinant fabs that bind to membrane proteins. *Methods* **55**:303–309. DOI: <https://doi.org/10.1016/j.ymeth.2011.09.012>, PMID: 21958987
- Kimanius D**, Forsberg BO, Scheres SH, Lindahl E. 2016. Accelerated cryo-EM structure determination with parallelisation using GPUs in RELION-2. *eLife* **5**:e18722. DOI: <https://doi.org/10.7554/eLife.18722>, PMID: 27845625
- Krogh A**, Larsson B, von Heijne G, Sonnhammer EL. 2001. Predicting transmembrane protein topology with a hidden markov model: application to complete genomes. *Journal of Molecular Biology* **305**:567–580. DOI: <https://doi.org/10.1006/jmbi.2000.4315>, PMID: 11152613
- Krysztofinska EM**, Evans NJ, Thapaliya A, Murray JW, Morgan RML, Martinez-Lumbreras S, Isaacson RL. 2017. Structure and interactions of the TPR domain of Sgt2 with yeast chaperones and Ybr137wp. *Frontiers in Molecular Biosciences* **4**:68. DOI: <https://doi.org/10.3389/fmolb.2017.00068>, PMID: 29075633
- Kudze T**, Mendez-Dorantes C, Jalloh CS, McClellan AJ. 2018. Evidence for interaction between Hsp90 and the ER membrane complex. *Cell Stress and Chaperones* **23**:1101–1115. DOI: <https://doi.org/10.1007/s12192-018-0908-z>, PMID: 29808299
- Kumazaki K**, Kishimoto T, Furukawa A, Mori H, Tanaka Y, Dohmae N, Ishitani R, Tsukazaki T, Nureki O. 2014. Crystal structure of *Escherichia coli* YidC, a membrane protein chaperone and insertase. *Scientific Reports* **4**:7299. DOI: <https://doi.org/10.1038/srep07299>, PMID: 25466392
- Lahiri S**, Chao JT, Tavassoli S, Wong AK, Choudhary V, Young BP, Loewen CJ, Prinz WA. 2014. A conserved endoplasmic reticulum membrane protein complex (EMC) facilitates phospholipid transfer from the ER to mitochondria. *PLOS Biology* **12**:e1001969. DOI: <https://doi.org/10.1371/journal.pbio.1001969>, PMID: 25313861
- Laverty D**, Desai R, Uchański T, Masiulis S, Stec WJ, Malinauskas T, Zivanov J, Pardon E, Steyaert J, Miller KW, Aricescu AR. 2019. Cryo-EM structure of the human $\alpha 1\beta 3\gamma 2$ GABA_A receptor in a lipid bilayer. *Nature* **565**:516–520. DOI: <https://doi.org/10.1038/s41586-018-0833-4>, PMID: 30602789
- Li X**, Mooney P, Zheng S, Booth CR, Braunfeld MB, Gubbens S, Agard DA, Cheng Y. 2013. Electron counting and beam-induced motion correction enable near-atomic-resolution single-particle cryo-EM. *Nature Methods* **10**:584–590. DOI: <https://doi.org/10.1038/nmeth.2472>, PMID: 23644547
- Liebschner D**, Afonine PV, Baker ML, Bunkóczi G, Chen VB, Croll TI, Hintze B, Hung LW, Jain S, McCoy AJ, Moriarty NW, Oeffner RD, Poon BK, Prisant MG, Read RJ, Richardson JS, Richardson DC, Sammito MD, Sobolev OV, Stockwell DH, et al. 2019. Macromolecular structure determination using X-rays, neutrons and electrons: recent developments in phenix. *Acta Crystallographica Section D Structural Biology* **75**:861–877. DOI: <https://doi.org/10.1107/S2059798319011471>, PMID: 31588918
- Lin DL**, Inoue T, Chen YJ, Chang A, Tsai B, Tai AW. 2019. The ER membrane protein complex promotes biogenesis of dengue and zika virus Non-structural Multi-pass transmembrane proteins to support infection. *Cell Reports* **27**:1666–1674. DOI: <https://doi.org/10.1016/j.celrep.2019.04.051>, PMID: 31067454
- Louie RJ**, Guo J, Rodgers JW, White R, Shah N, Pagant S, Kim P, Livstone M, Dolinski K, McKinney BA, Hong J, Sorscher EJ, Bryan J, Miller EA, Hartman JL. 2012. A yeast phenomic model for the gene interaction network modulating CFTR- Δ F508 protein biogenesis. *Genome Medicine* **4**:103. DOI: <https://doi.org/10.1186/gm404>, PMID: 23270647
- Luo WJ**, Gong XH, Chang A. 2002. An ER membrane protein, Sop4, facilitates ER export of the yeast plasma membrane [H⁺] ATPase, Pma1. *Traffic* **3**:730–739. DOI: <https://doi.org/10.1034/j.1600-0854.2002.31005.x>, PMID: 12230471
- Lupas A**, Van Dyke M, Stock J. 1991. Predicting coiled coils from protein sequences. *Science* **252**:1162–1164. DOI: <https://doi.org/10.1126/science.252.5009.1162>, PMID: 2031185
- Marinko JT**, Huang H, Penn WD, Capra JA, Schleich JP, Sanders CR. 2019. Folding and misfolding of human membrane proteins in health and disease: from single molecules to cellular proteostasis. *Chemical Reviews* **119**:5537–5606. DOI: <https://doi.org/10.1021/acs.chemrev.8b00532>, PMID: 30608666
- Marquez J**, Criscione J, Charney RM, Prasad MS, Hwang WY, Mis EK, García-Castro MI, Khokha MK. 2020. Disrupted ER membrane protein complex-mediated topogenesis drives congenital neural crest defects. *Journal of Clinical Investigation* **130**:813–826. DOI: <https://doi.org/10.1172/JCI129308>, PMID: 31904590
- Mastrorarde DN**. 2005. Automated electron microscope tomography using robust prediction of specimen movements. *Journal of Structural Biology* **152**:36–51. DOI: <https://doi.org/10.1016/j.jsb.2005.07.007>, PMID: 16182563

- Mateja A**, Keenan RJ. 2018. A structural perspective on tail-anchored protein biogenesis by the GET pathway. *Current Opinion in Structural Biology* **51**:195–202. DOI: <https://doi.org/10.1016/j.sbi.2018.07.009>, PMID: 30173121
- McDowell MA**, Heimes M, Fiorentino F, Mehmood S, Farkas Á, Coy-Vergara J, Wu D, Bolla JR, Schmid V, Heinze R, Wild K, Flemming D, Pfeffer S, Schwappach B, Robinson CV, Sinning I. 2020. Structural basis of Tail-Anchored membrane protein biogenesis by the GET insertase complex. *Molecular Cell* **80**:72–86. DOI: <https://doi.org/10.1016/j.molcel.2020.08.012>, PMID: 32910895
- McGilvray PT**, Anghel SA, Sundaram A, Zhong F, Trnka MJ, Fuller JR, Hu H, Burlingame AL, Keenan RJ. 2020. An ER translocon for multi-pass membrane protein biogenesis. *eLife* **9**:e56889. DOI: <https://doi.org/10.7554/eLife.56889>, PMID: 32820719
- Mitra K**, Ubarretxena-Belandia I, Taguchi T, Warren G, Engelman DM. 2004. Modulation of the bilayer thickness of exocytic pathway membranes by membrane proteins rather than cholesterol. *PNAS* **101**:4083–4088. DOI: <https://doi.org/10.1073/pnas.0307332101>, PMID: 15016920
- Morin A**, Eisenbraun B, Key J, Sanschagrin PC, Timony MA, Ottaviano M, Sliz P. 2013. Collaboration gets the most out of software. *eLife* **2**:e01456. DOI: <https://doi.org/10.7554/eLife.01456>, PMID: 24040512
- Ngo AM**, Shurtleff MJ, Popova KD, Kulsuptrakul J, Weissman JS, Puschnik AS. 2019. The ER membrane protein complex is required to ensure correct topology and stable expression of flavivirus polyproteins. *eLife* **8**:e48469. DOI: <https://doi.org/10.7554/eLife.48469>, PMID: 31516121
- Notredame C**, Higgins DG, Heringa J. 2000. T-Coffee: a novel method for fast and accurate multiple sequence alignment. *Journal of Molecular Biology* **302**:205–217. DOI: <https://doi.org/10.1006/jmbi.2000.4042>, PMID: 10964570
- O'Donnell JP**, Phillips BP, Yagita Y, Juszkiewicz S, Wagner A, Malinverni D, Keenan RJ, Miller EA, Hegde RS. 2020. The architecture of EMC reveals a path for membrane protein insertion. *eLife* **9**:e57887. DOI: <https://doi.org/10.7554/eLife.57887>, PMID: 32459176
- Obradovic Z**, Peng K, Vucetic S, Radivojac P, Dunker AK. 2005. Exploiting heterogeneous sequence properties improves prediction of protein disorder. *Proteins: Structure, Function, and Bioinformatics* **61 Suppl 7**:176–182. DOI: <https://doi.org/10.1002/prot.20735>, PMID: 16187360
- Ouali M**, King RD. 2000. Cascaded multiple classifiers for secondary structure prediction. *Protein Science* **9**:1162–1176. DOI: <https://doi.org/10.1110/ps.9.6.1162>, PMID: 10892809
- Peng K**, Radivojac P, Vucetic S, Dunker AK, Obradovic Z. 2006. Length-dependent prediction of protein intrinsic disorder. *BMC Bioinformatics* **7**:208. DOI: <https://doi.org/10.1186/1471-2105-7-208>, PMID: 16618368
- Petkovic M**, Oses-Prieto J, Burlingame A, Jan LY, Jan YN. 2020. TMEM16K is an interorganelle regulator of endosomal sorting. *Nature Communications* **11**:3298. DOI: <https://doi.org/10.1038/s41467-020-17016-8>, PMID: 32620747
- Pettersen EF**, Goddard TD, Huang CC, Couch GS, Greenblatt DM, Meng EC, Ferrin TE. 2004. UCSF chimera—a visualization system for exploratory research and analysis. *Journal of Computational Chemistry* **25**:1605–1612. DOI: <https://doi.org/10.1002/jcc.20084>, PMID: 15264254
- Pfeffer S**, Dudek J, Schaffer M, Ng BG, Albert S, Plitzko JM, Baumeister W, Zimmermann R, Freeze HH, Engel BD, Förster F. 2017. Dissecting the molecular organization of the translocon-associated protein complex. *Nature Communications* **8**:14516. DOI: <https://doi.org/10.1038/ncomms14516>, PMID: 28218252
- Pleiner T**, Tomaleri GP, Januszyk K, Inglis AJ, Hazu M, Voorhees RM. 2020. Structural basis for membrane insertion by the human ER membrane protein complex. *Science* **369**:433–436. DOI: <https://doi.org/10.1126/science.abb5008>, PMID: 32439656
- Probert F**, Rice P, Scudamore CL, Wells S, Williams R, Hough TA, Cox IJ. 2015. ¹H NMR metabolic profiling of plasma reveals additional phenotypes in knockout mouse models. *Journal of Proteome Research* **14**:2036–2045. DOI: <https://doi.org/10.1021/pr501039k>, PMID: 25849460
- Punjani A**, Rubinstein JL, Fleet DJ, Brubaker MA. 2017. cryoSPARC: algorithms for rapid unsupervised cryo-EM structure determination. *Nature Methods* **14**:290–296. DOI: <https://doi.org/10.1038/nmeth.4169>, PMID: 28165473
- Punjani A**, Zhang H, Fleet DJ. 2019. Non-uniform refinement: adaptive regularization improves single particle cryo-EM reconstruction. *bioRxiv*. DOI: <https://doi.org/10.1101/2019.12.15.877092>
- Punjani A**, Fleet DJ. 2020. 3D variability analysis: directly resolving continuous flexibility and discrete heterogeneity from single particle cryo-EM images. *bioRxiv*. DOI: <https://doi.org/10.1101/2020.04.08.032466>
- Raman S**, Vernon R, Thompson J, Tyka M, Sadreyev R, Pei J, Kim D, Kellogg E, DiMaio F, Lange O, Kinch L, Sheffler W, Kim BH, Das R, Grishin NV, Baker D. 2009. Structure prediction for CASP8 with all-atom refinement using rosetta. *Proteins: Structure, Function, and Bioinformatics* **77 Suppl 9**:89–99. DOI: <https://doi.org/10.1002/prot.22540>, PMID: 19701941
- Ramírez AS**, Kowal J, Locher KP. 2019. Cryo-electron microscopy structures of human oligosaccharyltransferase complexes OST-A and OST-B. *Science* **366**:1372–1375. DOI: <https://doi.org/10.1126/science.aaz3505>, PMID: 31831667
- Ramlal K**, Palmer CM, Nakane T, Aylett CHS. 2020. Mitigating local over-fitting during single particle reconstruction with SIDESPLITTER. *Journal of Structural Biology* **211**:107545. DOI: <https://doi.org/10.1016/j.jsb.2020.107545>, PMID: 32534144
- Rappsilber J**, Mann M, Ishihama Y. 2007. Protocol for micro-purification, enrichment, pre-fractionation and storage of peptides for proteomics using StageTips. *Nature Protocols* **2**:1896–1906. DOI: <https://doi.org/10.1038/nprot.2007.261>, PMID: 17703201

- Reinisch KM**, De Camilli P. 2016. SMP-domain proteins at membrane contact sites: structure and function. *Biochimica Et Biophysica Acta (BBA) - Molecular and Cell Biology of Lipids* **1861**:924–927. DOI: <https://doi.org/10.1016/j.bbalip.2015.12.003>, PMID: 26686281
- Richard M**, Boulin T, Robert VJ, Richmond JE, Bessereau JL. 2013. Biosynthesis of ionotropic acetylcholine receptors requires the evolutionarily conserved ER membrane complex. *PNAS* **110**:E1055–E1063. DOI: <https://doi.org/10.1073/pnas.1216154110>, PMID: 23431131
- Ritchie TK**, Grinkova YV, Bayburt TH, Denisov IG, Zolnerciks JK, Atkins WM, Sligar SG. 2009. Chapter 11 - Reconstitution of membrane proteins in phospholipid bilayer nanodiscs. *Methods in Enzymology* **464**:211–231. DOI: [https://doi.org/10.1016/S0076-6879\(09\)64011-8](https://doi.org/10.1016/S0076-6879(09)64011-8), PMID: 19903557
- Rost B**. 2001. Review: protein secondary structure prediction continues to rise. *Journal of Structural Biology* **134**:204–218. DOI: <https://doi.org/10.1006/jsbi.2001.4336>, PMID: 11551180
- Rothstein R**. 1991. Targeting, disruption, replacement, and allele rescue: integrative DNA transformation in yeast. *Methods in Enzymology* **194**:281–301. DOI: [https://doi.org/10.1016/0076-6879\(91\)94022-5](https://doi.org/10.1016/0076-6879(91)94022-5), PMID: 2005793
- Roy A**, Kucukural A, Zhang Y. 2010. I-TASSER: a unified platform for automated protein structure and function prediction. *Nature Protocols* **5**:725–738. DOI: <https://doi.org/10.1038/nprot.2010.5>, PMID: 20360767
- Salas-Estrada LA**, Leioatts N, Romo TD, Grossfield A. 2018. Lipids alter rhodopsin function via Ligand-like and Solvent-like interactions. *Biophysical Journal* **114**:355–367. DOI: <https://doi.org/10.1016/j.bpj.2017.11.021>, PMID: 29401433
- Samuelson JC**, Chen M, Jiang F, Möller I, Wiedmann M, Kuhn A, Phillips GJ, Dalbey RE. 2000. YidC mediates membrane protein insertion in Bacteria. *Nature* **406**:637–641. DOI: <https://doi.org/10.1038/35020586>, PMID: 10949305
- Satoh T**, Ohba A, Liu Z, Inagaki T, Satoh AK. 2015. dPob/EMC is essential for biosynthesis of rhodopsin and other multi-pass membrane proteins in *Drosophila* photoreceptors. *eLife* **4**:e06306. DOI: <https://doi.org/10.7554/eLife.06306>
- Savidis G**, McDougall WM, Meraner P, Perreira JM, Portmann JM, Trincucci G, John SP, Aker AM, Renzette N, Robbins DR, Guo Z, Green S, Kowalik TF, Brass AL. 2016. Identification of Zika virus and dengue virus dependency factors using functional genomics. *Cell Reports* **16**:232–246. DOI: <https://doi.org/10.1016/j.celrep.2016.06.028>, PMID: 27342126
- Scheufler C**, Brinker A, Bourenkov G, Pegoraro S, Moroder L, Bartunik H, Hartl FU, Moarefi I. 2000. Structure of TPR domain-peptide complexes: critical elements in the assembly of the Hsp70-Hsp90 multichaperone machine. *Cell* **101**:199–210. DOI: [https://doi.org/10.1016/S0092-8674\(00\)80830-2](https://doi.org/10.1016/S0092-8674(00)80830-2), PMID: 10786835
- Schlegel T**, Mirus O, von Haeseler A, Schleiff E. 2007. The tetratricopeptide repeats of receptors involved in protein translocation across membranes. *Molecular Biology and Evolution* **24**:2763–2774. DOI: <https://doi.org/10.1093/molbev/msm211>, PMID: 17905998
- Schwanhäusser B**, Busse D, Li N, Dittmar G, Schuchhardt J, Wolf J, Chen W, Selbach M. 2011. Global quantification of mammalian gene expression control. *Nature* **473**:337–342. DOI: <https://doi.org/10.1038/nature10098>, PMID: 21593866
- Sejdiu BI**, Tieleman DP. 2020. Lipid-Protein interactions are a unique property and defining feature of G Protein-Coupled receptors. *Biophysical Journal* **118**:1887–1900. DOI: <https://doi.org/10.1016/j.bpj.2020.03.008>, PMID: 32272057
- Shaikh TR**, Gao H, Baxter WT, Asturias FJ, Boisset N, Leith A, Frank J. 2008. SPIDER image processing for single-particle reconstruction of biological macromolecules from electron micrographs. *Nature Protocols* **3**:1941–1974. DOI: <https://doi.org/10.1038/nprot.2008.156>, PMID: 19180078
- Shurtleff MJ**, Itzhak DN, Hussmann JA, Schirle Oakdale NT, Costa EA, Jonikas M, Weibezahn J, Popova KD, Jan CH, Sinitcyn P, Vembar SS, Hernandez H, Cox J, Burlingame AL, Brodsky JL, Frost A, Borner GH, Weissman JS. 2018. The ER membrane protein complex interactively cotranslationally to enable biogenesis of multipass membrane proteins. *eLife* **7**:e37018. DOI: <https://doi.org/10.7554/eLife.37018>, PMID: 29809151
- Song Y**, DiMaio F, Wang RY, Kim D, Miles C, Brunette T, Thompson J, Baker D. 2013. High-resolution comparative modeling with RosettaCM. *Structure* **21**:1735–1742. DOI: <https://doi.org/10.1016/j.str.2013.08.005>, PMID: 24035711
- Stagg SM**, Noble AJ, Spilman M, Chapman MS. 2014. ResLog plots as an empirical metric of the quality of cryo-EM reconstructions. *Journal of Structural Biology* **185**:418–426. DOI: <https://doi.org/10.1016/j.jsb.2013.12.010>, PMID: 24384117
- Suloway CJ**, Chartron JW, Zaslaver M, Clemons WM. 2009. Model for eukaryotic tail-anchored protein binding based on the structure of Get3. *PNAS* **106**:14849–14854. DOI: <https://doi.org/10.1073/pnas.0907522106>, PMID: 19706470
- Talbot BE**, Vanderpe DH, Stotter BR, Alper SL, Schlondorff JS. 2019. Transmembrane insertases and N-glycosylation critically determine synthesis, trafficking, and activity of the nonselective cation channel TRPC6. *Journal of Biological Chemistry* **294**:12655–12669. DOI: <https://doi.org/10.1074/jbc.RA119.008299>, PMID: 31266804
- Tang X**, Snowball JM, Xu Y, Na CL, Weaver TE, Clair G, Kyle JE, Zink EM, Ansong C, Wei W, Huang M, Lin X, Whitsett JA. 2017. EMC3 coordinates surfactant protein and lipid homeostasis required for respiration. *Journal of Clinical Investigation* **127**:4314–4325. DOI: <https://doi.org/10.1172/JCI94152>, PMID: 29083321
- Tian S**, Wu Q, Zhou B, Choi MY, Ding B, Yang W, Dong M. 2019. Proteomic analysis identifies membrane proteins dependent on the ER membrane protein complex. *Cell Reports* **28**:2517–2526. DOI: <https://doi.org/10.1016/j.celrep.2019.08.006>, PMID: 31484065

- Volkmar N**, Thezenas ML, Louie SM, Juszkievicz S, Nomura DK, Hegde RS, Kessler BM, Christianson JC. 2019. The ER membrane protein complex promotes biogenesis of sterol-related enzymes maintaining cholesterol homeostasis. *Journal of Cell Science* **132**:jcs223453. DOI: <https://doi.org/10.1242/jcs.223453>, PMID: 30578317
- Volkmar N**, Christianson JC. 2020. Squaring the EMC - how promoting membrane protein biogenesis impacts cellular functions and organismal homeostasis. *Journal of Cell Science* **133**:jcs243519. DOI: <https://doi.org/10.1242/jcs.243519>, PMID: 32332093
- Volmer R**, van der Ploeg K, Ron D. 2013. Membrane lipid saturation activates endoplasmic reticulum unfolded protein response transducers through their transmembrane domains. *PNAS* **110**:4628–4633. DOI: <https://doi.org/10.1073/pnas.1217611110>, PMID: 23487760
- Vyas NK**, Vyas MN, Chervenak MC, Johnson MA, Pinto BM, Bundle DR, Quijcho FA. 2002. Molecular recognition of oligosaccharide epitopes by a monoclonal fab specific for *Shigella flexneri* Y lipopolysaccharide: x-ray structures and thermodynamics. *Biochemistry* **41**:13575–13586. DOI: <https://doi.org/10.1021/bi0261387>, PMID: 12427018
- Wainberg M**, Kamber RA, Balsubramani A, Meyers RM, Sinnott-Armstrong N, Hornburg D, Jiang L, Chan J, Jian R, Gu M, Shcherbina A, Dubreuil MM, Spees K, Snyder MP, Kundaje A, Bassik MC. 2019. A genome-wide almanac of co-essential modules assigns function to uncharacterized genes. *bioRxiv*. DOI: <https://doi.org/10.1101/827071>
- Ward JJ**, Sodhi JS, McGuffin LJ, Buxton BF, Jones DT. 2004. Prediction and functional analysis of native disorder in proteins from the three kingdoms of life. *Journal of Molecular Biology* **337**:635–645. DOI: <https://doi.org/10.1016/j.jmb.2004.02.002>, PMID: 15019783
- Waterhouse AM**, Procter JB, Martin DM, Clamp M, Barton GJ. 2009. Jalview version 2—a multiple sequence alignment editor and analysis workbench. *Bioinformatics* **25**:1189–1191. DOI: <https://doi.org/10.1093/bioinformatics/btp033>, PMID: 19151095
- Weissmann F**, Petzold G, VanderLinden R, Huis In 't Veld PJ, Brown NG, Lampert F, Westermann S, Stark H, Schulman BA, Peters JM. 2016. biGBac enables rapid gene assembly for the expression of large multisubunit protein complexes. *PNAS* **113**:E2564–E2569. DOI: <https://doi.org/10.1073/pnas.1604935113>, PMID: 27114506
- Wideman JG**. 2015. The ubiquitous and ancient ER membrane protein complex (EMC): tether or not? *F1000Research* **4**:624. DOI: <https://doi.org/10.12688/f1000research.6944.1>, PMID: 26512320
- Wu S**, Avila-Sakar A, Kim J, Booth DS, Greenberg CH, Rossi A, Liao M, Li X, Alian A, Griner SL, Juge N, Yu Y, Mergel CM, Chaparro-Riggers J, Strop P, Tampé R, Edwards RH, Stroud RM, Craik CS, Cheng Y. 2012. Fabs enable single particle cryoEM studies of small proteins. *Structure* **20**:582–592. DOI: <https://doi.org/10.1016/j.str.2012.02.017>, PMID: 22483106
- Xiong L**, Zhang L, Yang Y, Li N, Lai W, Wang F, Zhu X, Wang T. 2020. ER complex proteins are required for rhodopsin biosynthesis and photoreceptor survival in *Drosophila* and mice. *Cell Death & Differentiation* **27**:646–661. DOI: <https://doi.org/10.1038/s41418-019-0378-6>, PMID: 31263175
- Yang J**, Yan R, Roy A, Xu D, Poisson J, Zhang Y. 2015. The I-TASSER suite: protein structure and function prediction. *Nature Methods* **12**:7–8. DOI: <https://doi.org/10.1038/nmeth.3213>, PMID: 25549265
- Zhang Y**. 2008. I-TASSER server for protein 3D structure prediction. *BMC Bioinformatics* **9**:40. DOI: <https://doi.org/10.1186/1471-2105-9-40>, PMID: 18215316
- Zhang K**. 2016. Gctf: real-time CTF determination and correction. *Journal of Structural Biology* **193**:1–12. DOI: <https://doi.org/10.1016/j.jsb.2015.11.003>, PMID: 26592709
- Zhang S**, Xu C, Larrimore KE, Ng DTW. 2017. Slp1-Emp65: a guardian factor that protects folding polypeptides from promiscuous degradation. *Cell* **171**:346–357. DOI: <https://doi.org/10.1016/j.cell.2017.08.036>, PMID: 28919078
- Zheng SQ**, Palovcak E, Armache JP, Verba KA, Cheng Y, Agard DA. 2017. MotionCor2: anisotropic correction of beam-induced motion for improved cryo-electron microscopy. *Nature Methods* **14**:331–332. DOI: <https://doi.org/10.1038/nmeth.4193>, PMID: 28250466
- Zhou Y**, Wu F, Zhang M, Xiong Z, Yin Q, Ru Y, Shi H, Li J, Mao S, Li Y, Cao X, Hu R, Liew CW, Ding Q, Wang X, Zhang Y. 2018. EMC10 governs male fertility via maintaining sperm ion balance. *Journal of Molecular Cell Biology* **10**:503–514. DOI: <https://doi.org/10.1093/jmcb/mjy024>, PMID: 29659949
- Zimmermann L**, Stephens A, Nam SZ, Rau D, Kübler J, Lozajic M, Gabler F, Söding J, Lupas AN, Alva V. 2018. A completely reimplemented MPI bioinformatics toolkit with a new HHpred server at its core. *Journal of Molecular Biology* **430**:2237–2243. DOI: <https://doi.org/10.1016/j.jmb.2017.12.007>, PMID: 29258817
- Zivanov J**, Nakane T, Forsberg BO, Kimanius D, Hagen WJ, Lindahl E, Scheres SH. 2018. New tools for automated high-resolution cryo-EM structure determination in RELION-3. *eLife* **7**:e42166. DOI: <https://doi.org/10.7554/eLife.42166>, PMID: 30412051